JAERI-M
82-172

JAPANESE CONTRIBUTIONS TO IAEA INTOR WORKSHOP,

PHASE IIA

CHAPTER V: RF HEATING AND CURRENT DRIVE

November   1 9 8 2

Kenro MIYAMOTO[*1], Masayoshi SUGIHARA,

Haruyuki KIMURA, Hiroshi MATSUMOTO, Kazuo ODAJIMA,

Tsuyoshi IMAI, Atsushi FUKUYAMA[*2], Masao OKAMOTO[*3],

Takashi NAGASHIMA, Takumi YAMAMOTO, Tadao OHNO[*4],

Noriyuki KOBAYASHI[*4], Takao UCHIDA[*4], Jyunji OHMORI[*4],

Yoshio SAWADA[*4], Katsuyuki EBISAWA[*4], Katsuya UCHIDA[*4],

Michinori YAMAUCHI[*4], and Noboru FUJISAWA

Japanese Contributions

to IAEA INTOR Workshop, Phase IIA

Chapter V: RF Heating and Current Drive

Kenro MIYAMOTO[*1], Masayoshi SUGIHARA, Haruyuki KIMURA,

Hiroshi MATSUMOTO, Kazuo ODAJIMA, Tsuyoshi IMAI,

Atsushi FUKUYAMA[*2], Masao OKAMOTO[*3], Takashi NAGASHIMA,

Takumi YAMAMOTO, Tadao OHNO[*4], Noriyuki KOBAYASHI[*4],

Takao UCHIDA[*4], Jyunji OHMORI[*4], Yoshio SAWADA[*4],

Katsuyuki EBISAWA[*4], Katsuya UCHIDA[*4], Michinori YAMAUCHI[*4]

and Noboru FUJISAWA

Fusion Research and Development Center

Tokai Research Establishment, JAERI

This report corresponds to Chapter V of Japanese contribution report to IAEA INTOR workshop, Phase IIA. Physics studies for radio frequency heating are concentrated on heating to ignition by means of ion cyclotron and lower hybrid ranges of frequencies, and discharge start-up assist and current drive by lower hybrid range. Their system design studies are also performed.

*1) The university of Tokyo.

*2) Okayama University.

*3) Nagoya University.

*4) Toshiba Corporation.

INTOR フェーズ II A ワークショップ検討報告書
第 V 章：RF による加熱と電流駆動

日本原子力研究所東海研究所

核融合研究開発推進センター

宮本健郎[*1]・杉原　正芳・木村　晴行・松本　　宏

小田島和男・今井　　剛・福山　淳[*2]・岡本正雄[*3]

永島　　孝・山本　　巧・大野忠雄[*4]・小林則幸[*4]

内田孝穂[*4]・大森順次[*4]・沢田芳夫[*4]・海老沢克之[*4]

内田　勝也・山内通則[*4]・藤沢　　登

　このレポートは IAEA　INTORフェーズ II A ワークショップに対する国内の検討報告書の第 V 章に相当するものである。高周波加熱の物理検討として，イオンサイクロトロン周波数帯および低ハイブリッド周波数帯を用いた自己点火に至る主加熱，低ハイブリッド周波数帯を用いた炉心起動補助と電流駆動に重点を置いた。さらにこれらのシステムの概念設計を行なった。

＊１）東京大学
＊２）岡山大学
＊３）名古屋大学
＊４）東芝（株）

Contents

目　　　　次

1. Physics Basis

1.1 Ion cyclotron heating to ignition

H. KIMURA, H. MATSUMOTO, K. ODAJIMA, M. SUGIHARA

§1. Introduction

High power ICRF (Ion Cyclotron Range of Frequency) heating are now underway in TFR [1], PLT [2] and JFT-2 [3]. According to the encouraging results obtained in these devices, ICRF heating is considered to be very promising for heating the INTOR plasma to ignition.

Heating modes

In INTOR, the lauching structure must be located on the outside of the torus. Therefore, the heating scenarios can be considered as follows.

(i) $\omega = \Omega_{CH} = 2\ \Omega_{CD}$ (84 MHz) in a H-D-T mixture with H as minority species or $\omega = \Omega_{CHe}3 = 2\ \Omega_{CT}$ (56 MHz) in a He^3-D-T mixture with He^3 as minority.

(ii) $\omega = 2\ \Omega_{CD}$ (84 MHz) or $\omega = 3\ \Omega_{CD}$ (126 MHz) in a D-T plasma.

The scheme (i) so-called minority heating regime, which has been intensively studied in PLT and the heating mechanism is well understood [2]. The scheme (ii) is attractive for avoiding additional minority species, since in the minority regime almost whole RF power goes to minority species, resulting in energetic ion tail, which increases beta requirement as well as impurity production due to loss particles. In addition, higher frequency is desirable for employing a wave guide, while is more suitable in reactor environments.

The second harmonic heating was confirmed in PLT with outside excitation [2]. In JFT-2 experiment, we study second harmonic heating of a deuterium plasma with 2 ∿ 4% of H component for inside excitation

[3]. Inside excitation is appropriate for such experiment, since the excited fast wave couples more tightly to the ion Bernstein wave, which plays a key role in the heating than for outside excitation. We observed deuterium high energy tail, indicating the deuterium second harmonic heating even in the presece of $2 \sim 4\%$ minority H component.

Antenna coupling and wave propagation

Establishment of the scaling law of the antenna loading impedance is necessary for the design of antenna, matching network and transmission line system. Figure V-1-1 shows experimental results on the loading resistance R_s in JFT-2. R_s is strongly dependent on the horizontal distance Δ_H between antenna and plasma, and dependence on the average electron density is weak. The value of R_s is in good agreement with the strong damping model [4].

From the anlaysis of ray tracing, the RF power deposition profile is highly dependent on the poloidal position of the wave excitation. From this point of view, the antenna must be located on the equatorial plane of the torus and its poloidal angle be as small as possible. The rays from such portion of the plasma cross-section goes deeply into the plasma and encounter with a damping zone.

The poloidal mode number of the antenna is not important, since the wave is damped with a single pass. In JFT-2 experiment, we have obtained good ion heating results (4×10^{13} eV cm^{-3} kW^{-1} at least up to RF net power 500 kW) using 1/4-turn antennas.

§2. Antenna system

The maximum RF power per port is limited by the RF breakdown due to the high voltage generated at the antenna, power feedthrough, transmission line and stub tuner. The maximum voltage V_A in the antenna scales as

$$V_A \propto (P_{RF} \; L \; R^{-1} \; C^{-1})^{\frac{1}{2}} \quad ,$$

where P_{RF}, R, L and C are RF power, resistance, inductance and capacitance of the antenna, respectively. To reduce the voltage, R and C must be as large as possible and L as low as possible.

Antenna dimension

The port size of INTOR is ∿3 m in hight and ∿2 m in width. The ICRF and antenna consists of a coil, a return conductor and a Faraday shield (Fig. V-1-2). The basic dimensions of the antenna, which determine the antenna loading impedance, are as follows (Fig. V-1-2).

d_0 : the distance between the plasma edge and the Faraday shield.

d_1 : the distance between the Faraday shield and the coil.

d_2 : the distance between the coil and the return conductor.

w : the coil width.

The loading impedance is calculated using the strong damping model [4], which well explains experimental values in TFR, DIVA and JFT-2.

The electron density profile is taken as

$$n_e = n_{eo} \left\{ 1 - \left(\frac{r}{a'}\right)^m \right\} \quad ,$$

where a' (123.8 cm) is the effective plasma radius with the density decay length of 3.8 cm in the scrape-off layer. We assume the radial position of the Faraday shield coincides with that of the first wall,

i.e. $d_0 = 6.2$ cm. This is a severe condition for the antenna-plasma coupling, but is desirable for the antenna material, since the heat load to the antenna is kept at least to the level of the first wall. We consider that the Faraday shield does not affect the antenna resistance but adds a paralell capacitance without inductance, resulting in reduction of the wave length on the coil.

Calculation results of the loading impedance as a function of $d_0 + d_1$, d_2 and w are shown in Fig. V-1-3 for $n_{eo} = 1.5 \times 10^{14}$ cm^{-3} and m = 4.

From the figure, one can see that smaller value of $d_0 + d_1$ is favourable for both R and ωL. R and ωL depend weakly on d_2 for $d_2 >$ 25 cm. ωL decreases rapidly with increasing w, and although somewhat slowly, R decreases too.

If we choose $d_1 = 3$ cm, $d_2 = 30$ cm and w = 40 cm (these values are not yet perfectly optimized), we obtain R = 10.7 Ω/m and $\omega L = 103$ Ω/m.

Figure V-1-4 shows change of the loading impendance with the peak electron density and the density profile. While ωL is almost constant for $n_{eo} > 5 \times 10^{13}$ cm^{-3}, R decreases rapidly with increasing n_{eo}. This dependence is a feature of the wide antenna. For a narrow antenna (w = 5 $\sim$ 6 cm), which is usually used in the present-day device, R increases slowly with increasing n_{eo}. The reason of the different dependence is due to the difference of the width of the k_z spectrum. The dependence on the density profile is small both for R and ωL.

Peak voltage in the antenna

The characteristic impedance Z_o of the antenna is estimated to be $\sim$25 Ω assuming the distance between the Faraday shield and coil of 1.5 cm. The wavelength in the antenna is reduced to 0.46 of the

free space wavelength (λ = 3.5 m for 85 MHz).

We assume the coil length is 0.9 m. Then the peak voltage in the antenna for P_{RF} = 12.5 MW is estimated to be 60 kV. This value seems to be too high to prevent RF breakdown. Therefore, we recommend four antennas system for a single port (Fig. V-1-5) as proposed in JET [5]. In this case, the peak voltage is limited to 30 kV. This value is still high considering 1.5 cm gap between the coil and the Faraday shield, but is not impossible to overcome from the technical point of view.

k_z spectrum of the antennas

Figure V-1-6 shows the k_z spectrum of a real component of the loading impedance for a single antenna and two antennas with various phase differences δ. R and ωL per antenna are almost the same for a single sntenna and two antennas with δ = 0 and they are somewhat smaller for the other two cases.

Even for a single antenna case, the spectrum is relatively narrow, because of the large width of the antenna. For the case of two antennas, whose interval is assumed to be 100 cm, the spectra become very sharp. k_z which provide maximum peak values are followingly.

δ	k_z (m^{-1})
0	$\sim$ 0
$\pi/2$	$\sim$ 1.5
π	$\sim$ ± 2.8

From the point of view of the plasma heating, large k_z is favourable. Therefore, δ = π is a reasonable choice.

§3. Wave propagation and damping

We calculate the wave propagation and damping for the deuterium second harmonic heating and the hydrogen minority heating on the basis of the ray tracing analysis [6]. The antennas are placed near the equatorial plane and have the poloidal angle $|\theta| \leq 40°$. We assume $k_z = 3$ m^{-1} because of the sharp profile of the k_z-spectrum as shown in Fig. V-1-6.

The ray tracing analysis is appropriate to calculate the wave propagation to the damping zone. However, in the damping zone, the ray tracing analysis is not valid and the full wave equation must be solved, especially for the second harmonic regime. The fast wave incident from the low field side is partly absorbed, transmitted, reflected, and converted to the ion Bernstein wave at the deuterium second harmonic cyclotron resonance layer.

From the approximate fourth order wave equation which does not incldue absorption, the tunneling parameter η is derived followingly [7,8].

$$\eta = \frac{\pi}{4c} R_o \, \omega_{pD} \, (\beta_D + \frac{n_H}{n_D}) \quad ,$$

where c, R_o, ω_{pD} and β_D are speed of light, major radius, deuteron plasma frequency and deuteron toroidal beta, respectively. For the fast wave from the low field side, conversion, tunneling and reflection take place with the coefficient $a_0 = e^{-2\eta}(1 - e^{-2\eta})$, $a_1 = e^{-2\eta}$ and $a_2 = (1 - e^{-2\eta})^2$, respectively.

In the deuterium second harmonic case, η is proportional to $n_D^{\frac{3}{2}} T_D$. Typically η increases by 40 times from the Joule plasma to the ignition plasma ($\eta \sim 0.066 \rightarrow 2.8$). Then the conversion, tunneling and reflection coefficient change as follows; $a_0 = 0.11 \rightarrow \sim 0$,

$a_1 = 0.88 \rightarrow \sim 0$ and $a_2 = 0.015 \rightarrow \sim 1$. Thus in the early stage of the heating, both the conversion and reflection are small and the tunneling is dominant due to the the low β_D. Further investigations are needed in experiment and theory to determine whether the second harmonic heating alone is sufficient even in the early stage or minority proton must be added.

When the plasma approaches to the ignition, the second harmonic resonance layer plays a role of a perfect reflection wall for the fast wave from the low field side and the wave power is absorbed in the vicinity of the second harmonic resonance layer via deuterium second harmonic cyclotron damping.

On the other hand, in the minority regime (e.g. 5% H +47.5% D + 47.5 % T), the two-ion hybrid resonance-cut-off pair is formed and the fast wave is perfectly reflected even for the Joule plasma parameters.

In the ray tracing code, an approximate dispersion relation is used. The confluent region of the fast and ion Bernstein wave does not appear. The ray from the low field side is perfectly reflected, while the ray from the high field side is perfectly converted to the ion Bernstein wave.

Therefore, the ray tracing is valid only if the reflection coefficient a_2 is close to unity for the low field side excitation, or only if the conversion coefficient $b_o (=1 - e^{-2\eta})$ is close to unity for the high field side incidence.

Figure V-1-7 shows the ray trajectory in the poloidal cross-section for the deuterium second harmonic case (50% D + 50% T) and the proton minority case (5% H + 47.5% D + 47.5% T). As the plasma parameters, intermediate values between the Joule and the ignition are taken, i.e.

$T_{eo} = T_{io} = 5.5$ keV and $n_{eo} = 2 \times 10^{14}$ cm^{-3}. Parabolic profiles of the temperature and density are assumed. In both cases the rays incident from the low field side are reflected at the second harmonic resonance layer, return back to the peripheral region and are reflected again at the fast wave cut-off layer. Such processes are continued till the wave power is almost absorbed. The power absorption processes are shown in Fig. V-1-8, where the ray trajectories are projected on the X-axis. About 44% and 29% are absorbed for one pass by deuterons for the second harmonic case and mainly by protons for the minority heating case, respectively.

§4. Power deposition profile

The radial power deposition profiles to each species are calculated by summing up the absorbed power of many rays emanating from the antenna.

Figure V-1-9 (a) and (b) depict thus obtained power deposition profiles for the second harmonic heating and the minority heating respectively. Plasma parameters, and temperature and density profiles are the same as in Fig. V-1-7. The profile is more peaked in the second harmonic heating case than in the minority heating case. However, the deposition profile is sensitive to the density profile. Figure V-1-10 shows the broadening of the power deposition profile of the second harmonic case for the density profile $n = n_o (1 - (\frac{r}{a})^6)$.

The wave propagation and damping change considerably with temperature. Power deposition profiles are calculated as a function of temperature for the deuterium second harmonic heating case. Here, the damping by the tritium is neglected.

We assume the plasma specifications follows.

$$n_e(r) = [n_{eo} - n_s][1 - (\frac{r}{a})^2] + n_s$$

$$T_e(r) = [T_{eo} - T_s][1 - (\frac{r}{a})^2] + T_s$$

$$n_{eo} = 2 \times 10^{14} \text{ cm}^{-3}, \quad n_s = 0.05 \, n_{eo}$$

$$50 - 50 \quad D - T$$

$$T_e = T_i, \quad T_s = 0.05 \, T_{eo}$$

$$q_o = 1, \quad q_a = 2.3$$

$$f = 84 \text{ MHz}, \quad k_z = 10 \text{ m}^{-1}$$

The power deposition profile is calculated by summing up the absorbed power of 4 rays emanating from the antenna $(5° \leq \theta \leq 30°)$. Figure V-1-11 (a) $\sim$ (e) show the results. Corresponding electron temperature are 1, 5, 10, 15 and 20 keV, respectively. At T_{eo} = 1 keV, almost all of the power goes to deuterons and the deposition profile is highly peaked on axis. The deposition profile of deuterons becomes broader with increasing ion temperature, but RF power is still perfectly deposited within $r < a/2$ at T_{eo} = 20 keV. The heating power to electrons increases and its profile becomes more hollow with increasing electron temperature. Fraction of the power deposited in deuterons and electrons versus electron temperature is shown in Fig. V-1-12. The power to electrons increases with increasing electron temperature, resulting in the reduction of the power to the deuterons. Above $T_{eo} \sim$ 15 keV, fraction of the power to electrons exceeds the one to deuterons.

The single pass absorption probability is given in Fig. V-1-13 as a function of the central electron temperature. Above T_{eo} = 15 keV, strong single pass absorption (>80%) occurs. In calculation, the ray is perfectly reflected at the deuteron second harmonic resonance layer.

The power absorption probability is defined as the rate of the power absorbed from the ray starting point to the reflection point. Therefore, the power, which transmits and is absorbed on the high field side of the deuteron second harmonic resonance layer, is neglected. Such effect should be taken into account especially in the low β_D region ($T_{eo} < 5$ keV). Therefore, the single pass absorption in Fig. V-1-13 is underestimated in this region.

§5. Ignition approach by ICRF heating

Preliminary calculations of ignition approach by ICRF heating are made by one-dimensional transport code with the power deposition profile given in fig. V-1-10. The results are shown in Fig. V-1-14. ICRF heating is started at t = 5 sec. The average ion density is slightly increased in time ($\bar{n}_D = \bar{n}_T = 5 \times 10^{19}$ m^{-3} at t = 5 s → $\bar{n}_D = \bar{n}_T = 6 \times 10^{19}$ m^{-3} at t = 10 s). Power deposition profile is assumed to be constant during the heating. Heating power of about 50 MW is sufficient to ignite the INTOR plasma. It is also expected that the heating power of 20 ~ 30 MW can ignite the plasma.

§6. Conclusion

Application of ICRF heating in a reactor size tokamak (INTOR) was investigated. It is possible to deliver 12.5 MW of RF power from a single port by antenna excitation. At most 50 MW of RF power is sufficient to ignite the INTOR plasma via deuterium second harmonic heating.

References

[1] TFR GROUP, Proceedings of the 3rd Joint Varenna-Grenoble Int.
     Symp. on Heating in Toroidal Plasma, Grenoble, 1982.

[2] HOSEA, J., et al., ibid.

[3] JFT-2 GROUP, ibid.; KIMURA, H., et al., Japan Atomic Energy
     Research Institute Report JAERI-M 82-046, 1982.

[4] ADAM, J., EUR-CEA-FC-1004 (1979).

[5] ADAM, J., et al., EUR-CEA-FC-1065 (1980).

[6] McVEY, E. D., Nucl. Fusion 19 (1979) 461.

[7] NGAN, Y., et al., Phys. Fluids 20 (1977) 1920.

[8] IIZUKA, S., et al., Phys. Rev. Lett. 45 (1980) 1256.

$$B_T = 12 \text{ kG}$$
$$n_H/n_D \sim 10\%$$

- • $\bar{n}_e \sim 4 \times 10^{13} \text{cm}^{-3}$
- ∘ $\sim 3 \times 10^{13} \text{cm}^{-3}$
- △ $\sim 2 \times 10^{13} \text{cm}^{-3}$

without plasma

R_S (Ω)

Δ_H (cm)
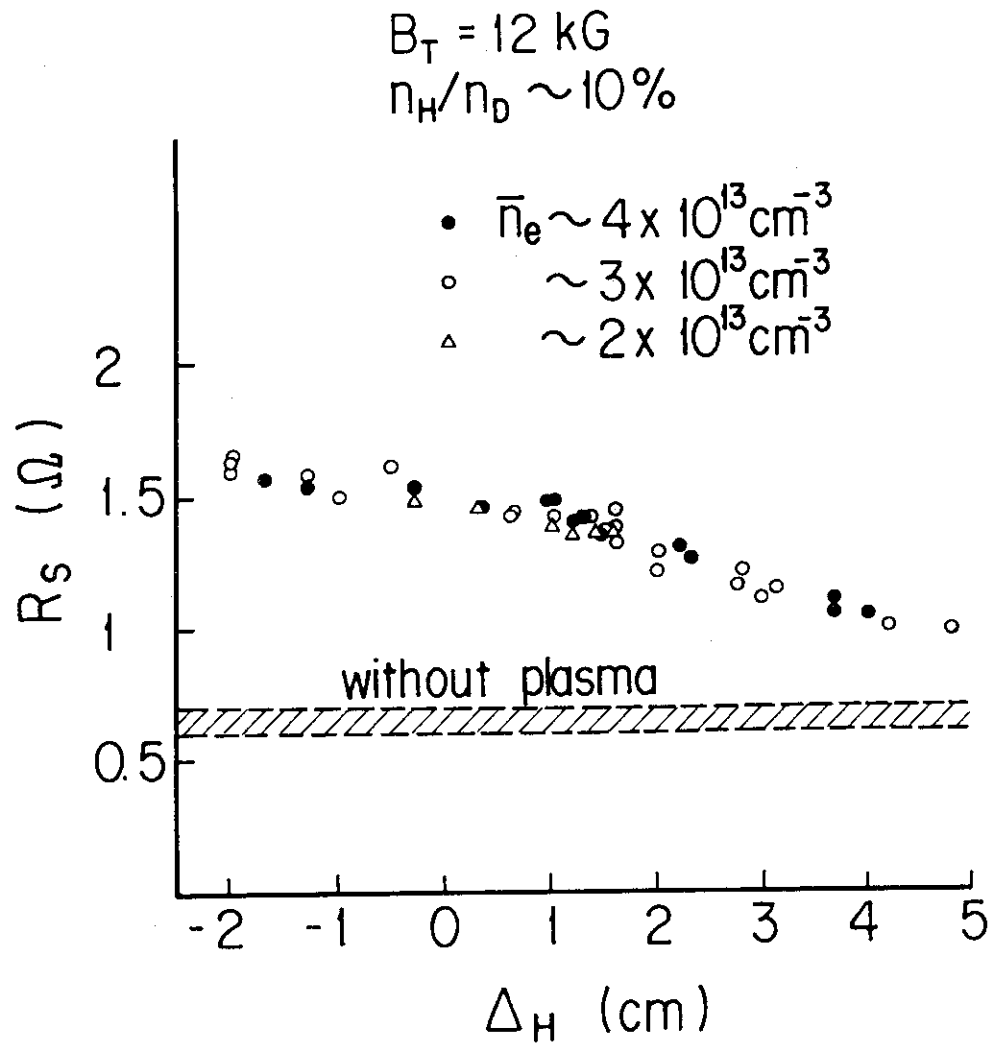
Fig. V-1-1 Antenna loading impedance as a function oo the horizontal

position of the plasma column in JFT-2 experiment. The

antenna is located inside of the torus.

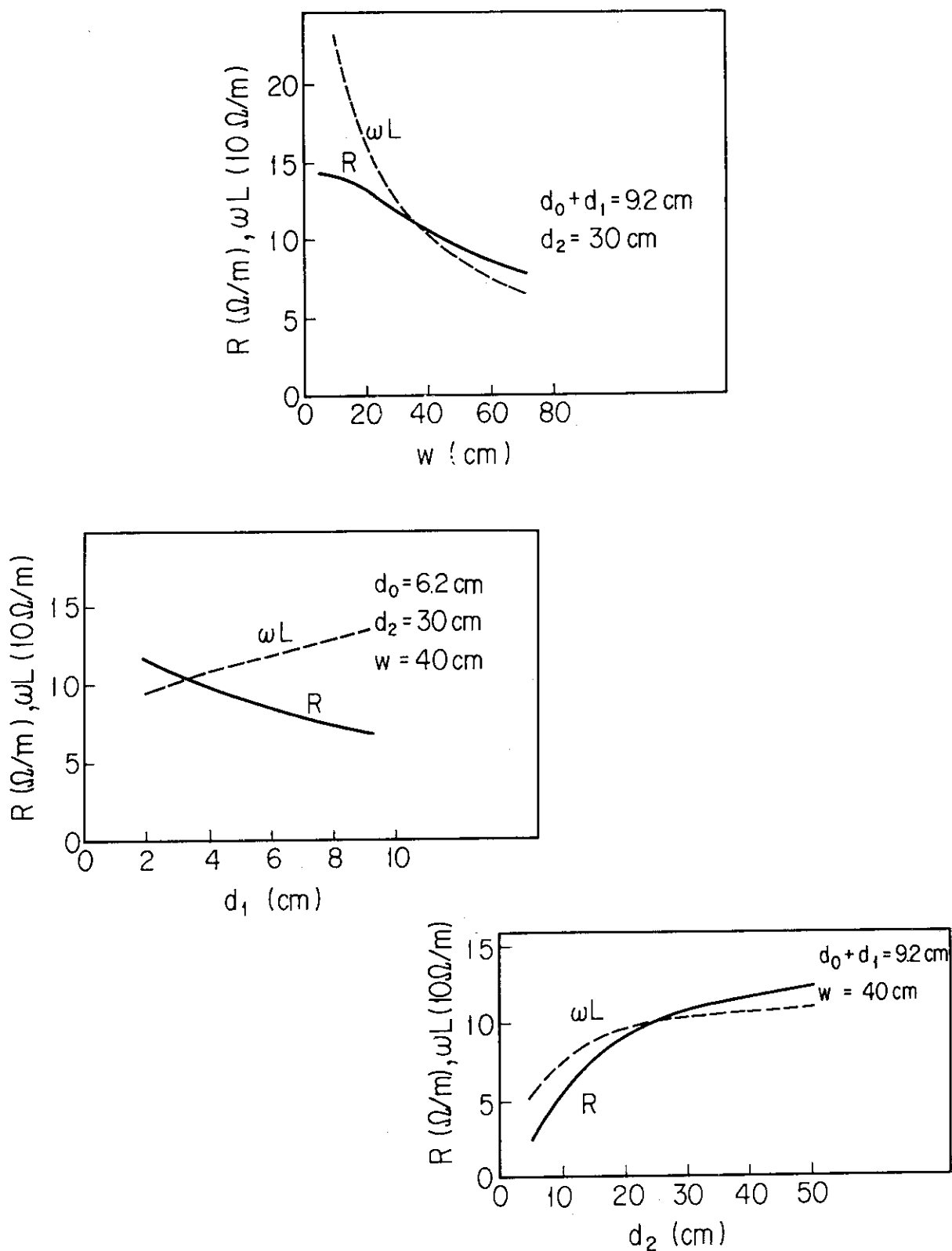# ICRF Antenna
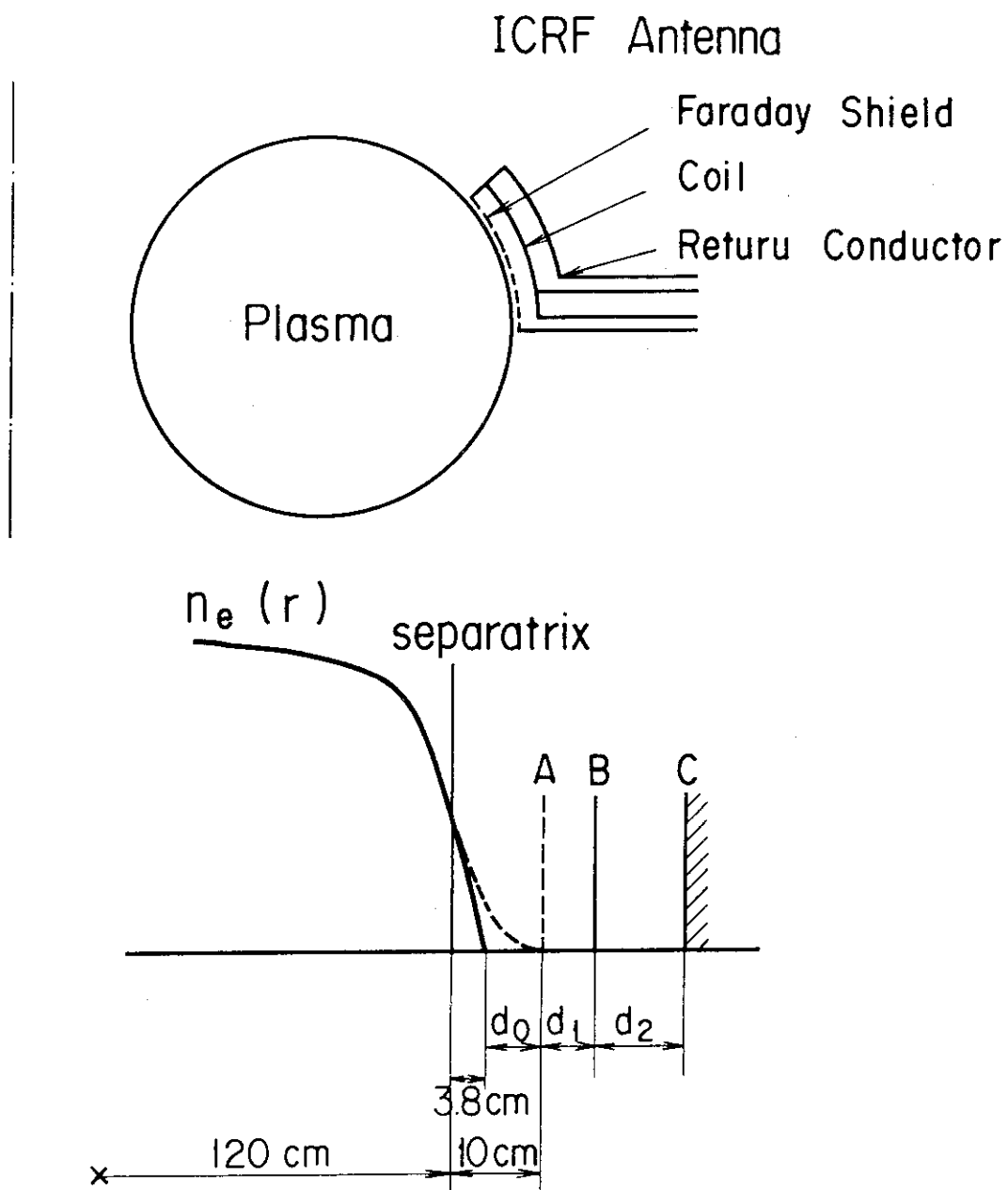
Fig. V-1-2 Schematic drawing of the antenna and the calculation model.

Fig. V-1-3 Real and imaginary components of the antenna loading impedance as a function of d_0+d_1, d_2 and w. The electron density profile is assumed $n_e = n_{e0}(1 - \frac{r^4}{a^4})$. $n_{e0} = 1.5 \times 10^{14}$ cm^{-3}, a = 123.8 cm, $d_0 = 6.2$ cm and f = 85 MHz.
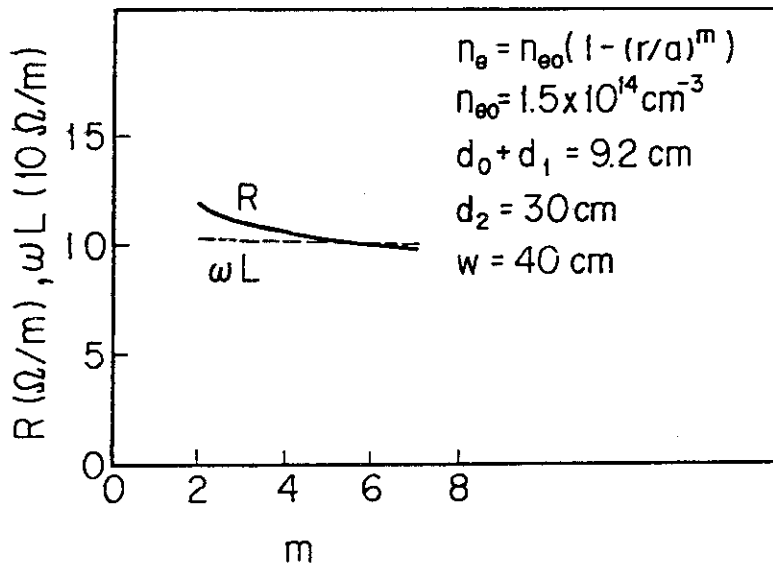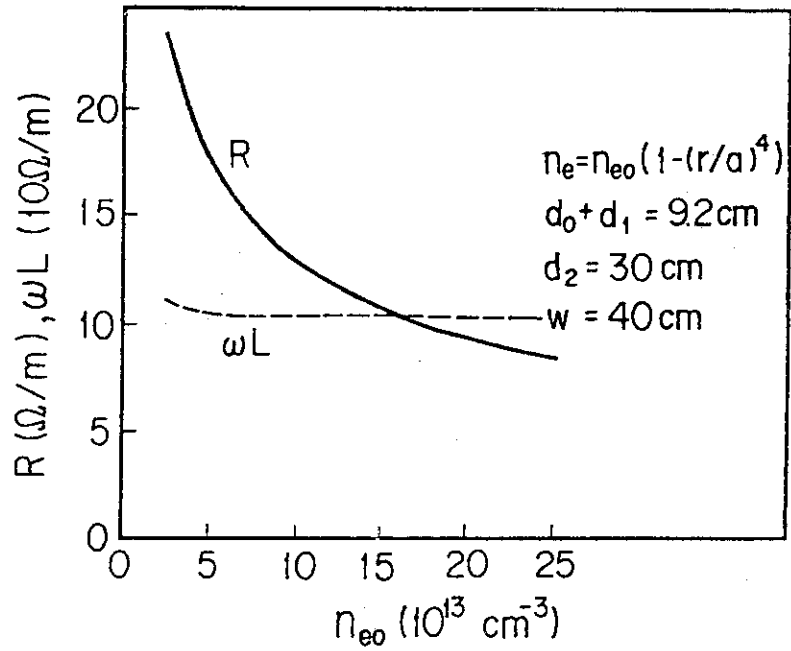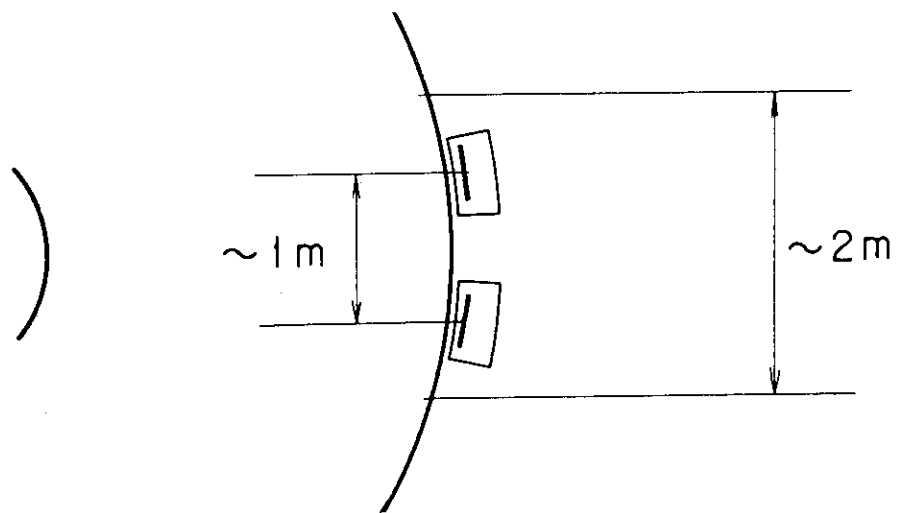
Fig. V-1-4 Change of the loading impedance with the peak electron
density and the density profile. $d_0 + d_1 = 9.2$ cm, $d_2 = 30$ cm
and w = 40 cm.
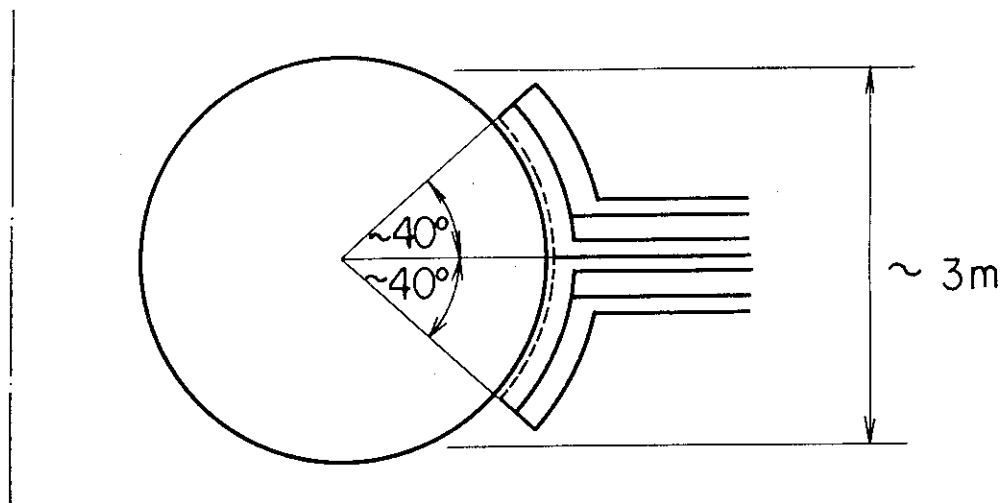
Cross - sectional View
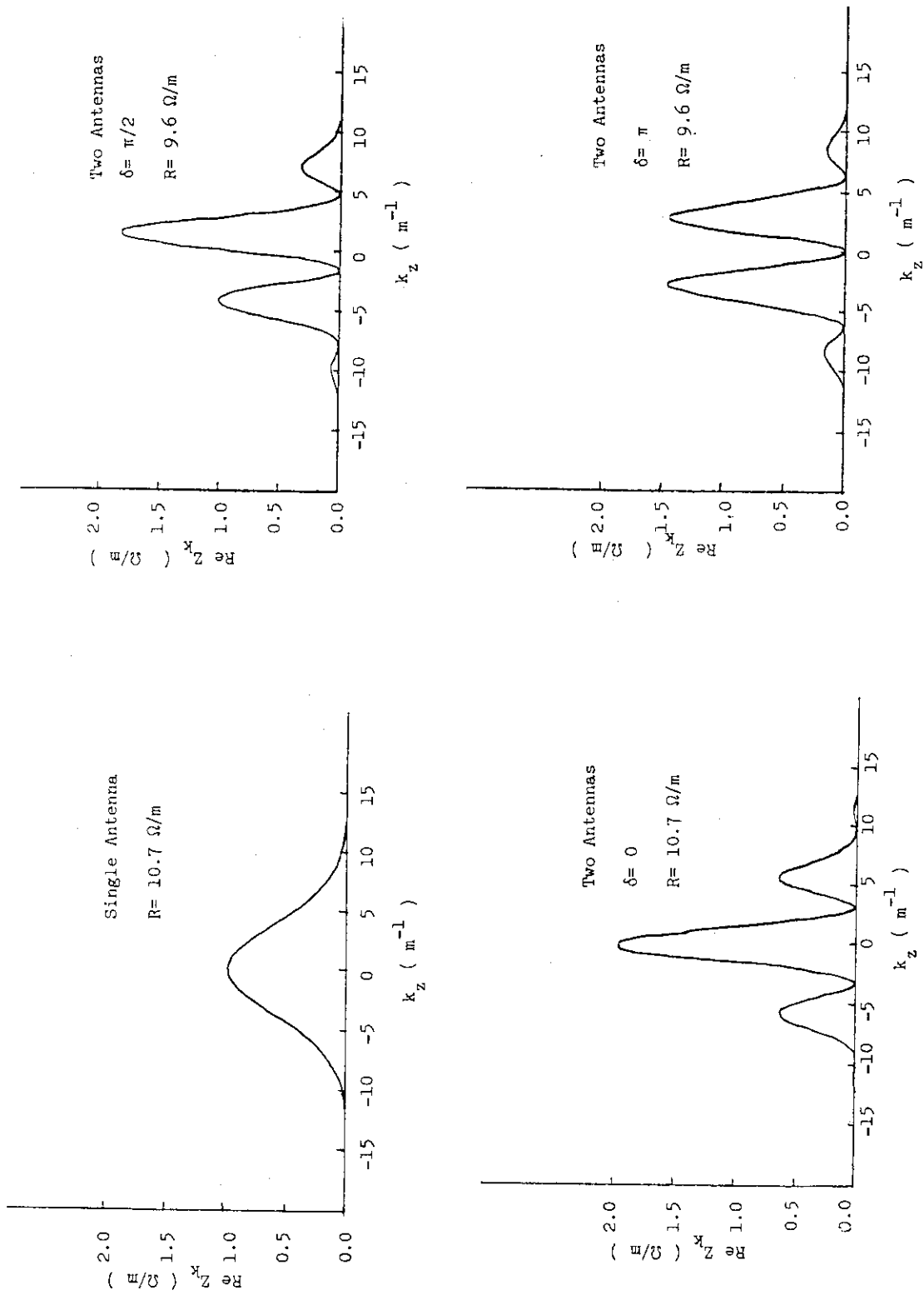
Top View

Fig. V-1-5   Schematic drawing of the four antenna system.

Fig. V-1-6 k_z spectrum of the real component of the loading impedance for a single antenna and two antennas with various phasing.
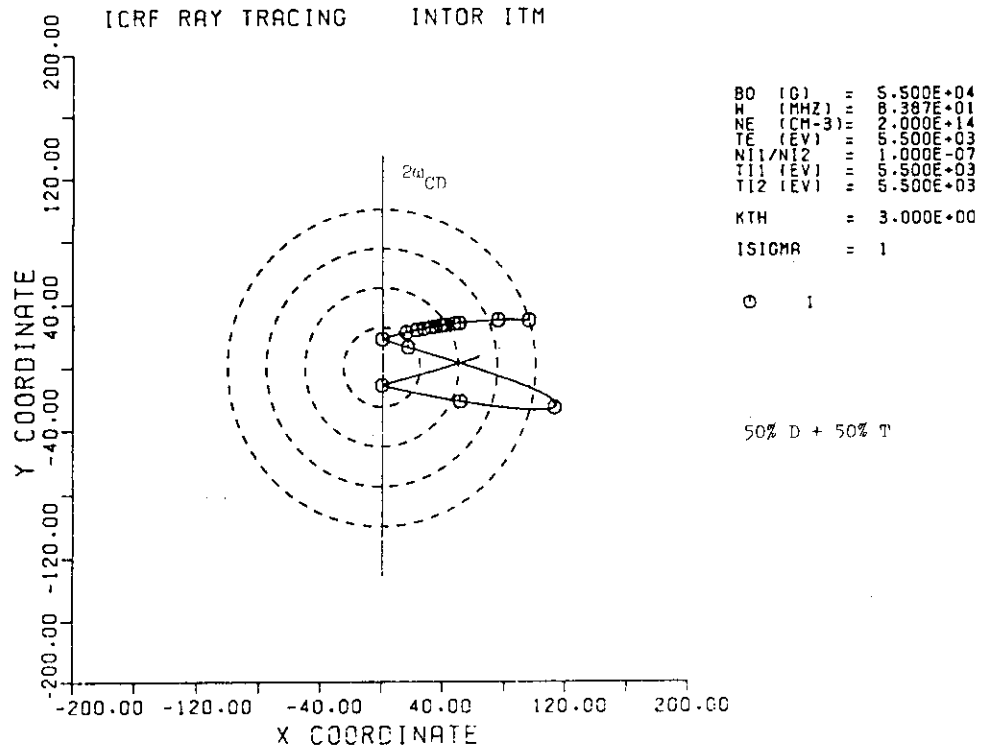
ICRF RAY TRACING   INTOR ITM

Fig. V-1-7(a)

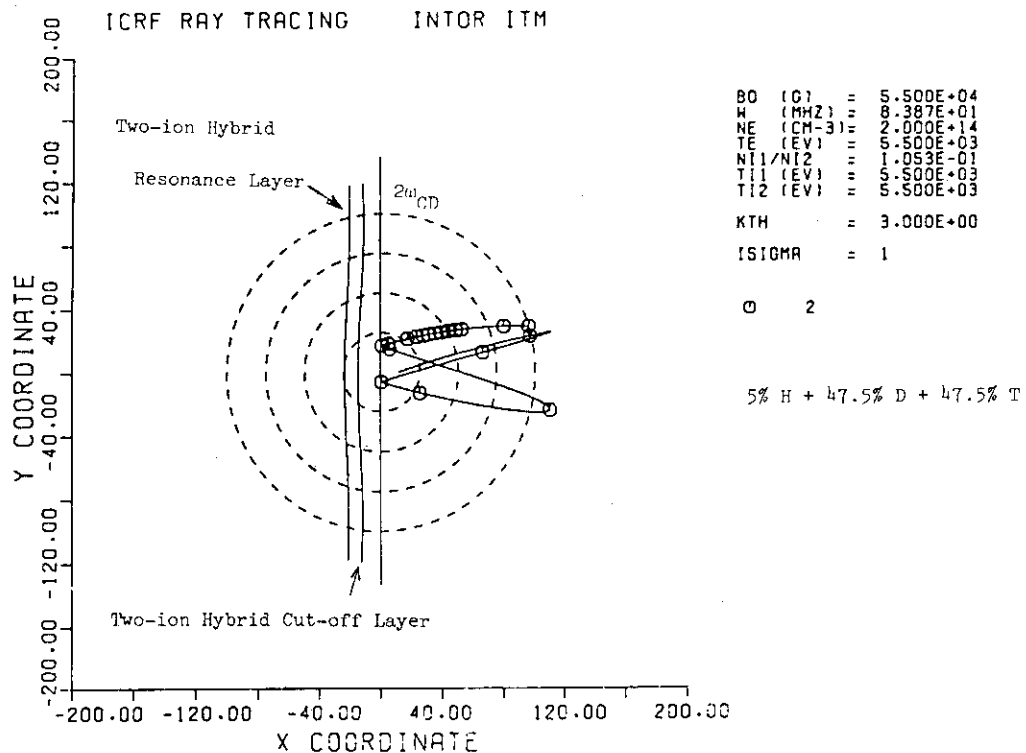ICRF RAY TRACING   INTOR ITM

Fig. V-1-7(b)

Fig. V-1-7   Ray trajectory in the poloidal cross-section.   (a) the

deuteron second harmonic heating case (50% D + 50% T),

and (b) the proton minority heating case (5% H + 47.5% D +
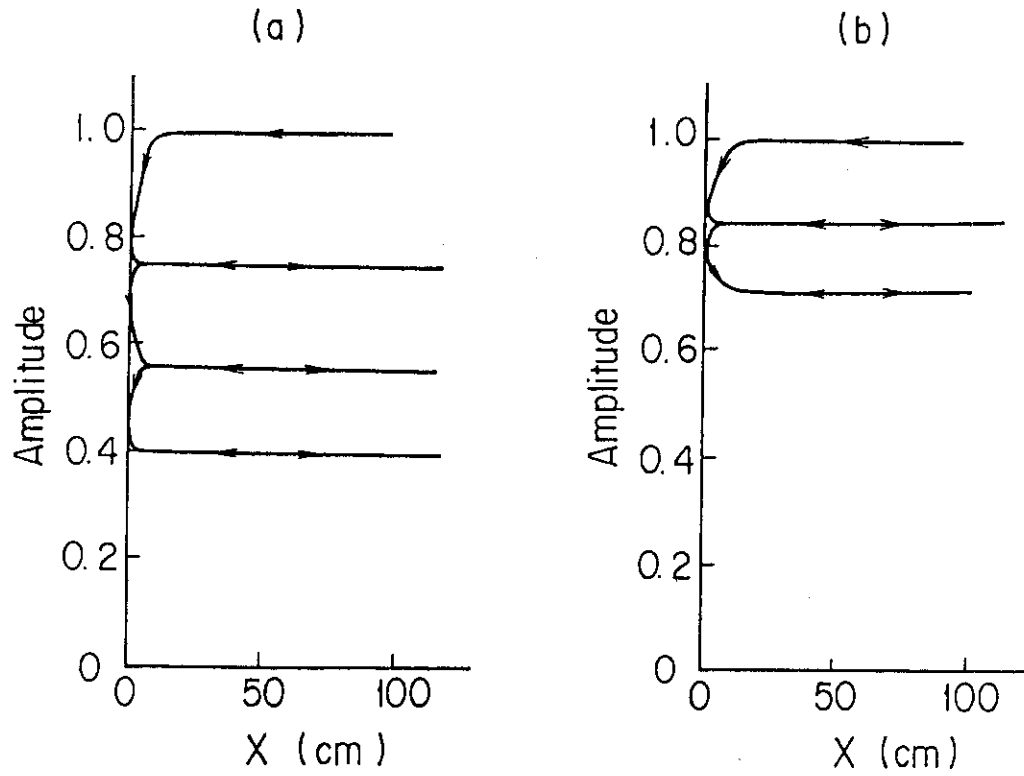
47.5% T). $q_0 = 1.0$ and $q_a = 2.3$.

Fig. V-1-8 Damping of the wave amplitude along the ray trajectory of

Fig. 7.   (a) the deuteron second harmonic heating case, and

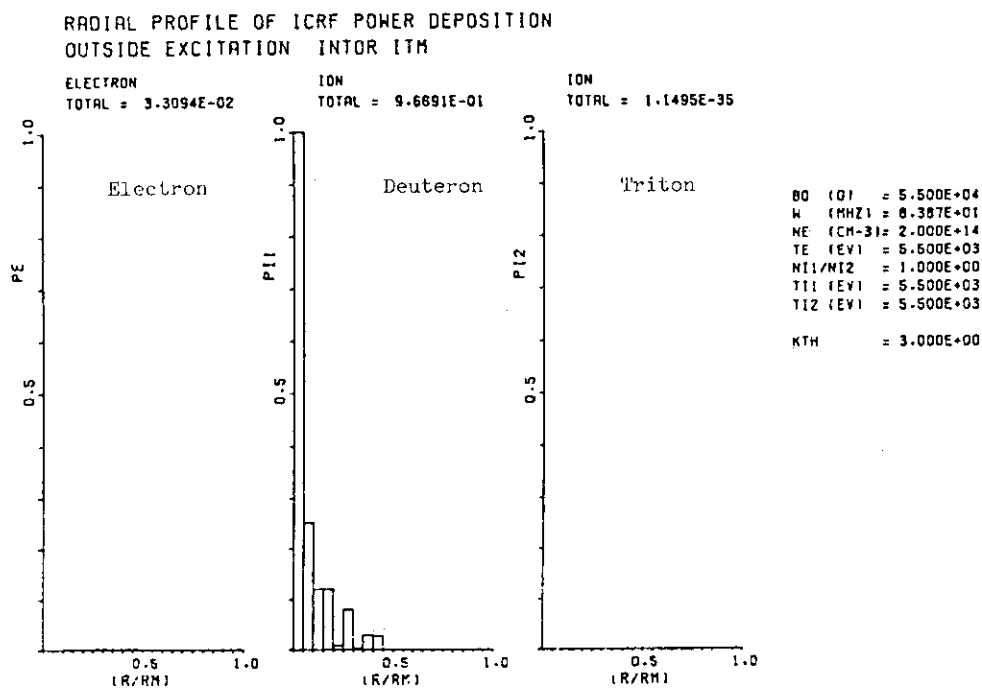(b) the proton minority heating case.

RADIAL PROFILE OF ICRF POWER DEPOSITION
OUTSIDE EXCITATION   INTOR ITM

ELECTRON
TOTAL = 3.3094E-02

ION
TOTAL = 9.6691E-01

ION
TOTAL = 1.1495E-35

Electron

Deuteron

Triton

BO (O) = 5.500E+04
W   (MHZ) = 8.387E+01
NE (CM-3)= 2.000E+14
TE (EV) = 5.500E+03
NI1/NI2   = 1.000E+00
TI1 (EV) = 5.500E+03
TI2 (EV) = 5.500E+03

KTH   = 3.000E+00

PE

PI1

PI2

0.5
(R/RM)

1.0

0.5
(R/RM)

1.0

0.5
(R/RM)

1.0

Fig. V-1-9(a)

RADIAL PROFILE OF ICRF POWER DEPOSITION
OUTSIDE EXCITATION   INTOR ITM

ELECTRON
TOTAL = 3.4461E-02

ION
TOTAL = 9.1449E-01

ION
TOTAL = 5.1047E-02

Electron

Proton

Deuteron

BO (O) = 5.500E+04
W   (MHZ) = 8.387E+01
NE (CM-3)= 2.000E+14
TE (EV) = 5.500E+03
NI1/NI2   = 1.053E-01
TI1 (EV) = 5.500E+03
TI2 (EV) = 5.500E+03

KTH   = 3.000E+00

PE

PI1

PI2

0.5
(R/RM)

1.0

0.5
(R/RM)
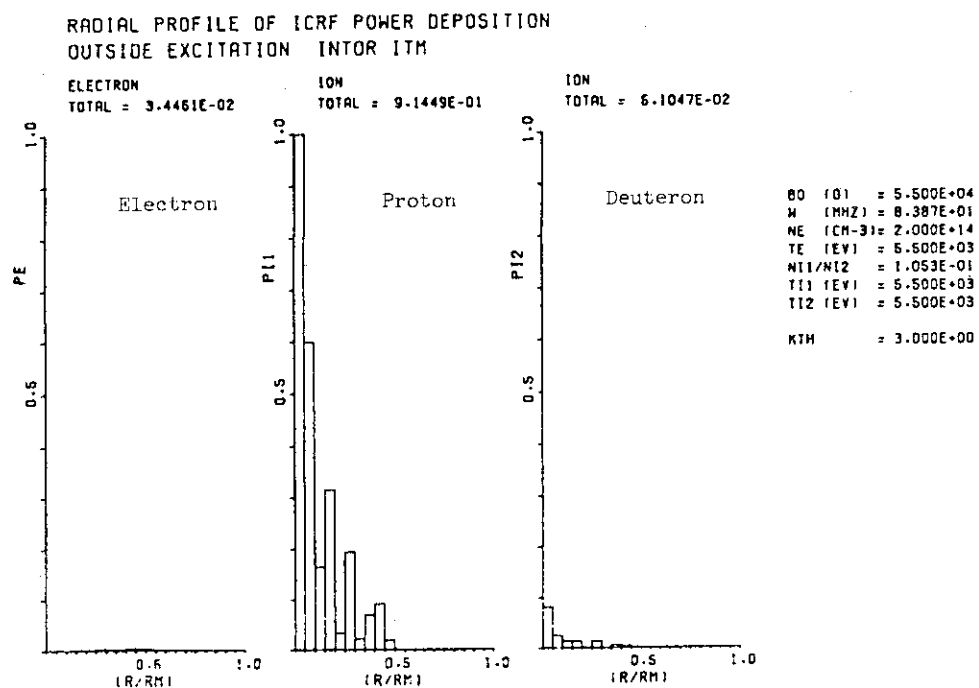
1.0

0.5
(R/RM)

1.0

Fig. V-1-9(b)

Fig. V-1-9   Power deposition profile to each species. (a) the deuteron

second harmonic heating case, and (b) the proton minority

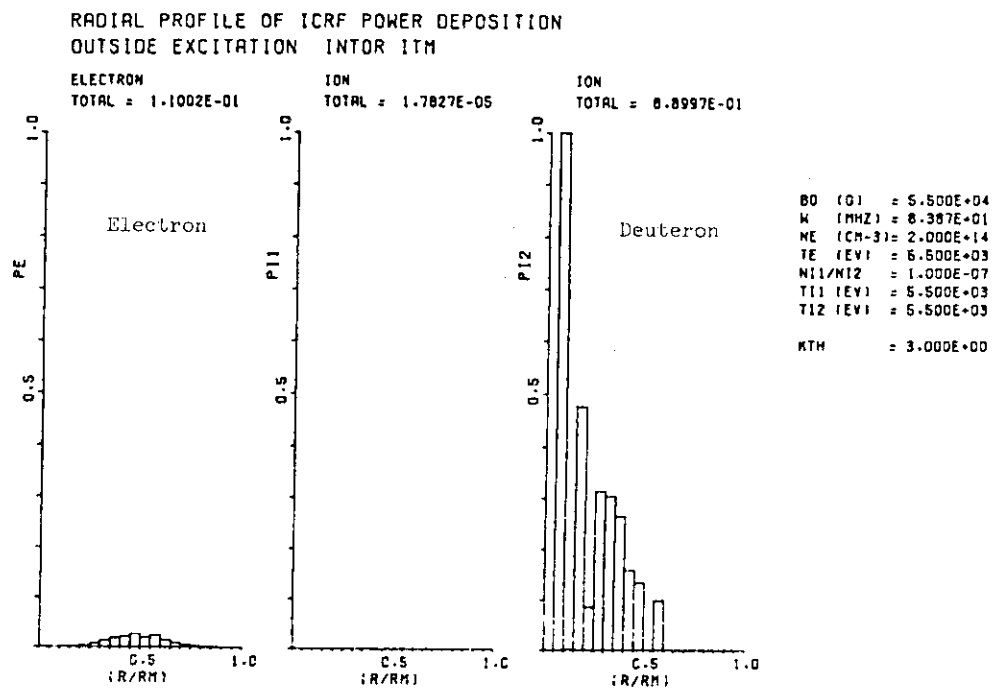heating case. The density profile is parabolic.

RADIAL PROFILE OF ICRF POWER DEPOSITION
OUTSIDE EXCITATION INTOR ITM

ELECTRON
TOTAL = 1.1002E-01

ION
TOTAL = 1.7827E-05

ION
TOTAL = 8.8997E-01

Electron

Deuteron

BO (G)   = 5.500E+04
W   (MHZ) = 8.367E+01
NE (CM-3)= 2.000E+14
TE (EV) = 6.500E+03
NI1/NI2   = 1.000E-07
TI1 (EV) = 5.500E+03
TI2 (EV) = 5.500E+03

KTH   = 3.000E+00

Fig.V-1-10 Power deposition profile of the deuteron second harmonic

case with the density profile $n = n_0 (1 - (\frac{r}{a})^6)$.

RADIAL PROFILE OF ICRF POWER DEPOSITION
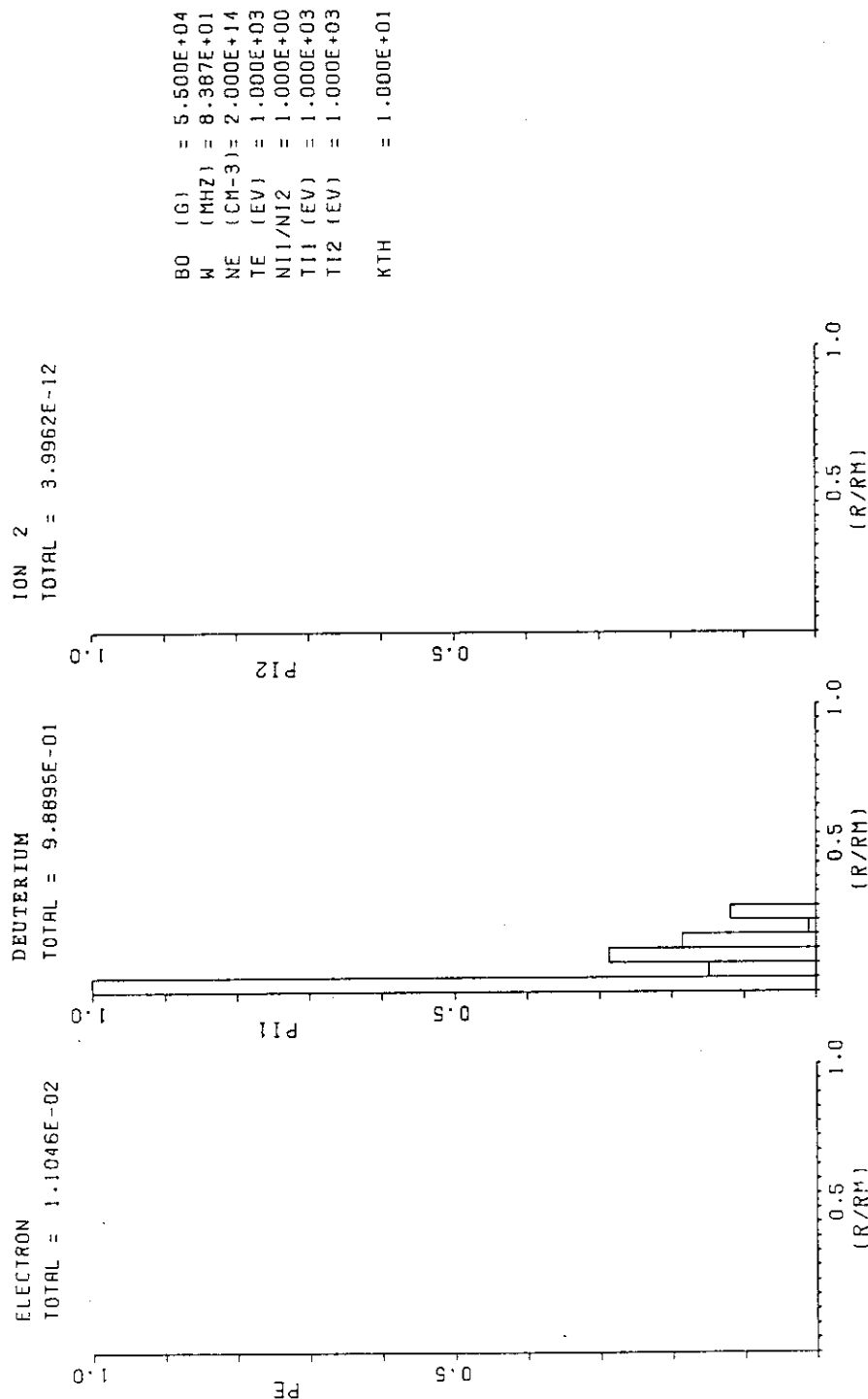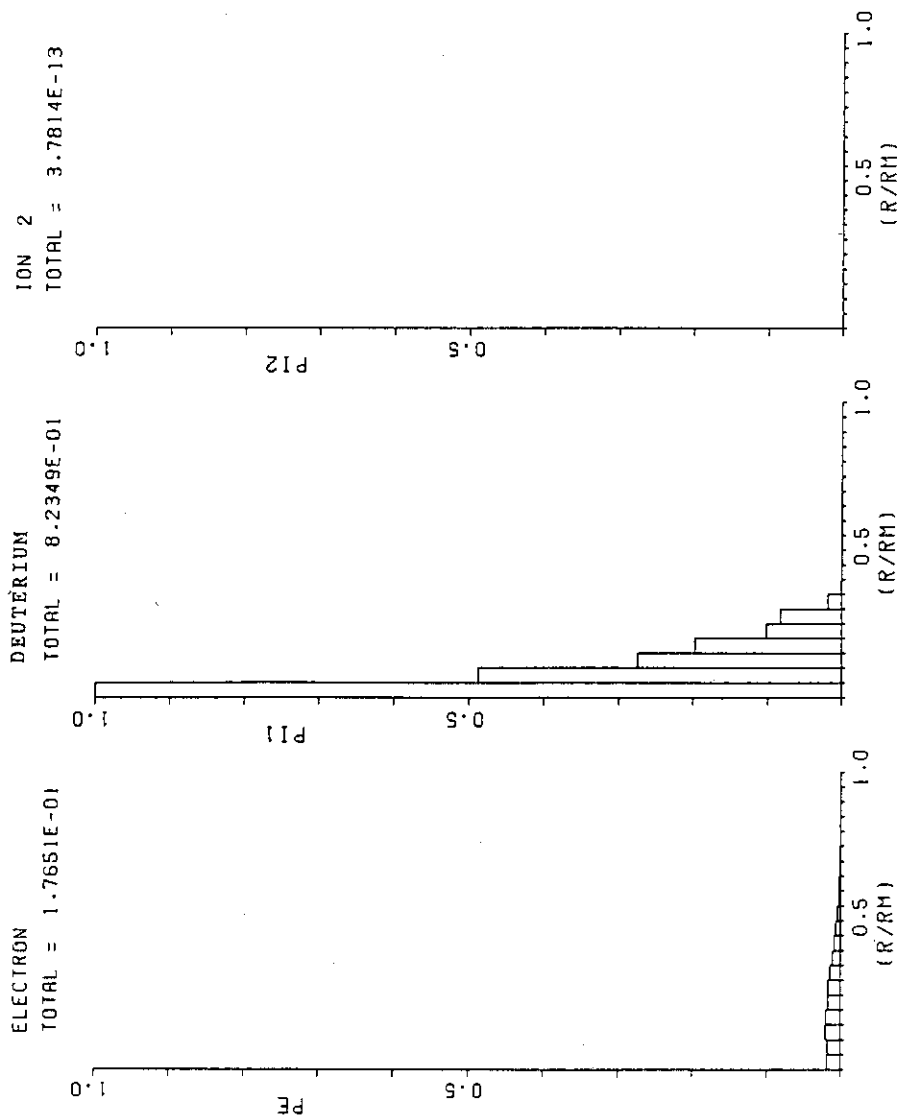OUTSIDE EXCITATION INTOR 1keV

ELECTRON
TOTAL = 1.1046E-02

DEUTERIUM
TOTAL = 9.8895E-01

ION 2
TOTAL = 3.9962E-12

BO (G)	=	5.500E+04
W (MHZ)	=	8.387E+01
NE (CM-3)	=	2.000E+14
TE (EV)	=	1.000E+03
NI1/NI2	=	1.000E+00
TI1 (EV)	=	1.000E+03
TI2 (EV)	=	1.000E+03
KTH	=	1.000E+01

Fig. V-1-11(a)

Fig. V-1-11 Radial power deposition profiles of electrons and deuterons.

(a) T_{eo} = 1 keV, (b) T_{eo} = 5 keV, (c) T_{eo} = 10 keV,

(d) T_{eo} = 15 keV and (e) T_{eo} = 20 keV.

Fig. V-1-11(b)

Fig. V-1-11(c)

RADIAL PROFILE OF ICRF POWER DEPOSITION
OUTSIDE EXCITATION INTOR 15keV

BO (G)   = 5.500E+04
W   (MHZ) = 8.387E+01
NE (CM-3) = 2.000E+14
TE (EV)   = 1.500E+04
NI1/NI2   = 1.000E+00
TI1 (EV)   = 1.500E+04
TI2 (EV)   = 1.500E+04

KTH   = 1.000E+01
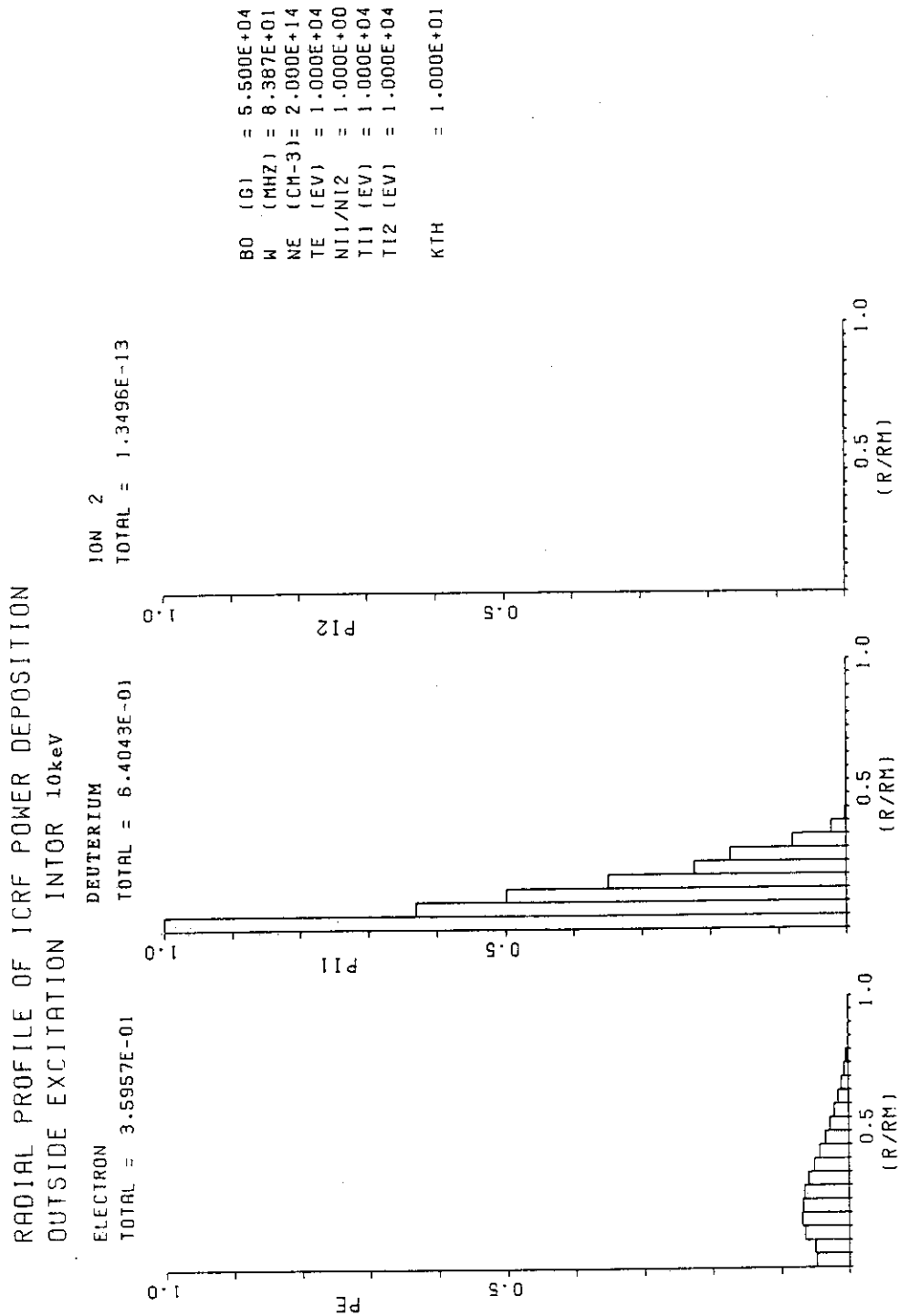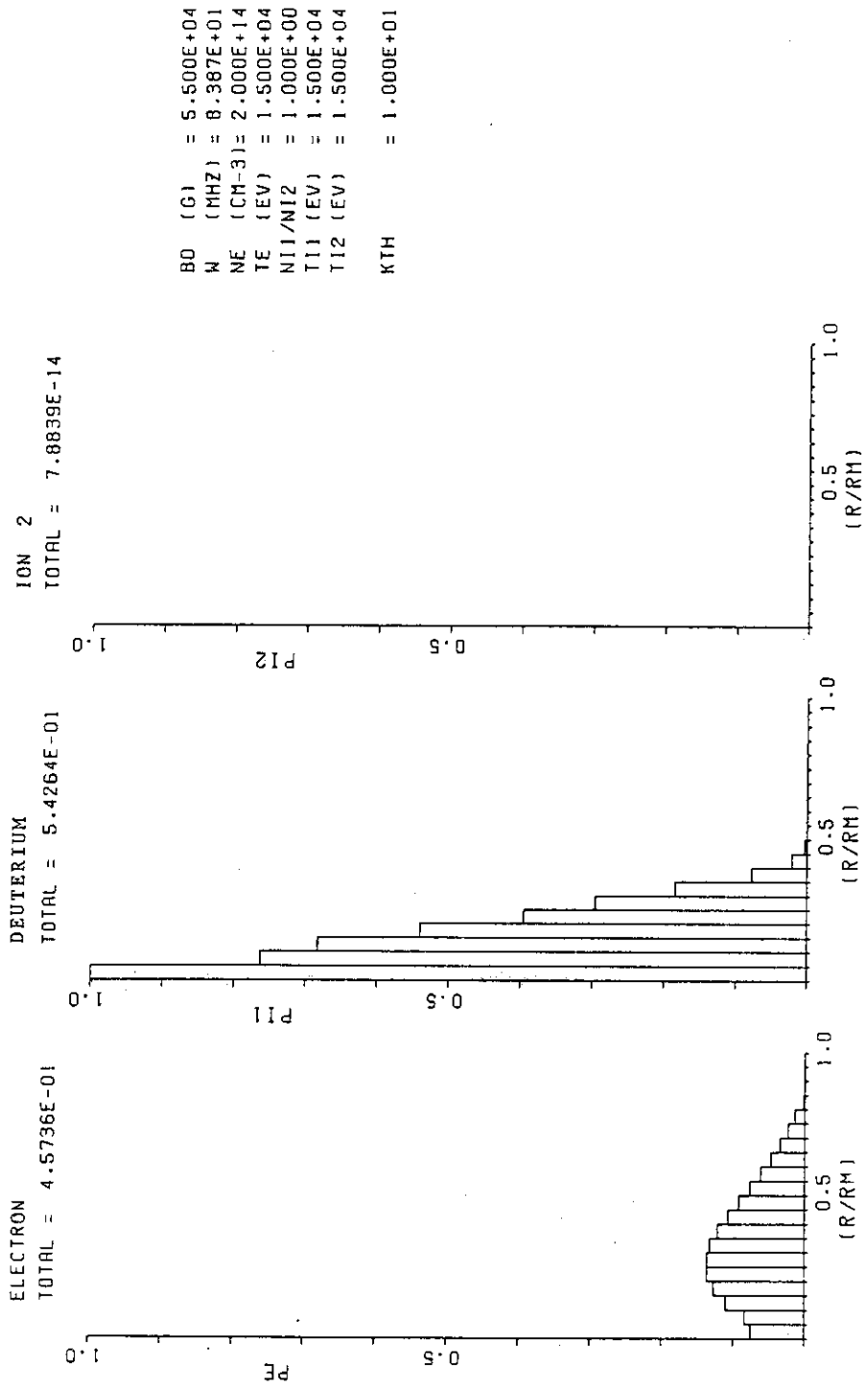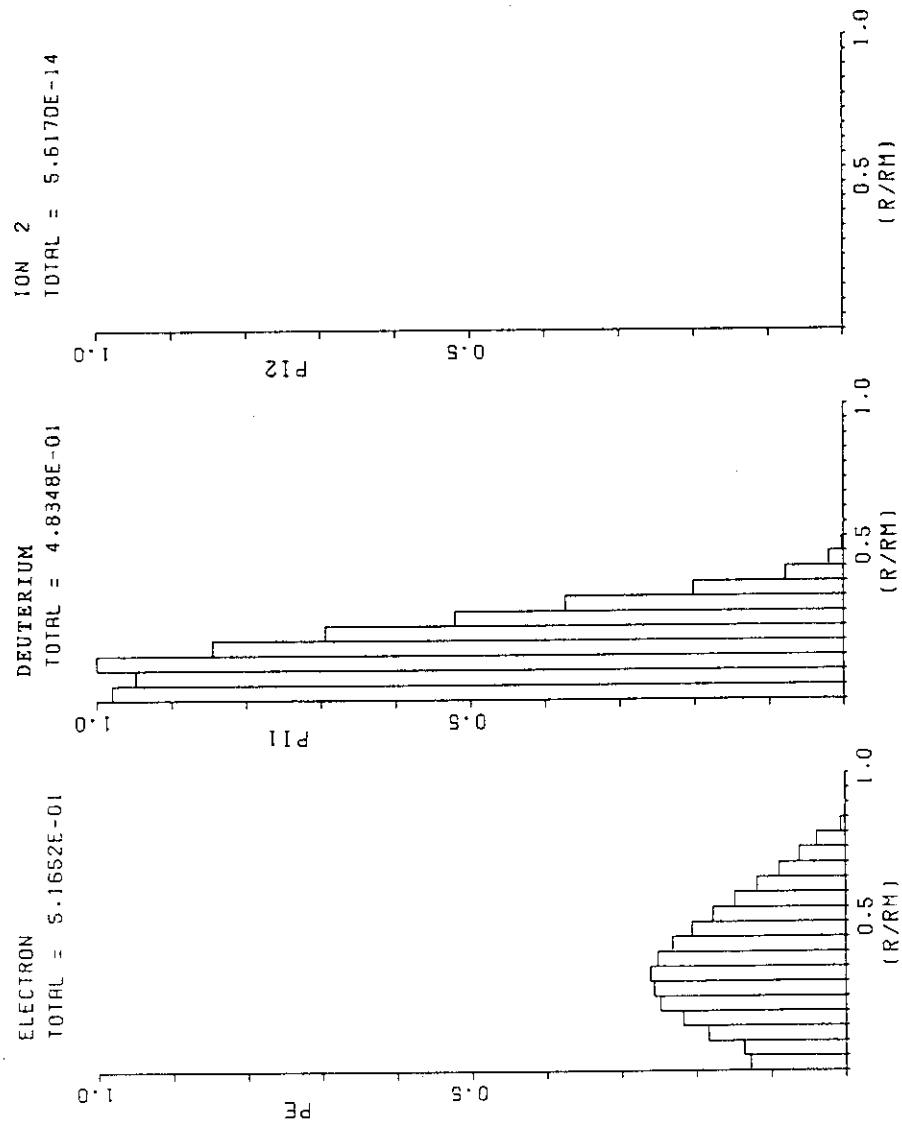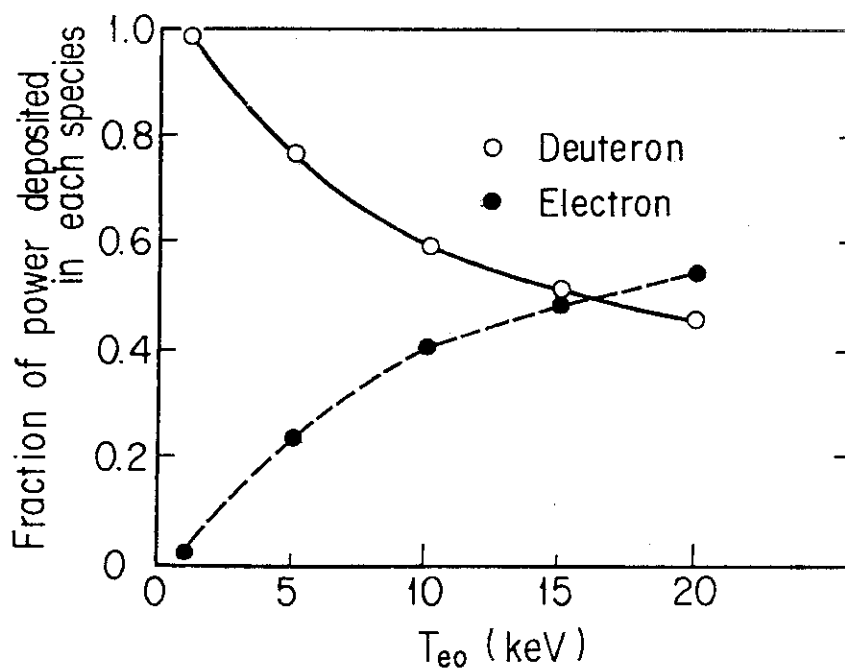
ELECTRON
TOTAL = 4.5736E-01

DEUTERIUM
TOTAL = 5.4264E-01

ION 2
TOTAL = 7.8839E-14

Fig. V-1-11(d)

RADIAL PROFILE OF ICRF POWER DEPOSITION
OUTSIDE EXCITATION INTOR 20KEV

ELECTRON
TOTAL = 5.1652E-01

DEUTERIUM
TOTAL = 4.8348E-01

ION 2
TOTAL = 5.6170E-14

BO (G)	= 5.500E+04
W (MHZ)	= 8.387E+01
NE (CM-3)	= 2.000E+14
TE (EV)	= 2.000E+04
NI1/NI2	= 1.000E+00
TI1 (EV)	= 2.000E+04
TI2 (EV)	= 2.000E+04
KTH	= 1.000E+01

Fig. V-1-11(e)

Fig. V-1-12 Fraction of power deposited in deuterons (o) and electrons (o) as a function of T_{eo}.

INTOR 2 ω_{cD}
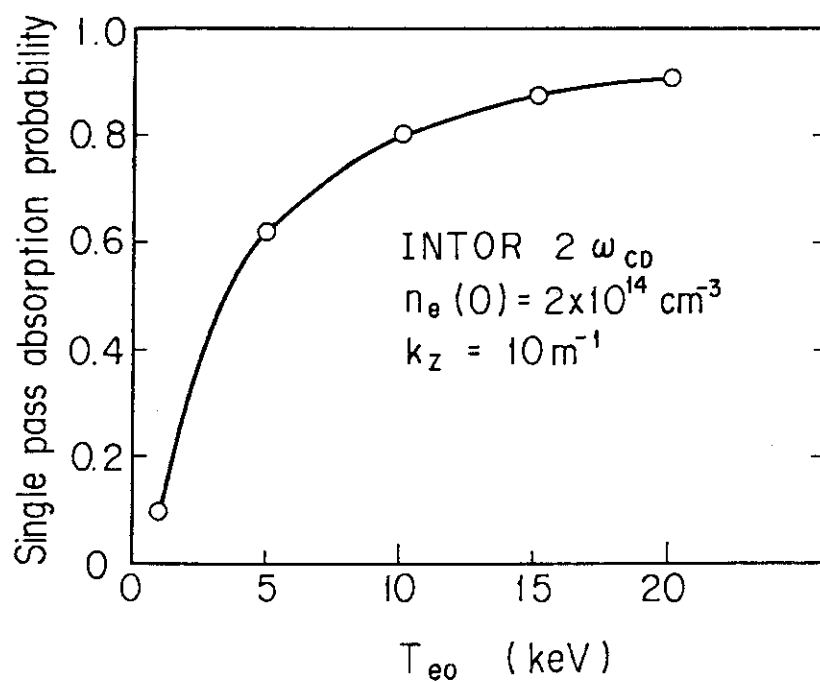$n_e (0) = 2 \times 10^{14} \ cm^{-3}$
$k_z = 10 \, m^{-1}$

Fig. V-1-13 Single pass absorption probability as a function of T_{eo}.
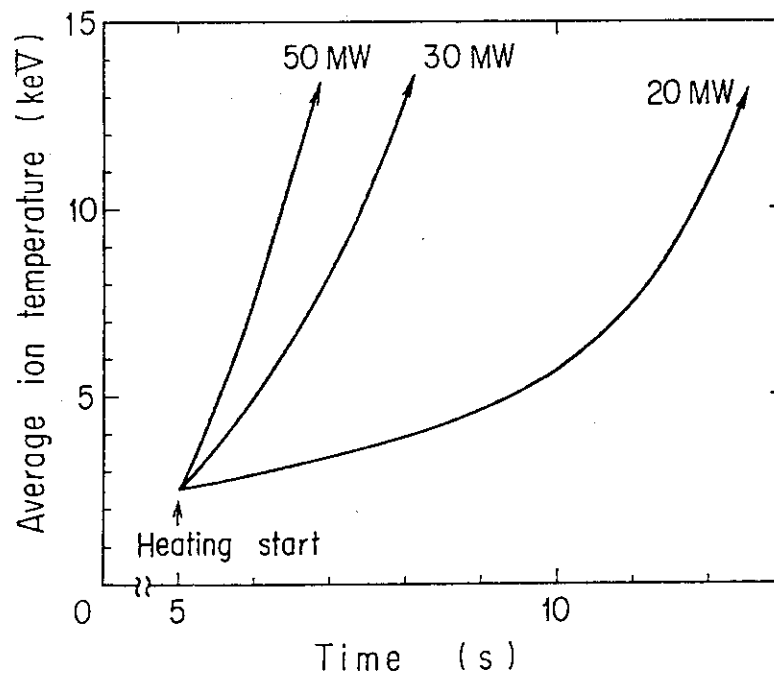
Fig. V-1-14´   Preliminary calculation of ignition approach by ICRf heating

in INTOR plasma for various heating power. Power deposition

profile is constant during heating phase.

1.2 Lower hybrid heating to ignition

T. IMAI (JAERI)

A. FUKUYAMA (Okayama Univ.)

M. OKAMOTO (Nagoya Univ.)

T. NAGASHIMA (JAERI)

§1. Overview of LHRF heating in INTOR

Lower Hybrid Range of Frequencies (LHRF) heating is very attractive as a further heating method of a plasma of a tokamak reactor, because of its engineering simplicities. One of them is the power source. A megawatt class klystron of a few GHz is comparatively easy to develope. Actually R&D of a MW klystron of 2 GHz for JT-60 has already begun in JAERI[1]. Another is the antenna system. Waveguide coupling which has many attractive points in a reactor environment is possible. Thirdly, required area to inject RF power is small, because of the large power density limit. Power density of 3-4 kW/cm^2 is expected to be available from the present experimental results, which enables to inject 50 MW with port area less than 2 m^2[2].

In addition to these engineering attractiveness, recent experiments in JFT-2, Alcator A and PLT showed good plasma heating [2,3]. LHRF enables other advanced concepts, besides the bulk plasma heating, like ion tail formation to enhance fusion power, RF current drive to operate tokamak in steady state and plasma profile control for plasma stability [2,4].

Lower hybrid resonance frequency is the ion plasma frequency in the space filled with the magnetically constrained electrons. Therefore, LHRF heating is sensitive to the ion density just like as that ICRF and ECH are sensitive to the magnetic field. Before the arrival

of the lower hybrid wave (LHW) to the resonance point, there are several processes which the wave must experience.

At first, the wave is launched from the outside of plasma. In the LHRF, waveguides, which are attractive in a reactor environment and easy to be formulated theoreticaly, are possible to use. Electromagnetic wave radiated from the launcher couples to the slow wave at the edge and propagates to the interior in the linear theory of the LHW. It is well known that a slow wave must satisfy the accessibility condition in order to penetrate further inside. The accessibility is approximately given as $N_z > 1 + \omega_{pe}^2/\omega_{ce}^2|_{res}$, where $|_{res}$ denotes the value at the lower hybrid resonance point [5]. After the penetration into the core of plasma, the wavelength become shorter. The wave is converted to the hot ion wave due to the thermal effect of ions and is absorbed near the turning point via the ion cyclotron harmonic damping and/or Landau damping. Above linear heating model is very simple and easy to understand, but the experimental results are somehow different from it. It seems to be indispensable to apply nonlinear consideration to understand the experimental results. There are many nonlinear theory of the LHW. Among them, parametric instabilities and nonlinear stochastic heating are very plausible. Parametric instabilities were observed in every LHRF heating experiment in tokamaks. But the role of them seems to be a mechanism of surface heating. Some attempt to reduce parametric instabilities near the surface have been made [6]. In the reactor grade tokamak parameters, this surface absorption will not be serious problem, since the ratio of the RF power density and plasma energy density $R_N = S^{RF}/nT$ will be a few hundredths of that of the present experiments.

Almost every LHRF heating experiment has predicted the necessity of the accessibility condition and the turning point of the LHW [2].

From these prediction, we can easily find the importance of the penetration of the LHW into the core plasma and mode conversion to the short wavelength ion waves. Since the linear damping mechanism like ion cyclotron harmonic damping and Landau damping saturate easily at low power, the ion wave accumulates in the core plasma and nonlinear stachastic heating is expected to occur near the turning point [7].

Heating efficiency of the LHRF (1.5 ∿ 3.0 eV/kW) is moderate, compared with the other heating schemes like NBI, ICRF and ECH (3 ∿ 6 eV/kW) in the present grade tokamak experiments. As mentioned before, this reduction of the heating efficiency is mainly due to the surface absorption which will be probably suppressed in the reactor plasma and a ripple loss or an orbit loss of perpendicular energetic ions which will also be confined in the reactor plasma. Thus the LHRF heating will be expected to work well in the reactor plasma like INTOR. Weak point of the LHRF heating in the present time is the lack of the experiments to demonstrate the excellent heating efficiency. Coming experiments of the LHRF heating in the PLT, Alcator C, JFT-2M, Wega, Asdex and JT-60 will clarify the present ambiguity soon.

§2. Preliminary results on antenna coupling and wave propagation studies

Determination of the RF parameters for INTOR is the first step of the design of the RF system. For this purpose, propagation properties of the LHW in plasma and RF parameter spaces are investigated, which are shown in Figs. V-1-14 and 15. In the figure V-1-14, the solid lines show the density of the Linear Mode Conversion point (LMC) of the LHW as a function of the input frequency and refractive index parallel to the magnetic field N_z. The dotted line is the density limit of the

accessibility condition of slow wave. Below this density LHW can
penetrate. Since the peak density of the INTOR is $1.5 - 2.0 \times 10^{20}$
m^{-3}, the frequency of $1.8 - 2.0$ GHz and $N_z = 1.6 - 2.5$ are appropriate.
In the figure V-1-15, the property of the LHW propagation with $f = 2.0$
GHz is shown, where the dotted line of large points is the lower hybrid
resonance, the solid lines are the mode conversion point of each N_z-
wave from the cold LHW to the hot ion wave, the dotted lines are mode
conversion point from slow wave to fast wave (accessibility condition)
and the broken line is an example of the plasma profile of INTOR. As
seen from the plasma profile of the INTOR, again, refractive index N_z
$= \sim 2$ is the best choice for ion heating in INTOR. An example of the
ray tracing of the LHW with $f = 2.0$ GHz is shown in Fig. V-1-16, where
$n_{e0} = 2.0 \times 10^{20}$ m^{-3} and $T = 5$ keV.

Next, the lauching structure of the LHW must be determined. For
the engineering simplicity, number of waveguides should be small and
the effective area to radiate the RF should be large. But for the
optimization of the wave penetration and absorption, large number of
the waveguides and small width of the each waveguide in the toroidal
direction (b) make a good N_z-spectrum for heating. It is the most
important to harmonize the above competing requirements in order to
get a good heating result in a large machine.

Calculation of the coupling and radiation power spectra is shown
in Appendix V-A. An array of 24 waveguides in toroidal direction with
the size of the each waveguide $b = 28$ mm ($b = 11$ m for current drive and
initial heating) is suitable. The simlified schematics of the launcher
is shown in Fig, V-1-17. Since the RF port size is $2 m \times 3 m$ INTOR, 12
steps of 24 waveguide arrays in poloidal direction is possible to place.
An example of the line up of RF amplifiers is shown in Fig. V-1-18,

where 20 klystron amplifiers of ~MW class are employed to drive 20 slots of 24 waveguide array.

Plasma parameters of INTOR change in time. The plasma density is expected to increase from $\bar{n}_e = 0.4 \times 10^{20}$ m^{-3} to 1.4×10^{20} m^{-3}, the plasma current $I_p = 4$ to 6 MA, and the temperature $<T> = 1.0$ to 10.0 keV. As the lower hybrid frequency is sensitive to the density and it is approximately proportional to the square root of the density, increase in the denisty by factor of 3 requires that in the frequency by 1.7. Thermal correction of the LHRF also requires frequency upshift with increase in an ion temperature. Control of the phasing of the launcher provides a part of the solution to these variation of plasma parameters. But it is impossible to follow to the all parameters in INTOR only by changing the phasing, if the choice of the frequency is only one point. Therefore, feedback control of the frequency is desired in order correspond to the plasma variation. More detiled calculation is done in reference [A1].

References

[1] T. Nagashima, "STATUS OF JT-60 RF HEATING PROGRAM AT JAERI" in IAEA Technical Comittee Meeting on Radio Frequency Heating in Large Fusion Experiments, Princeton, 19-22 October 1981.

[2] T. Imai et al., in Proc. of 4th Top. Conf. on RF Plasma Heating, Austin (1981) C2.: J. J. Shuss, et al., Nuclear Fusion 21 (1981) 472.

[3] J. Stevens, "Lower Hybrid Waveguide Coupling and Heating on PLT" in the same meeting of the Ref [1].

[4] T. Yamamoto et al., Phys. Rev. Lett. 45 (1980) 716.: S.C. Luckhardt,

et al., in Proc. of 4th Top. Conf. on RF Plasma Heating, Austin

(1981) B6.

[5] T. H. Stix, Phys. Rev. Lett. 15 (1965) 878.

[6] N. Suzuki et al., in Proc. of 8th Int. Conf., Brussels (1980) IAEA

IAEA-CN38-T2-3.

[7] A. Fukuyama et al., Phys. Rev. Lett. 38 (1977) 701.: C. F. F.

Karney, Phys. Fluids 21 (1978) 1584.
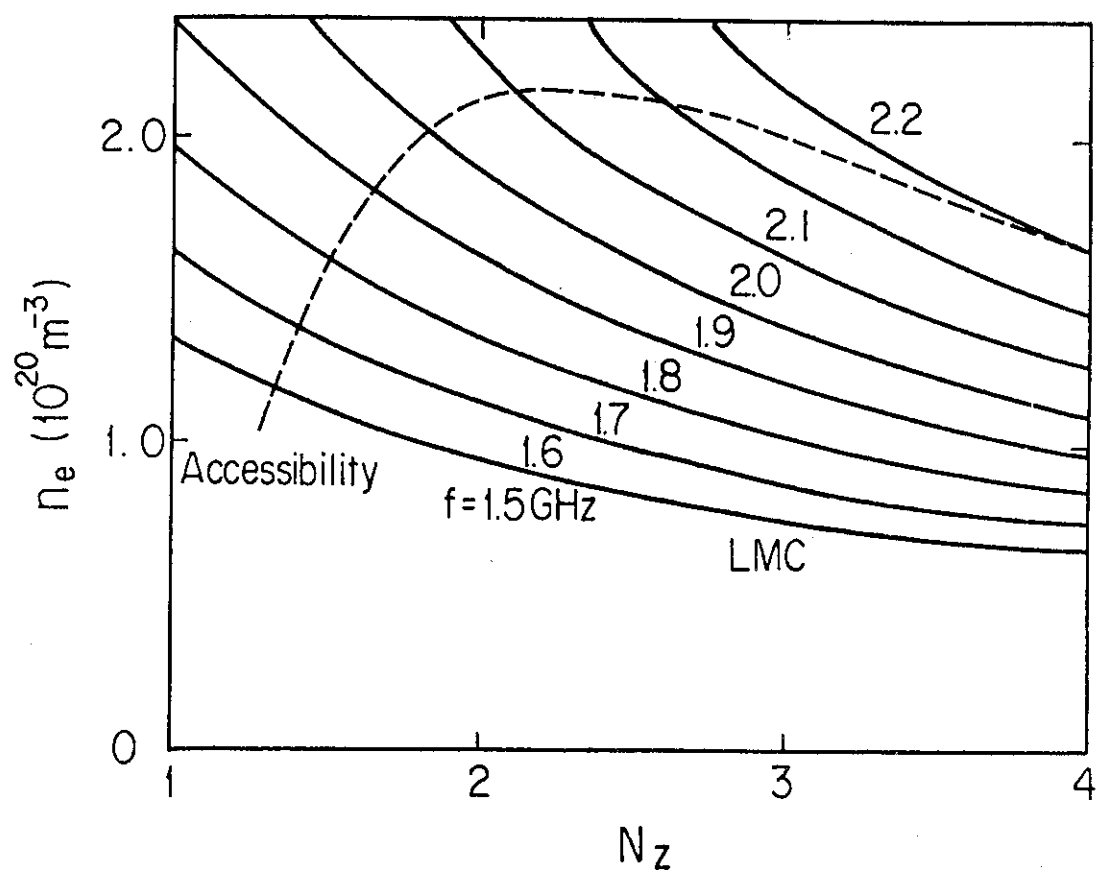
[8] M. Brambilla, Nucl. Fusion 16 (1976) 47.

Fig. V-1-14   Plasma density of LMC (solid lines) and accessibility limit

(dotted line) against the refractive index N_z, as a function

of the input frequency, where T = 5 keV and B_t = 5.4 T.
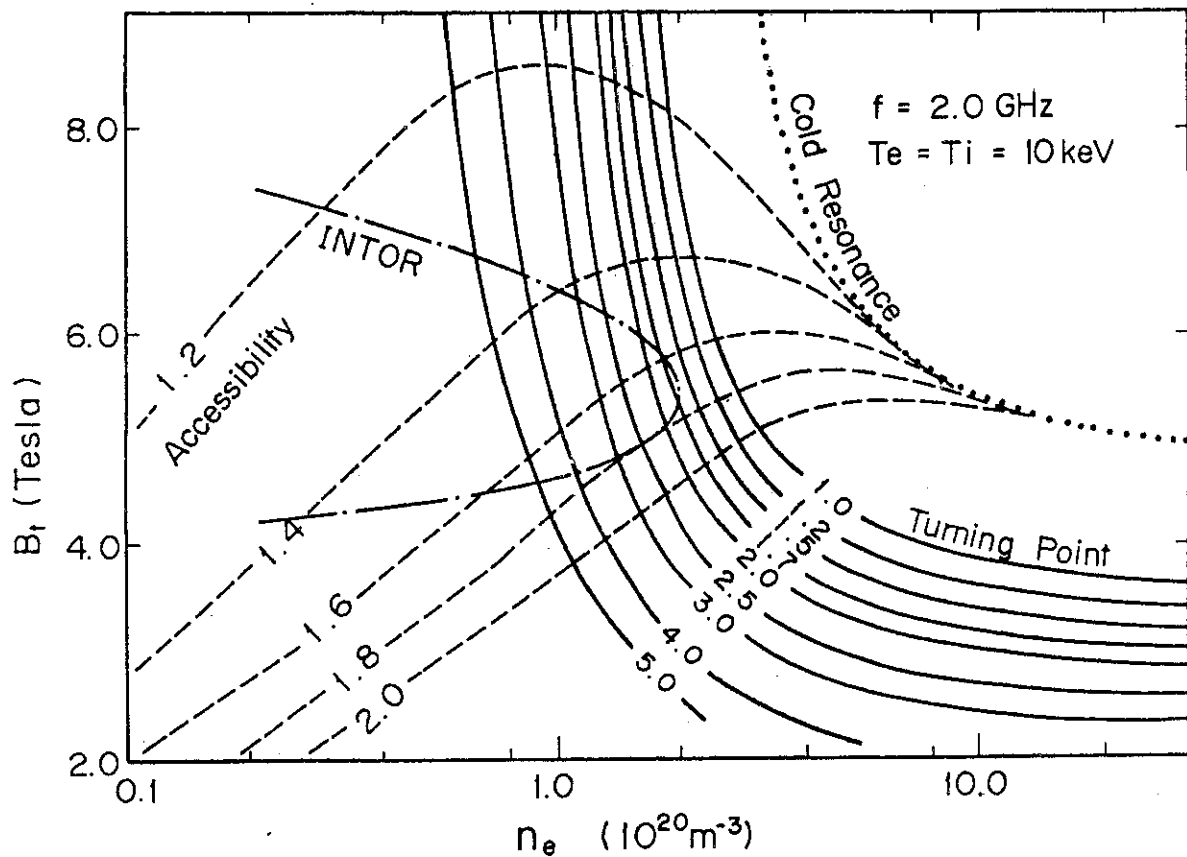
Fig. V-1-15 Wave characteristics in plasma parameter space. The horizontal
and vertical axises show the density and toroidal magnetic
field, respectively. Dotted line of closed circles shows
the cold lower hybrid resonance, solid lines the turning
point from the cold LHW to the hot ion wave of each N_z-wave,
dottted lines the accessibility condition (mode conversion
point from slow wave to fast wave) of each N_z-wave. Mass
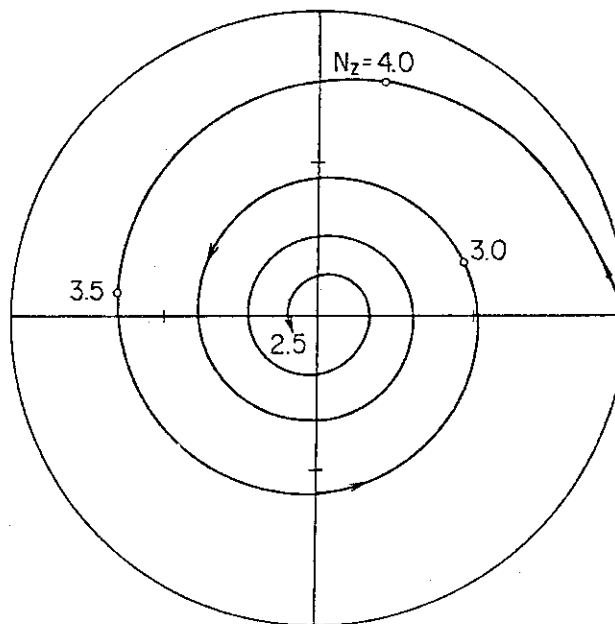number of ions is taken to be 2.4 (equal D-T mixture).

Fig. V-1-16 Ray trajectory of the LHW. Closed circles (●) indicate the

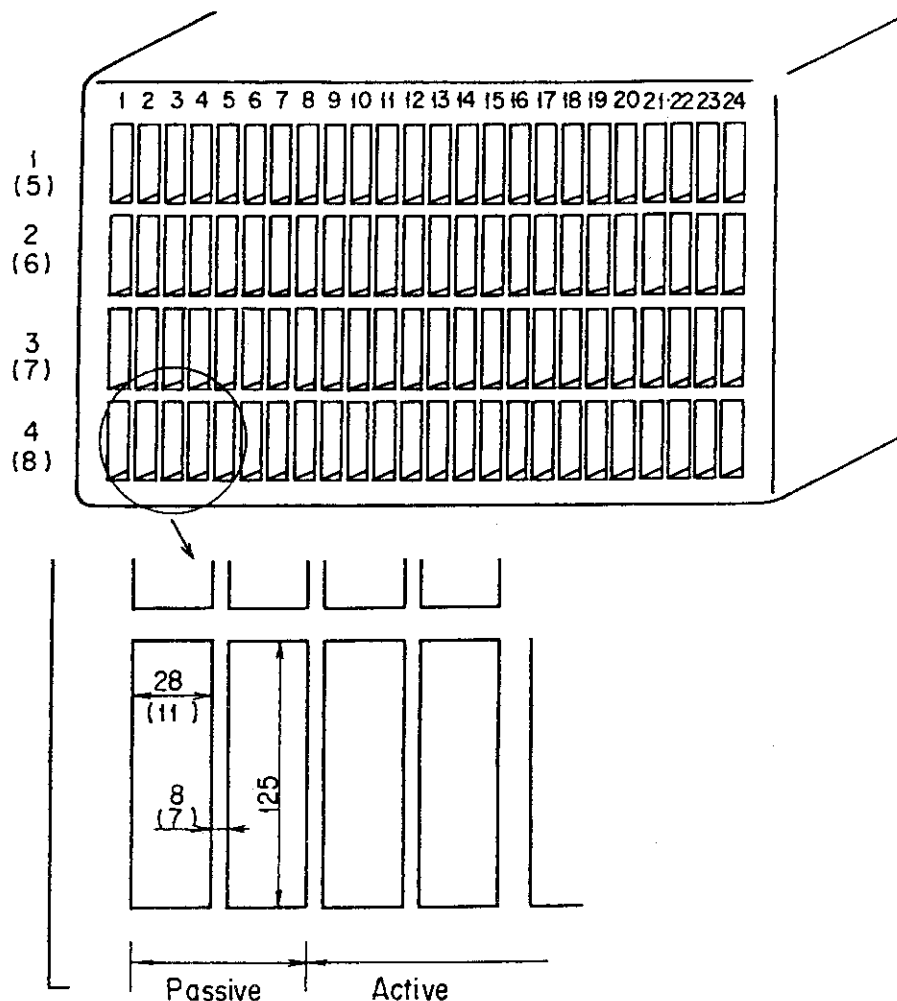points where almost power of each N_z-wave is absorbed.

Fig. V-1-17 Simplified schematics of the launching system for LHRF

heating. b = 28 mm for plasma heating and b = 11 mm for
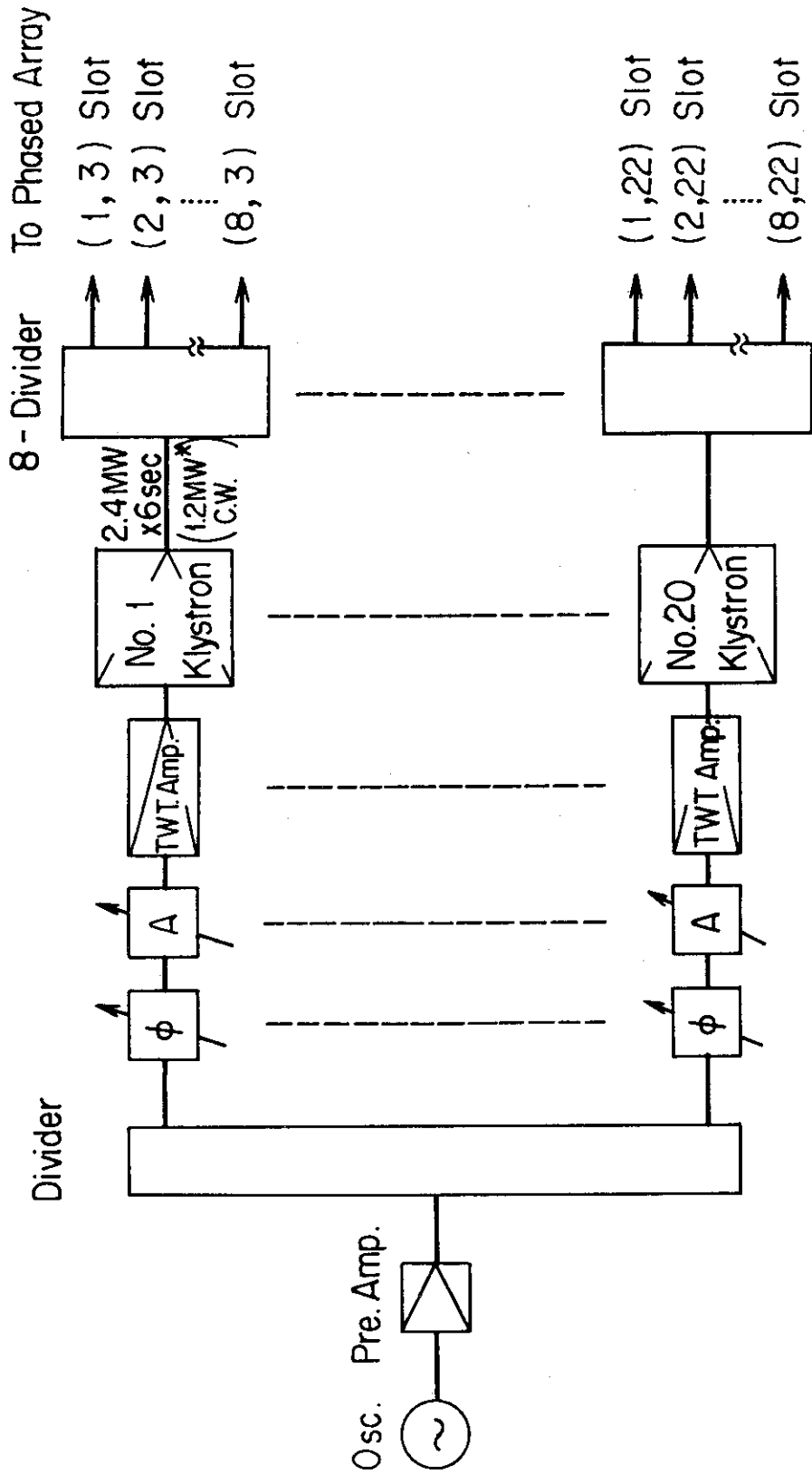
current drive and initial heating.

Fig. V-1-18 An example of the line up of the amplifiers for LHRF heating systme.

1.3 Start-up assist and current drive

—— Electron heating and current drive by the

lower hybrid waves in the INTOR tokamak ——

Tokumi Yamamoto (JAERI)

§1. Introduction

Recently there has been increased interest in heating of tokamak plasmas by RF waves near lower hybrid range of frequencies. The wavelengths are in the range of tens of centimeters so that high power is available and waveguide coupling structures fit conveniently into present experiments and future reactors. For suitable wave parameters, theory predicts that lower hybrid waves can be used to heat ions [1] or electrons [2] selectively or to drive a steady-state plasma current [3,4]. The electron heating via electron Landau damping has been proposed as a useful method of profile control of Ohmic plasma current for getting the high β plasma in a tokamak. The current drive would, in principle, allow steady-state operation of the tokamak reactor, as opposed to the pulsed operation dictated by the usual inductive current drive.

In order to make effective interaction between the lower hybrid waves and electron via Landau process, it is necessary to avoid the deposition of the RF energy into ions resulting from the linear mode conversion and the excitation of parametric instabilities. The JFT-2 experiments on the RF ion heating indicated that for $f_0/f_{LH}(0) \gtrsim 1.6$ the ions did not couple with the RF waves and the parametric decay instabilities almost disappeared [5,6], where f_0 is the applied RF frequency and $f_{LH}(0)$ is the lower hybrid frequency at the center of the plasma column.

Here, the application of the electron heating and current drive by the lower hybrid waves to the INTOR tokamak with major and minor radii of $R_0 = 5.2$ m and $a = 1.2$ m, respectively, and toroidal magnetic field of $B_t = 5.5$ T is described. In particular, we investigate numerically the spatial profiles of RF power deposition for a build-up phase of Ohmic current and generated current for a steady-state operation phase by using a Fokker-Planck equation coupled to an energy loss term and a quasi-linear diffusion term.

§2. Calculation model

The RF interaction with electrons in tokamaks depends on a substantial amount of the RF power density and application of a large amplitude lower hybrid waves can strongly modify the electron velocity distribution function in the region of resonant electrons. However, binary collisions and/or losses of the resonant electrons tend to restore thermal equilibrium, thus establishing stationary distribution function and wave absorption. The evolution of the distribution function in a tokamak is described by a coupled quasi-linear Fokker-Planck equation with the loss term resulting from magnetic fluctuations [7,8]. Solving the Fokker-Planck equation and wave damping in the WKB approximation at a local position under the steay state condition, we calculated the RF power density absorbed by the resonant electrons $P_{ab}(r)$ and the generated current density $J(r)$ with r being the distance from the minor axis in cylindrical co-ordinates. It is assumed for simplicity that the parallel refractive index n_z-spectrum of the RF power flux at a boundary of the plasma column is approximated by

$$P_{rf}(a, n_z) = \frac{P_{rf}(a)}{\sqrt{2\pi}\ \Delta n_z}\ \exp\left\{\frac{-(n_z - n_{z0})^2}{2\Delta n_z{}^2}\right\} \tag{1}$$

with $P_{rf}(a)$ being the net RF power radiated from the launcher and the value of n_{z0} is a constant for propagation. The n_z of the slow wave must satisfy certain accessibility conditions ($n_z > n_{LC}$ with n_{LC} being critical value), otherwise, it will be converted to the outward propagating fast wave [9].

We also use a cylindrical model of tokamak density and temperature profiles given by

$$n_e(r) = n_{e0}\{1-(r/a)^2\}^{\alpha_n} \quad \text{and} \quad Te(r) = T_{e0}\{1-(r/a)^2\}^{\alpha_T}$$

respectively and spatial variation of toroidal magnetic field $B_t(r)$ = $B_{t0}\ R_0/(R_0 + r)$.

The total power absorbed and current generated in the torus are

$$P_{ab} = \int_0^a P_{ab}(r)4\pi^2\ R_0 r\,der \quad \text{and} \quad I_{rf} = \int_0^a j(r)2\pi r\,dr, \quad \text{respectively}$$

The total power balance on the RF power is represented as

$$P_{re}(a) = P_{ab} + P_f + P_t$$

where P_f is the RF power converted into the fast waves and P_t is the slow wave power undamped in the plasma.

It should be noted that power absorbed by the resonant electrons goes into increasing the thermal energy $P_d(r, n_z)$ and enhancing the diffusion losses by the magnetic fluctuations. The ratio of two powers is given approximately by their respective time scales or [7],

$$\frac{P_{ab}(r, n_z) - P_d(r, n_z)}{P_d(r, n_z)} = \frac{(v/\tau_E{}^*\ v_{Te})}{\nu_0(v/v_{Te})^3}$$

where v and v_{Te} and the velocities of resonant and thermal electrons, respectively. ν_0 is the collision frequency and τ_E^* is the energy confinement time. This effect reduces the effeciency of the bulk electron heating if the confinement of electron energy is poor comparing with the collision time.

§3. Results and conclusions

To apply the lower hybrid wave heating for a wide range fo plasma parameters, it is appropriate to employ klystron amplifers with two bands of frequencies of f_0 = 1.5 and 2.0 GH_z. In the former case, the electron heating for the mean electron density of $\bar{n}_e$ = $2 - 4 \times 10^{19}$ m^{-3} is effective and then a profile control of the electron temperature can be expected, while the latter is for the current drive in burning phase. A phased array of multi-waveguides is employed as a launching structure and the different phase between waveguides is adjustable to control the n_z - spectrum during a discharge.

For the computer calculations of the power deposition for the initial plasma heating, the following RF system and plasma parameters are adopted: f_0 = 1.5 GH_z, n_{z0} = 5.0, Δn_z = 1.0 and P_{rf}(a) = 10 MW and n_{e0} = 5×10^{19} m^{-3} of D^+ plasma, α_n = 1.5 and α_T = 1.5. Figure V-1-19 shows the radial profile of the power deposition on bulk electrons as a parameter of central electron temperature. The outward shift in the power deposition is seen with increasing temperature. The total deposited powers for various temperatures of T_{e0} = 0.5, 0.8, 1.0 and 1.5 keV are 2.6, 8.8, 9.4 and 10 MW, respectively. For T_{e0} = 0.8 keV, the almost RF power is consumed to heat the bulk electrons near the plasma center. In figure V-1-20, the results for same

conditions as in Fig. V-1-19 except $T_{e_0} = 1.5$ keV are shown as a parameter of n_{z_0}. It is found that the heating region is comaratively narrow and its radial position can be controlled by changing n_{z_0}. These are favorable for the profile control of the plasma current.

For the calculations of the current drive in a steady-state operation phase, the following parameters are considered; $f_0 = 2.0$ GH$_z$, $n_{z_0} = 1.5$, $\Delta n_z = 0.2$, $P_{rf}(a) = 22$ MW, $T_{e_0} = 30$ keV, $\alpha_T = 0.5$, $n_{e_0} = 1.0$ and 1.5×10^{20} m^{-3} of D$^+$ plasma and $\alpha_n = 2.0$. The profiles of the generated current for different densities are shown in Figv V-1-21. The calculations for $n_{e_0} = 1.0$ and 1.5×10^{20} m^{-3} indicate surface currents and give the total currents of 3.7 and 5.4 MA and the rf powers converted into the fast waves of $P_f = 1$ and 3 MW, respectively. Although decreasing n_{z_0} results in the inward shift in the generated current, n_z can not be less than n_{LC} for the accessibility conditions. Therefore, the stronger toroidal magnetic filed, which lessens the value of n_{LC}, is required for driving the current near the plasma core.

The propagation of the LH wave in a tokamak plasma is described in a geometric optics limit by means of ray tracing technique. With the help of the local dispersion relation for the LH resonance range of frequencies, the three dimensional ray equations for the tokamak geometry are solved, a given density and temperature profiles, the 1/R variation in the toroidal magnetic field, and the resulting poloidal magnetic field due to a rotational transform being incorporated. The ray trajectory picture shows the modification of the n_z spectrum along the trajectories which results in a considerable change in the power transport under the some conditions.

Figure V-1-22 (a) and (b) show a poloidal projection of a pencil of the ray departing from the grill mouth and behavior of n_z along

trajectory, respectively, for the same conditions as in Fig. V-1-19.

It is seen that the slow wave propagates near the center of plasma and

the n_z is nearly constant along radius. The variation of n_z along the

trajectory depends on the dnesity and plasma current plofiles strongly.

In conclusions, the RF system with $f_0 = 1.5$ GH$_z$, $n_{z_0} \lesssim 6$ and $P_{rf}(a)$

=10 MW is useful for the electron heating and the control of the current

in the initial phase of the discharge. However, a fine control of the

frequency and the different phase between the waveguides responding to

the evolutions of the plasma density and temperature may be required

to get a stable burning plasma successfully. On the other hand, more

detailed investigations about the current drive by the lower hybrid

waves may be demanded also.

References

[1] STIX, T.H., Phys. Rev. Lett. 15 (1965) 878.

[2] BERS, A., in Plasma Heating (Proc. 3rd Varenna Symp.) Ed. Compo-
     sitori, Bologna (1976) 99.

[3] FISCH, N.J., Phys. Rev. Lett. 41 (1978) 873.

[4] YAMAMOTO, T., et al., Phys. Rev. Lett. 45 (1980) 716.

[5] IMAI, T., et al., Phys. Rev. Lett. 43 (1979) 586.

[6] YAMAMOTO, T., et al., J. Phys. Soc. Jpn. 48 (1979) 1349.

[7] CHAN, V.S., et al., Nucl Fusion 20 (1980) 1165.

[8] HARVEY, R.W., et al., Nucl. Fusion 21 (1981) 153.
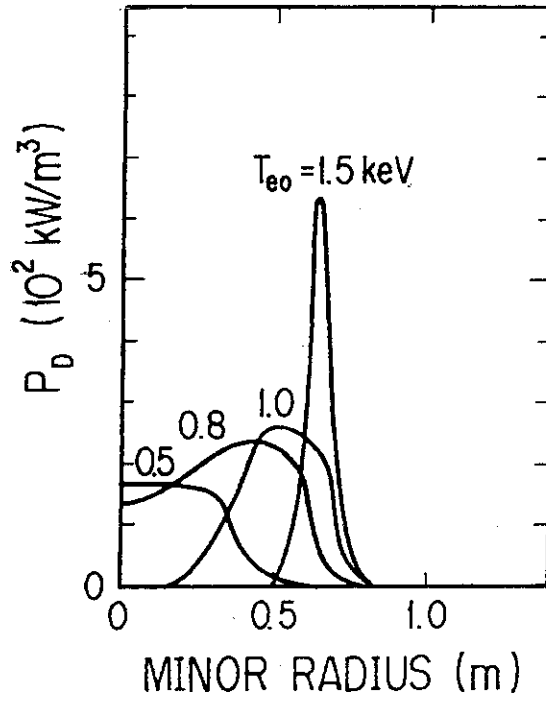
[9] GLAGOLEV, V.M., Plasma Phys. 14 (1972) 301.

Fig. V-1-19 Radial profiles of the power deposition as a parameter of central electron temperature ($f_0 = 1.5$ GH$_z$, $n_{z_0} = 5.0$, $\Delta n_z = 1.0$, $P_{rf}(0) = 10$ MW, $n_{e_0} = 5 \times 10^{19}$ m^{-3}, $\alpha_n = 1.5$, $\alpha_T = 1.5$]
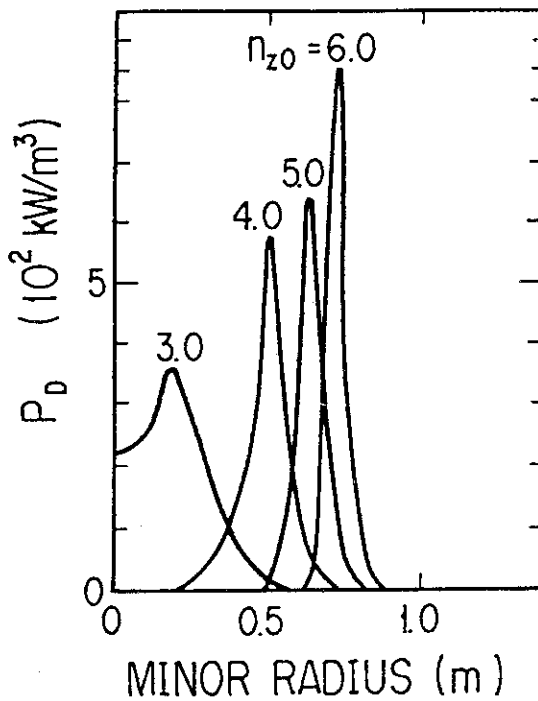

Fig. V-1-20 Radial profiles of the power deposition as a parameter of n_{z_0} under same conditions as in Fig. V-1-19 except $T_{e_0} = 1.5$ keV.
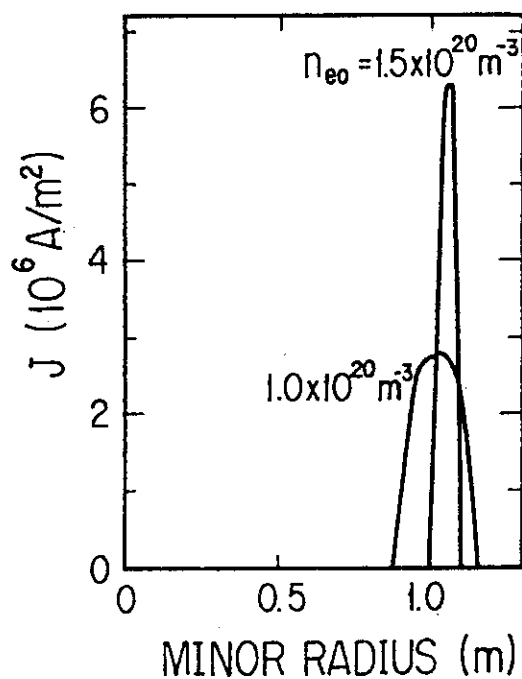
Fiv. V-1-21 Radial profiles of the generated current for n_{e_0} = 1.0 and 1.5 × 10^{20} m^{-3}. [f_0 = 2.0 GHz, n_{z_0} = 1.5, Δn_z = 0.2, P_{rf}(a) = 22 MW, T_{e_0} = 30 keV, α_T = 0.5, α_n = 2.0]
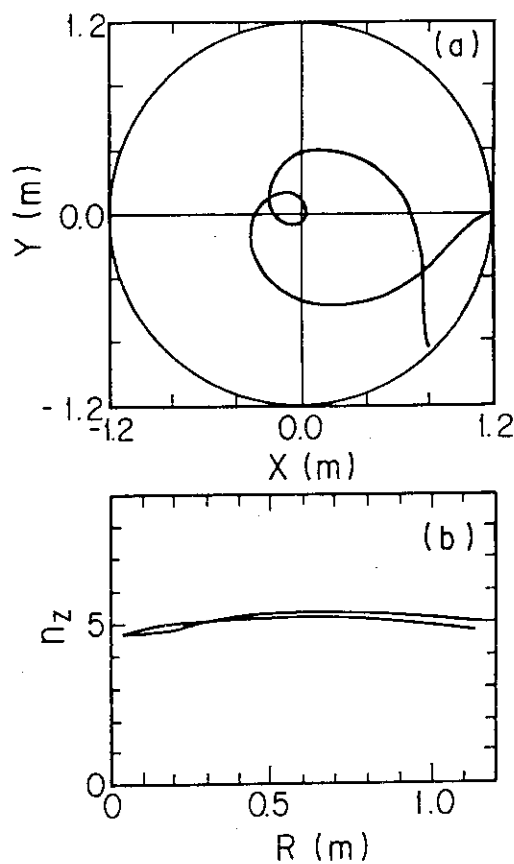
Fig. V-1-22 (a) Poloidal projection of the LH wave ray trajectory and

(b) behavior of the n_z along radius for the same conditions

as in Fig. V-1-19

2. System Design Concepts

2.1 Ion Cyclotron Wave Launching System

H. Kimura*

T. Ohno**

N. Kobayashi**

T. Uchida**

J. Ohmori**

Y. Sawada**

K. Ebisawa**

K. Uchida**

M. Yamauchi**

*   Japan Atomic Energy Research Institute

** Toshiba Corporation

2.1.1 Introduction

RF plasma heating experiments have shown the attractive results for the last several years, and hence the possibility of the ignition with a RF heating has been discussed. In INTOR design study, ICRF heating is used for the secondary plasma heating. This work describes the primary result of it.

In this design, all metal antenna type launching system is adopted and it is investigated to construct the ICRF heating system, especially the RF launching system, which has the sufficient capability for the reactor component, with some experiences in real machines, such as JFT-2, TFR, PLT.

2.1.2 Specifications

(1) RF parameter

Frequency	85 MHz
Input power/port	15 MW
Port Number	4
Total input power	50 (+10) MW
Pulse width	10 sec.
Repetition rate	10 sec/246 sec.

(The number in the parentheses denotes redundancy.)

(2) Antenna parameter

Distance from central conductor to plasma surface	9.2 cm
Distance from central conductor to return conductor	30 cm
Central conductor length	1 m
Central conductor width	40 cm
Antenna impedance	
Resistance	9.3 Ω/m
Reactance	95.6 Ω/m

, where the central plasma density (n_{eo})
is $2.1 \times 10^{14} cm^{-3}$.

2.1.3 Outline of ICRF Heating System

Foundamental ICRF heating system is composed of the antenna,

the coaxial cable and the double stub tuner as shown in

Fig. V-2-1. The standard ICRF antenna consists of three

elements, which are the central conductor, the return con-

ductor and the Faraday shield. These three elements have the

cooling channel for removing some heat load. Their relative

positions from the plasma surface are shown in Fig. V-2-2.

The Faraday shield should be located as same as the first

wall position. For the impedance matching between the RF

power amplifier and the antenna, the double stub tuner is

used. The each stud length except the stroke length for

the stub driving is about 1.7 m. The interval between the

two stubs is 0.5 m. In this design, the characteristic

impedance of the coaxial cable is 50Ω between the RF power

amplifier and the double stub tuner and is 25Ω between the

double stub tuner and the antenna. The coaxial cable is
filled with SF_6 gas to raise the withstand voltage. The
vacuum is sealed at the ceramic feed-through.

2.1.4 Electrical Design

For the antenna impedance of RD = 9.3Ω/m and XD = 95.6Ω/m,
where RD and XD is the resistive part and the reactive
part of the antenna impedance, respectively, the voltage
and the current standing waves are calculated for the
input power of 15 MW and the maximum volage is discussed.

The voltage V and the current I distributions along the
antenna and the coaxial cable for some cases are shown in
Fig. V-2-3 ∿ Fig. V-2-6, when the load impedance is matched
by the double stub tuner.
In Fig. 1, V,I for the coaxial cable characteristic impe-
dance Z_c of 50Ω and in Fig. V-2-2 V,I for Z_0 = 25Ω are shown,
without any additional capacitance except for the capacitance
between the central conductor and the return conductor,
where V,I are the amplitude described in the instantaneous
value, that is, $V = \sqrt{2}|Vrms|$ and $I = \sqrt{2}|Irms|$.
The maximum voltage is about 130 kVp in both cases. Even
if the antenna is divided into 2 or 4 sections, the maximum
voltage is 93 kVp or 66 kVp. According to the experimental
results in some tokamaks, it is desirable that the maximum
voltage is less than 30 ∿ 40 kVp at the antenna and the
feed-through.

To reduce the voltage, the capacitance between the Faraday shield and the central conductor is added and decreases the characteristic impedance of the antenna. If the gap spacing between the Faraday shield surface and the central conductor surface is 1.5 cm, the capacitance CF at the gap is about 2.4×10^{-10} F/m and the characteristic impedance of the antenna is 25Ω. The voltage and the current distributions with CF = 2.4×10^{-10} F/m are shown in Fig. V-2-5 for $Z_0 = 50\Omega$ and in Fig. V-2-6 for $Z_0 = 25\Omega$.
Assuming that the RF power of 15 MW is radiated by 4 antennae in one RF port halves the maximum voltage as shown in Figs. V-2-5 and V-2-6, and then the maximum voltage is about 55 kVp for $Z_0 = 50\Omega$ and about 30 kVp for $Z_0 = 25\Omega$. For the latter case, the voltage breakdown will be safely suppressed in the coaxial cable filled with SF_6 gas of about 2 atom and also in the vacuum region.
According to the above discussion, it is reasonable to choose the coaxial cable characteristic impedance $Z_0 = 25\Omega$. in the region between the double stub and the antenna and $Z_0 = 50\Omega$ in the region between the RF power amplifier and the double stub to reduce the transport power loss.

2.1.5 Heat Load

The heat load of the three elements of one antenna and the Cu coated SS coaxial cable are estimated and tabulated in Table V-2-1.

(1) Heat in central and return conductors

The central conductor and the return conductor are made of Cu coated SS plate. The Cu coating thickness is about 50μm. The length of each conductor is about 1 m and the nuclear heat is about 70 kW for each conductor. For the estimation of RF power loss, the current distribution shown in Fig. V-2-6 is used. For the estimation of the nuclear heat, the space factor of each conductor is assumed to be 50% because the cooling channels are required inside the conductors. The nuclear heat is dominant in the two conductors.

(2) Heat in Faraday shield

As the Faraday shield must receive the radiation load of about 23 W/cm^2 from the plasma, the heat load including the nuclear heat is similar to the first wall. Therefore the total plasma radiation heat is about 200 kW and the total nuclear heat is about 200 kW. The Faraday shield is composed of many pipes so that the cooling medium can pass through them. In this estimation, it is assumed that the pipe cross section is 4 cm × 2 cm, the cooling channel occupys about 10%

of it, and the total surface area of the Faraday shield

is 0.8 m^2.

(3) Heat in coaxial cable

As the spacially averaged RF current along the coaxial

cable is about 530 Arms, the RF power loss is 2.2 kW/m

and the total RF power loss is 50 kW, where the dia-

meter of the inner conductor is 20 cm, the diameter

of the outer conductor is 30 cm, the thickness of each

cylinder is 3 mm. The total power loss is the loss

for the distance of 25 m from the stubs to the antenna.

The Cu coating thickness is about 50μm, which is suffici-

ently larger than the skin depth for 85 MHz. The esti-

mation of the nuclear heat is over estimated value

because it is supposed that there is the same nuclear

heat along the total length of the coaxial cable. So

the actual nuclear heat of the coaxial cable is less

than the value in the Table V-2-1. The RF power loss is

dominant for the coaxial cable.

2.1.6 Electromagnetic force

(1) Central conductor

(i) The repulsive force between the RF current flowing

the central conductor and the return conductor is

0.1 kg/m at the maximum for the maximum current

about 1.3 kAp in one antenna.

(ii) The radial force f_1 directs to plasma as shown
in Fig. 7 arises on the central conductor because
of the induced current i_1 at the plasma disruption.
The current i_1 is induced by the change of the
toroidal magnetic field B_T due to the plasma
diamagnetism. The current i_1 is dependent on the
resistivity of the base material of the coaxial
cable. The estimated maximum f_1 for three cases
are shown as follows;

all Cu coaxial cable   : 5.8×10^3 kg/m^2

Cu coated Aℓ coaxial   : 4.3×10^3 kg/m^2
cable

Cu coated SS coaxial   : 2.5×10^3 kg/m^2
cable

, where the time constant of the plasma current
decay at the major disruption is 20 ms, the
toroidal magnetic field change of 0.3T is assumed
and the antenna resistance due to the conduction
is ignored in comparison with the total coaxial
cable resistance.
The force f_1 can be removed by the use of D.C
break to the coaxial cable between the antenna and
the stub.

(iii) The radial force f_2 is generated by the change
of the poloidal magnetic field B_p at the plasma
disruption as shown in Fig. V-2-7. When the central
conductor is constructed by Cu coated SS plate,

f_2 depends on the thcikness of the SS plate.

f_2 at the maximum for some thickness of the SS plate are as follows;

Thickness of 3 mm : 4.5×10^2 kg/m²

5 mm : 7.5×10^2 kg/m²

7 mm : 10^3 kg/m²

, where the central conductor thickness is 3 cm. The current i_3 is induced by the normal component of B_p to the central conductor. This field is about 0.2T. With i_3 and B_T, the electromagnetic force f_3 as shown in Fig. V-2-7 arises. For the conductor thickness of 30 mm, f_3 gives rise to the torsion through the bening moment of 925 kg·m. According to these results the central conductor and also the return conductor require appropriate rib structure.

(iv)   On the end conductor of the antenna the vertical force f_4 which has the opposite direction as shown in Fig. V-2-8 arises from The B_T and the induced current i_4 results from the B_p change at the plasma disruption. When the end conductor surface area is 0.4 m × 0.3 m, the force f_4 at the maximum is about 30 ton/m² on the one side. This large force can be reduced to a negligible small value by dividing the end conductor into the width less than the skin depth for SS.

(2) Faraday shield

The large current i_5 is induced at the plasma dis-
ruption as shown in Fig. V-2-9 by the change of B_p. As
the Faraday shield is located near the first wall
position in this design. The electromagnetic forces
f_5 on the front surface and f_6 on the side position
of the Faraday shield are considered. If the Faraday
shield is composed of about 25 pipes, f_5 and f_6 for
the one pipe is about 14 kg/m and 40 kg/m, respectively.

In this estimation it is supposed as follows;
The all pipes are individually insulated and connected
to the header as shown in Fig. V-2-10. As two cooling
pipes extend to the access door, the electrical cir-
cuit is short-circuited at the access door.

2.1.7 Mechanical Consideration

Following the previous discussion about the heat load
and the electromagnetic force $f_2 \sim f_6$ at the plasma dis-
ruption, we estimate the mechanical and thermal stress of
ICRF antenna.

(1) Electromagnetic stress

(i) Stress of the central conductor by f_2 and f_3

As f_2 normal to the front and back conductor
surface is 10^{-3} kg/mm^2 for the unit area, the
tensile stress σ_2 is straightforwardly 10^{-3} kg/mm^2.

When the torsion due to f_3 is supported only by the end conductor, the maximum torsional stress σ_3 is approximated by torsion of a rectangular rod;

$$\sigma_3 = \frac{925 \times 10^3}{0.312 \times 400 \times 30^2} = 8.2 \text{ kg/mm}^2$$

(ii) Stress of the end conductor by f_4

The torsional moment is 1.51×10^4 kg-cm for the loaded area of 30 cm $\times$ 4.2 cm (skin depth at the disruption). As this moment is supported by the bottom wall of the antenna cell, the stress σ_4 is small; for the bottom wall width of 80 cm and the thickness of 2 cm, the stress is

$$\sigma_4 = \frac{1.51 \times 10^4 \times 10}{0.333 \times 800 \times 20^2} = 1.4 \text{ kg/mm}^2$$

(iii) Stress of the Faraday shield by f_5 and f_6

The stress σ_5 results from f_5 can be estimated from the staticaly indeterminate beam model as shown in Fig. V-2-11-(a).
When the BC side is regarded as a simple supported beam suffered the uniform load, the deflection angle θ at B is given by a summation of two deflection angles. The one angle is the deflection at B when the AB side subjected to the bending moment M is supported on the one end and is fixed

on the other end. The other angle is the deflection at B when the BC side is regarded as a cantilever suffers M on the both ends. Then we get the relation

$$\frac{w\ell_2^3}{24EI} = \frac{M\ell_1}{4EI} + \frac{M\ell_2}{2EI} \quad ,$$

where E, I is Young's modulus and the moment of inertia area, respectively. For $w=1.4\times10^{-2}$ kg/mm, $\ell_1=350$ mm and $\ell_2=800$ mm, M is 520 kg-mm. The bending moment at the center of BC side is

$$\frac{1}{8}w\ell_2^2 - M = 600 \text{ kg-mm}$$

Then the maximum bending stress on the end of the rectangular cooling tube with the cross section of 4 cm × 2 cm is given by

$$\sigma_S = \frac{M}{Z} = \frac{600}{2360} = 0.25 \text{ kg/mm}^2$$

The stress due to f_7 as shown in Fig. V-2-11-(b) is estimated from a simple beam model. If the B and C ends are not fixed, the AB and CD sides suffer the bending and torsion, and the BC side suffers the shearing and bending. When the load w is uniformly distributed, the maximum bending stress σ_6 arises at the center of AB and CD is

$$\sigma_7 = \frac{M}{Z} = \frac{\frac{1}{24} \cdot 0.04 \cdot 350^2}{4883} = 4\times10^{-2} \text{ kg/mm}^2$$

(2) Thermal stress

(i) Stress of Faraday shield

When the Faraday shield receives the radiation
from the plasma and suffers the nuclear heat
the steady temperature distirbution in the shield
is given by the equation for parallel plate;

$$\Delta T = - \frac{q_u}{2\lambda} x^2 + \frac{(q_u l + q_r)}{\lambda} x + \frac{q_r + q_u l}{\alpha}$$

where, q_r : surface heat load   23 w/cm^2

q_u : nuclear heat   12 w/cm^3

l : plate thickness   1.5 cm

λ : thermal conductivity   0.18 w/cm°C

α : heat transfer coefficient 0.55 w/cm^2°C

In the right hand side of this equation, the first
and second terms are the temperature difference
from the shield surface to the cooling surface,
and the third term is the temperature difference
between the cooling surface and the water. The
Faraday shield structure is shown in Fig. 12.
When the maximum water temperature is 60°C, the
maximum temperature in the shield is 350°C at
the shield surface and 85°C at the cooling sur-
face.

The thermal stress for the temperature distribution T(z) along the plate thickness is given by the following equation,

$$\sigma = \frac{\alpha E}{1-\nu} \left\{ -T + \frac{1}{2C} \int_{-C}^{C} T dz + \frac{3z}{2C^3} \int_{-C}^{C} Tz dz \right\}$$

where α : 1.62×10^{-5} °C

E : 1.97×10^4 kgf/mm^2

ν : Poisson's ratio

C : half of the plate thickness as shown in the next figure;
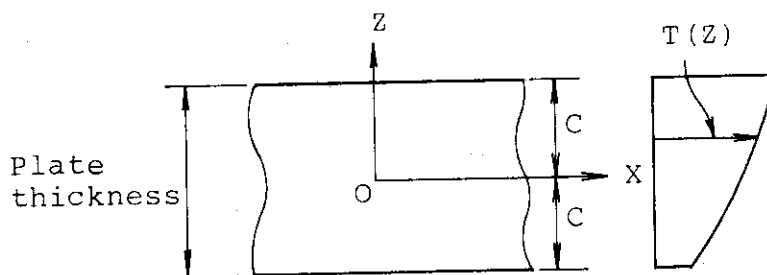
For the case of C=7.5 mm the stress of each position is

$\sigma = 5.7$ kg/mm^2 for the shield surface

$\sigma = -2.8$ kg/mm^2 for the shield center

$\sigma = 5.7$ kg/mm^2 for the cooling surface

(ii) Central conductor

The thermal load of the central conductor is mainly the nuclear heat of 10 w/cm^3. According to Fig. V-2-12, the maximum plate thickness to cooling

surface is 1 cm. As similar to the previous discussion, the temperature rise ΔT is given by

$$\Delta T = - \frac{q_u}{2\lambda} x^2 + \frac{q_u l}{\lambda} x + \frac{q_u l}{\alpha}$$

and then the maximum temperature rise in the central conductor is 46°C. In this case, the maximum thermal stress is

$$\sigma = 2.5 \text{ kg/mm}^2$$

at the cooling surface and the position of 1 cm from the cooling surface.

(3) Stress assessment

According to ASME Sec. III, the Sm value is 14.1 kg/mm^2 for SS316. Therefore the all stresses are enough allowable.

2.1.8 Antenna Configuration

Regarding the previous discussion we try to construct the ICRF antenna for INTOR. The schematic view of the ICRF antenna installed in the reactor is shown in Fig. V-2-13. The blind like part is the Faraday shield whose position is nearly the first wall surface. As the one port has four antennae, the Faraday shield are divided into four region. The front view of the four ICRF antennae is shown in Fig. V-2-14. The central conductor, the return conductor, the end conductor and the coaxial cable are disclosed in the

cross sectional view removed the Faraday shield. The return
conductor and the end conductor are fixed in the wall.
The lateral cross sectional view of the ICRF antenna is
show in Fig. V-2-15. The center conductor is very near the
Faraday shield, and the gap spacing of them is 1.5 cm.
The all antenna elements and the coaxial cable have cool-
ing channels.
In Fig. V-2-16 the bird's-eye view of one antenna is shown,
partly omitting the Faraday shield and the side wall. The
vertical entire cross sectional view of the ICRF antenna in
the reactor is shown in Fig. V-2-17. To reduce the neutron
damage of the ceramics, the feed-through is located behind
the shield. As it is required to protect the trouble of
the tritium or other radioactive materials contamination,
the two feed-throughs are used to divide the transmission
line into two region.

Neutron streaming effects through the bending ICRF ducts
have been studied. Albedo Monte Carlo calculation was
carried out with MORSE-I code to find high energy neutron
flux at a deep location in the ducts. A preliminary
investigation shows that the neutron flux decreases by
one order of magnitude at each corner of the narrow duct.
Though the statistics of the calculation are not enough
to draw a solid conclusion, the total neutron flux at the
ceramic feed-through may be the order 10^{10} n/cm$^2\cdot$s, and
the ceramic could withstand the exposure of 10^{18} n/cm^2
during the INTOR lifetime.

It is also expected that the penetration shield thickness around the RF ducts could be reduced gradually along the ducts if the narrow ducts are extended outward. More detailed analysis is in progress.

2.1.9 Power Supply

One of the advantage of ICRF heating is the availability of the high power vacuum tube of the output power of MW class. For the power amplifier of 85 MHz, TH518 or X2170 is presently available. Their output power is more than 1 MW. It is necessary to drive the one antenna of one port with the power of about 3.8 MW. When the RF heating system is operated in the duty of 10 sec/246 sec, the required power of one antenna will be generated by two tubes and the total tube number will be 40 including the redundancy. As it is usually acceptable that the power efficiency of the RF amplifier is 65%, the power transport efficiency is about 90%, and the power factor of the power supply is about 85%, the A.C. power supply for the total RF output power of 60 MW including the redundancy requires the capacity of 120 MVA as shown in Fig. V-2-18.

Fig. V-2-1 ICRF heating system

Element	R.F power loss	Nuclear heat	Plasma radiation
Central conductor	1 kW	70 kW	~0
Return conductor	1 kW	70 kW	~0
Faraday shield	~0	200 kW	200 kW
Cu coated SS coaxial cable	50 kW	(12 kW)	~0
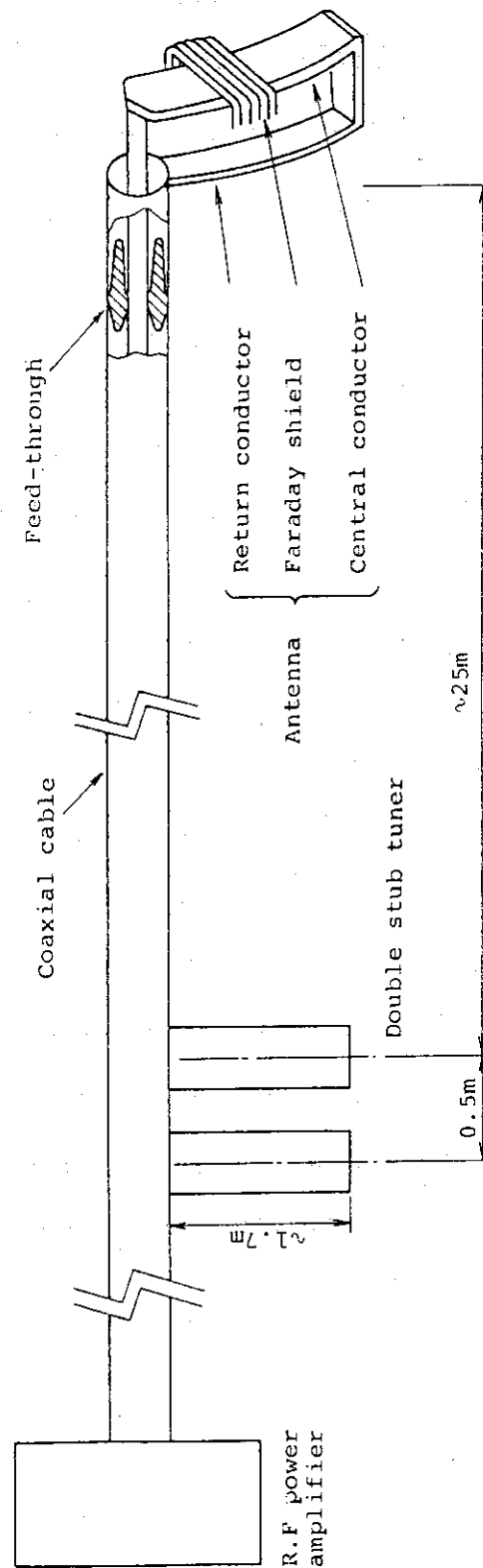
Table V-2-1 Heat load of antenna element
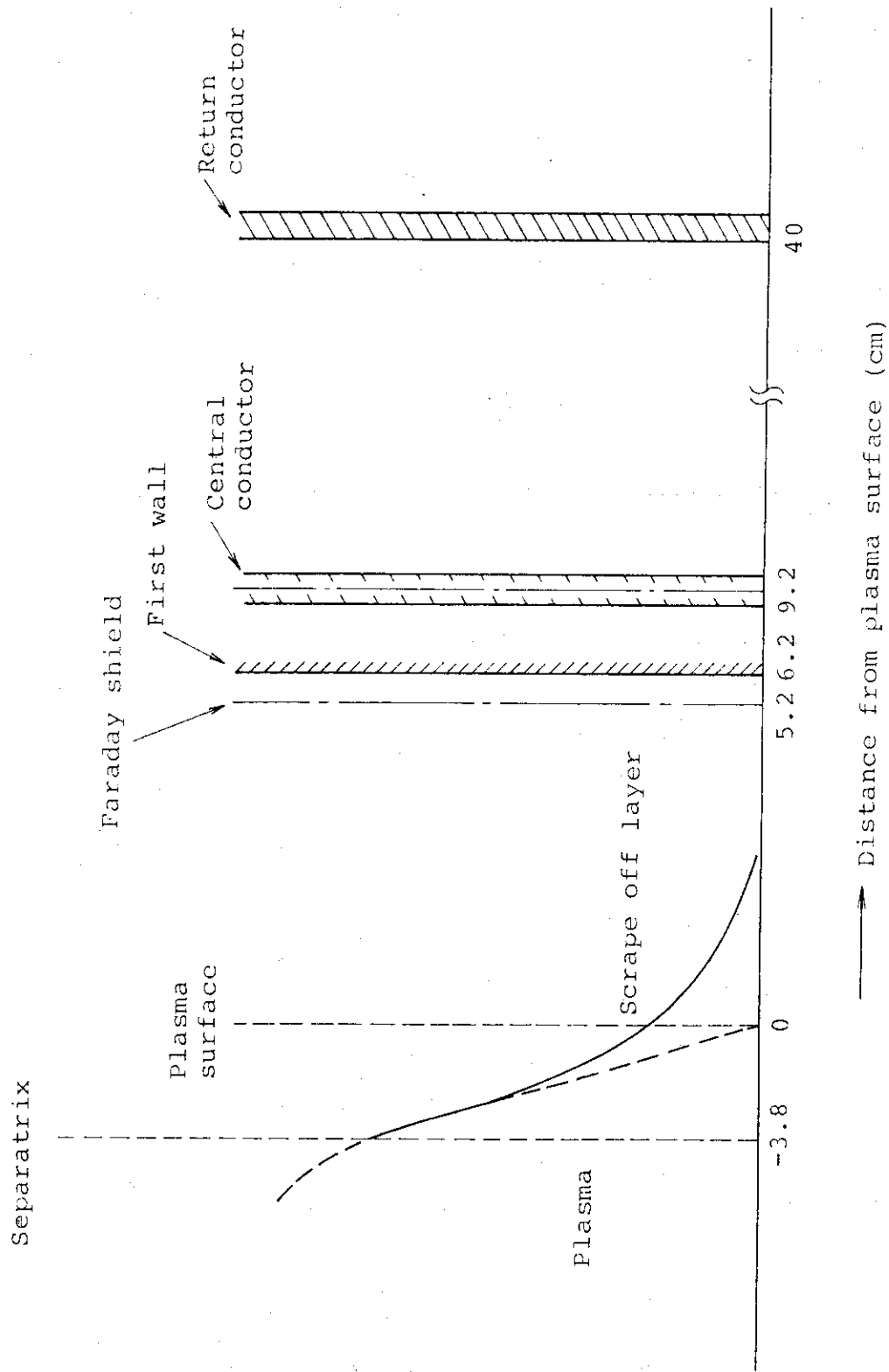
Fig. V-2-2 Relative position of antenna element
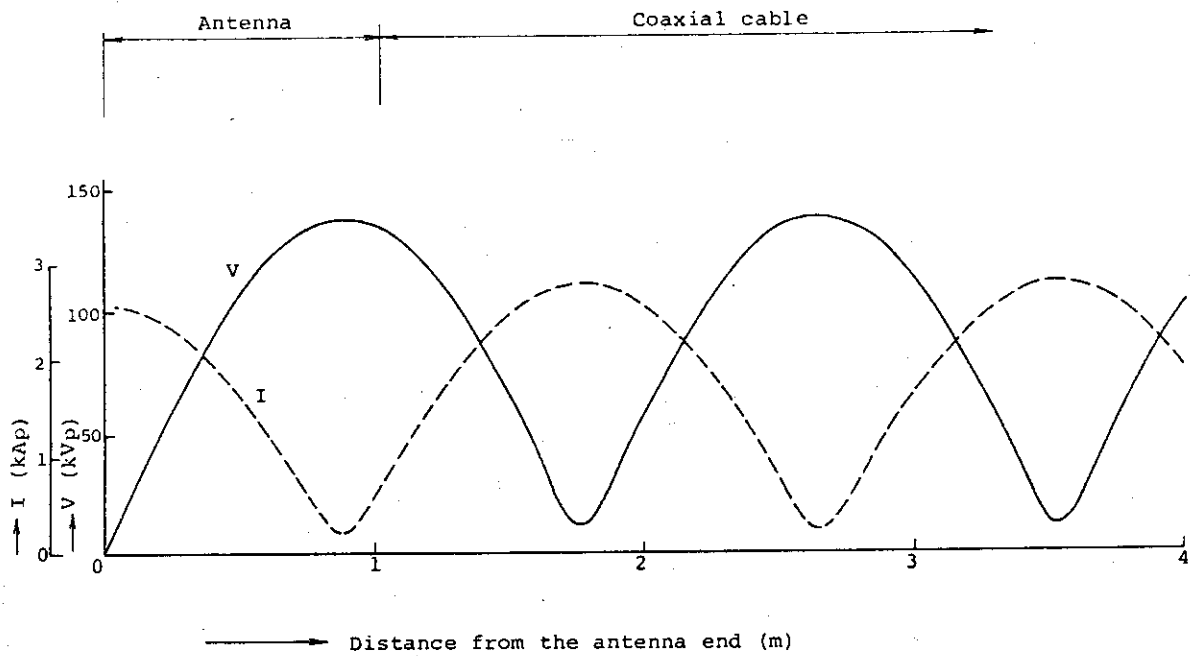
Fig. V-2-3 V, I distributions along the antenna and the coaxial cable
for $Z_0 = 50\Omega$, $CF = 0$ F/m
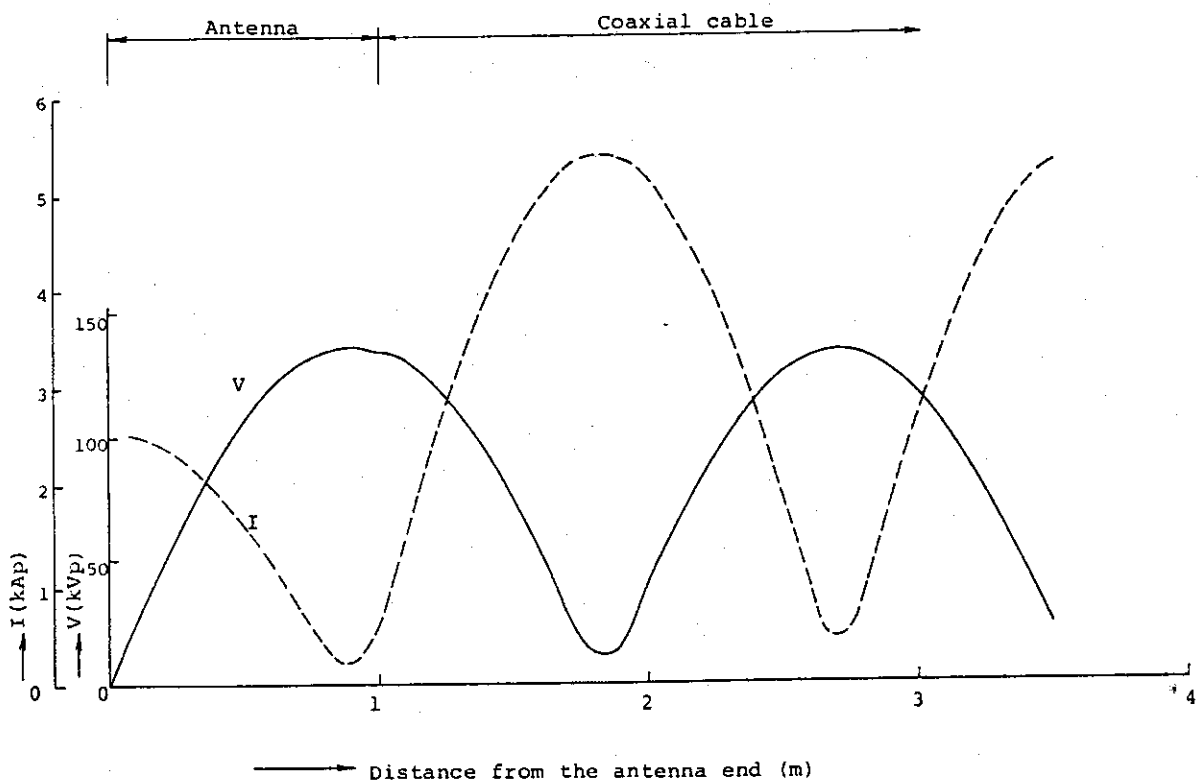
Fig. V-2-4 V, I distribution along the antenna and coaxial cable
for $Z_0 = 25\Omega$, $CF = 0$ F/m
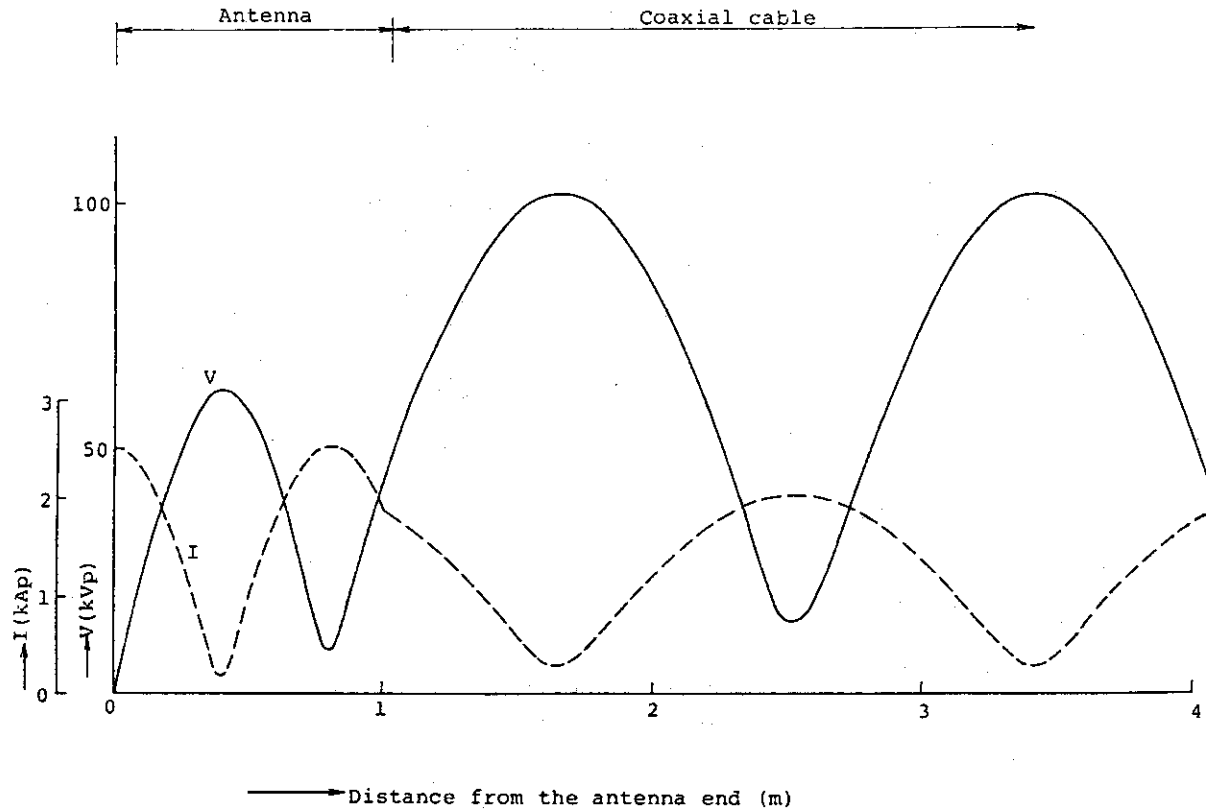
Fig. V-2-5　V, I distribution along the antenna and coaxial cable
for $Z_0 = 50\Omega$, $CF = 2.4 \times 10^{-10}$ F/m
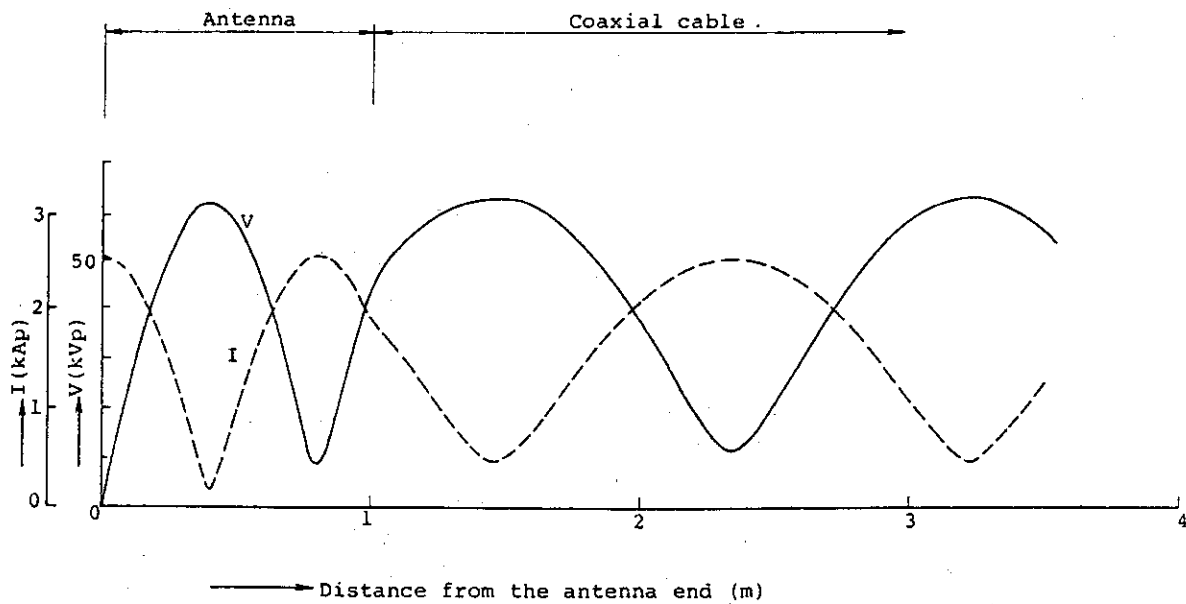
Fig. V-2-6　V, I distribution along the antenna and coaxial cable
for $Z_0 = 25\Omega$, $CF = 2.4 \times 10^{-10}$ F/m
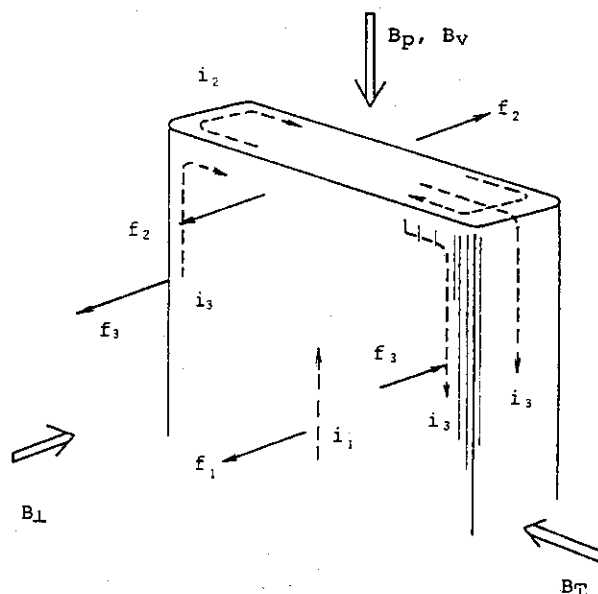
Fig. V-2-7 Electromagnetic force on central
conductor at plasma disruption
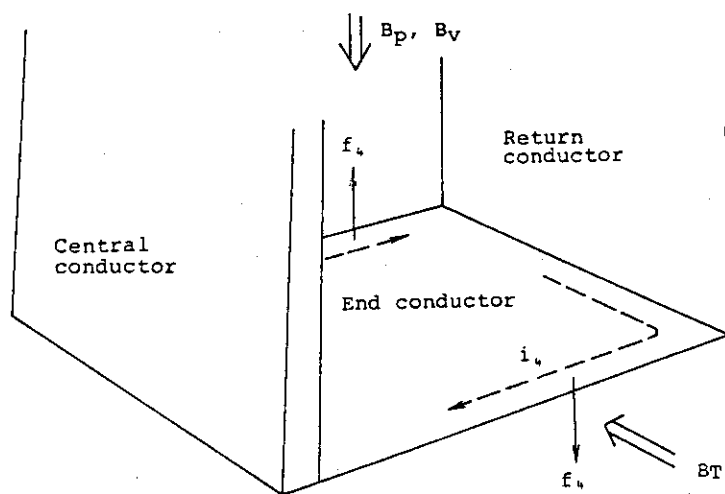
Fig. V-2-8 Electromagnetic force on end conductor
at plasma disruption
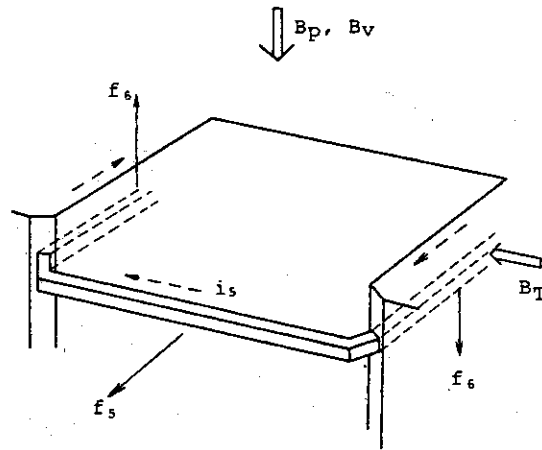
Fig. V-2-9 Electromagnetic force on Faraday shield
at plasma disruption
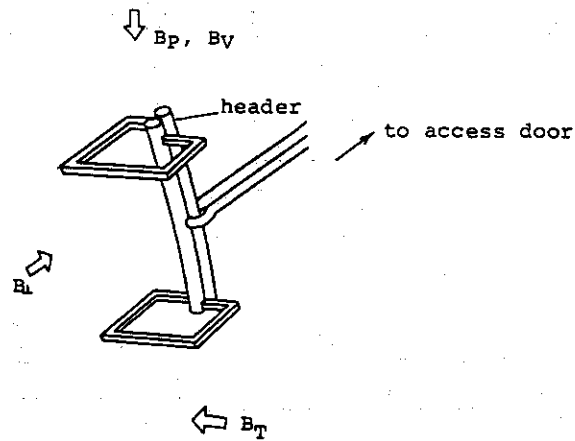
(a)
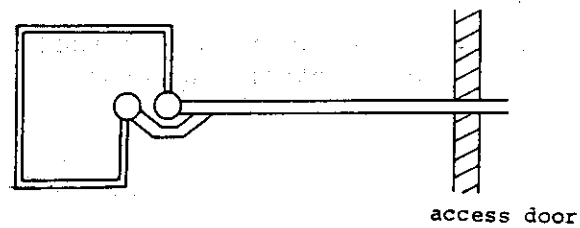
(b)

Fig. V-2-10 Faraday shield short circuit
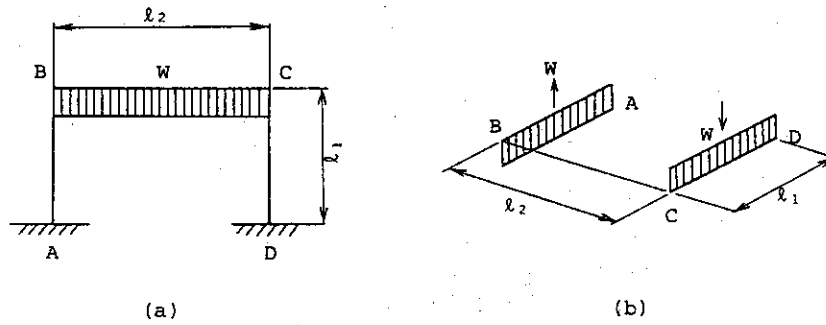
Fig. V-2-11 Stress estimation of Faraday shield
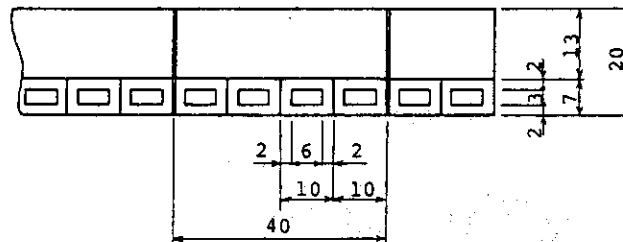
(a) Faraday shield
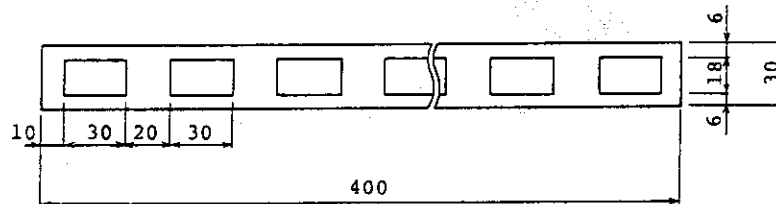
(b) Central conductor

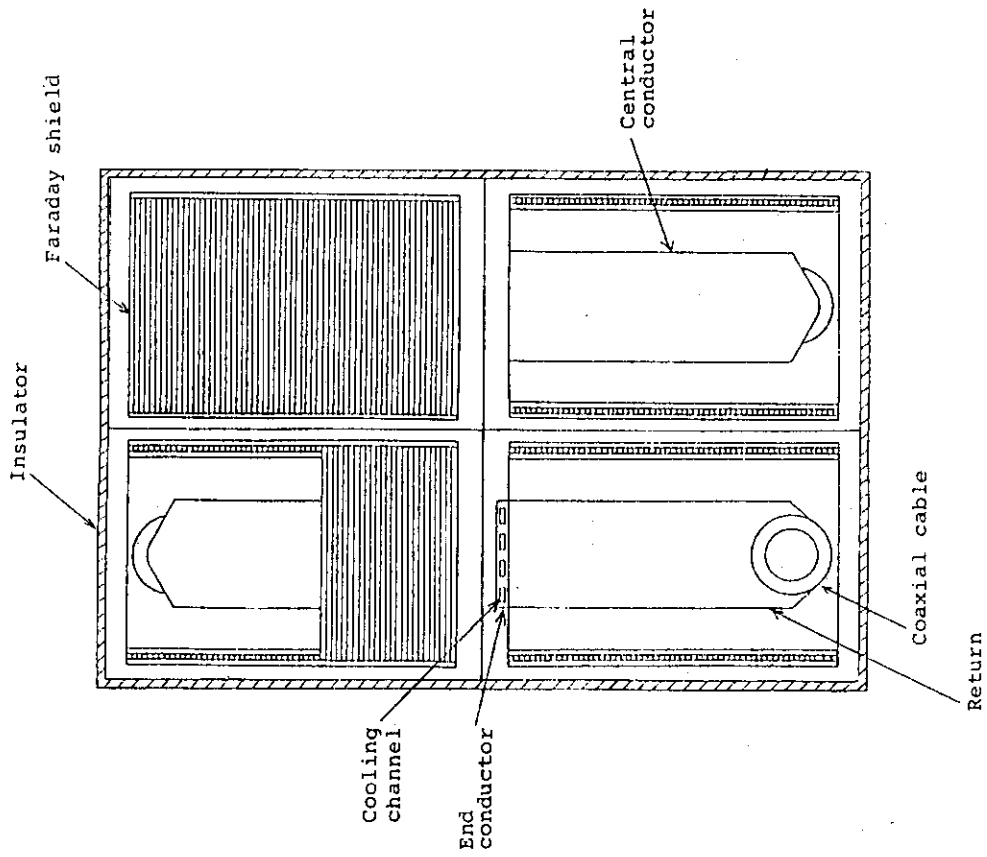Fig. V-2-12 Cross sections of faraday shield
and central conductor
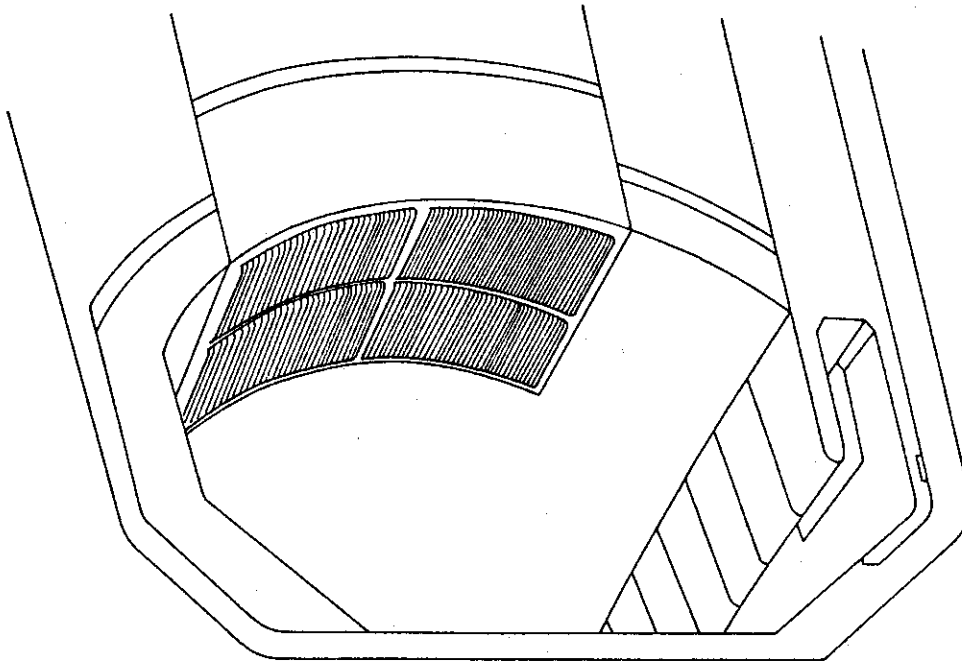
Fig. V-2-14 Front view of four ICRF antenna

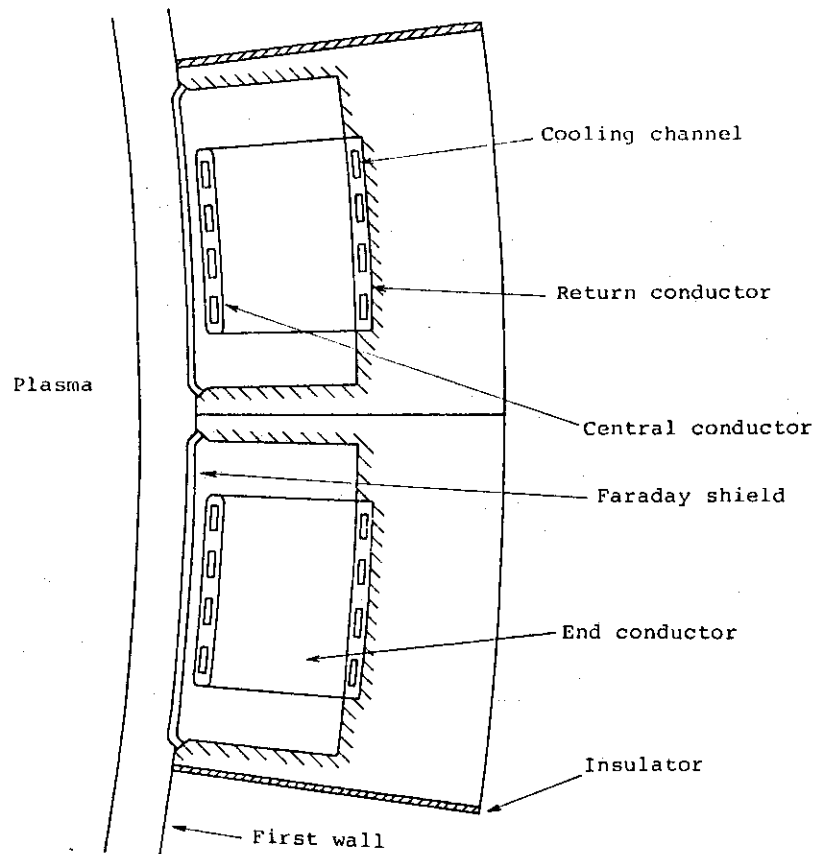Fig. V-2-13 Schematic view of ICRF antenna in reactor

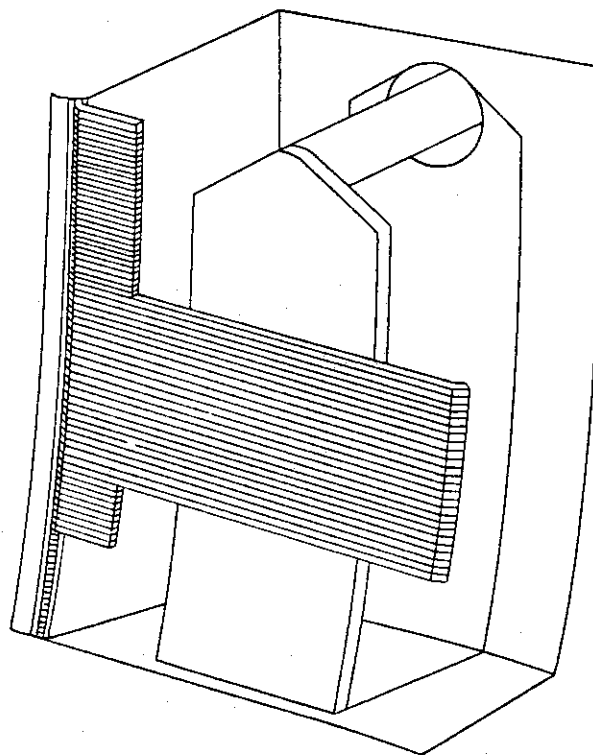Fig. V-2-15 Latoral cross sectional view of ICRF antenna
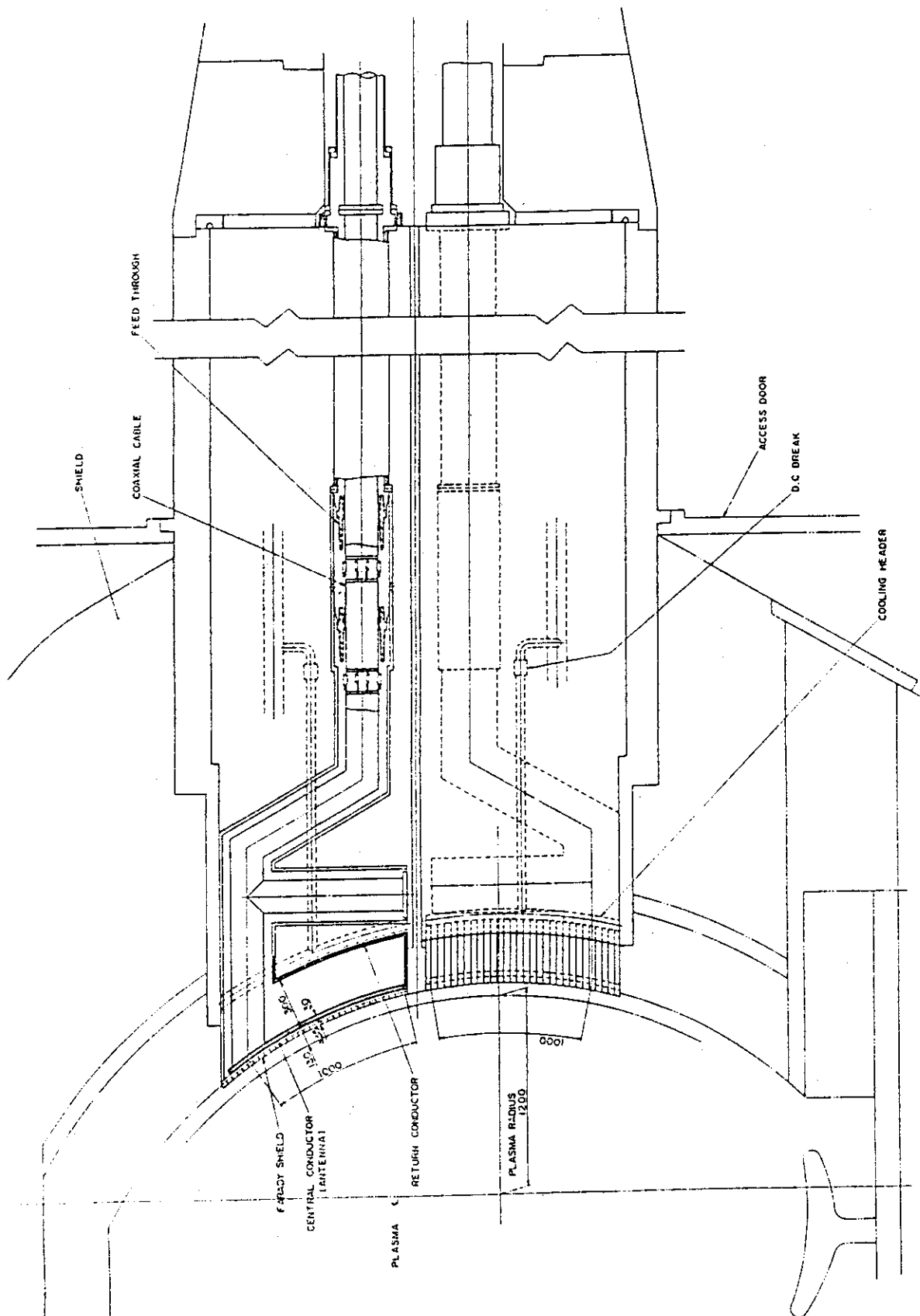

Fig. V-2-16 Bird's-eye view of one antenna

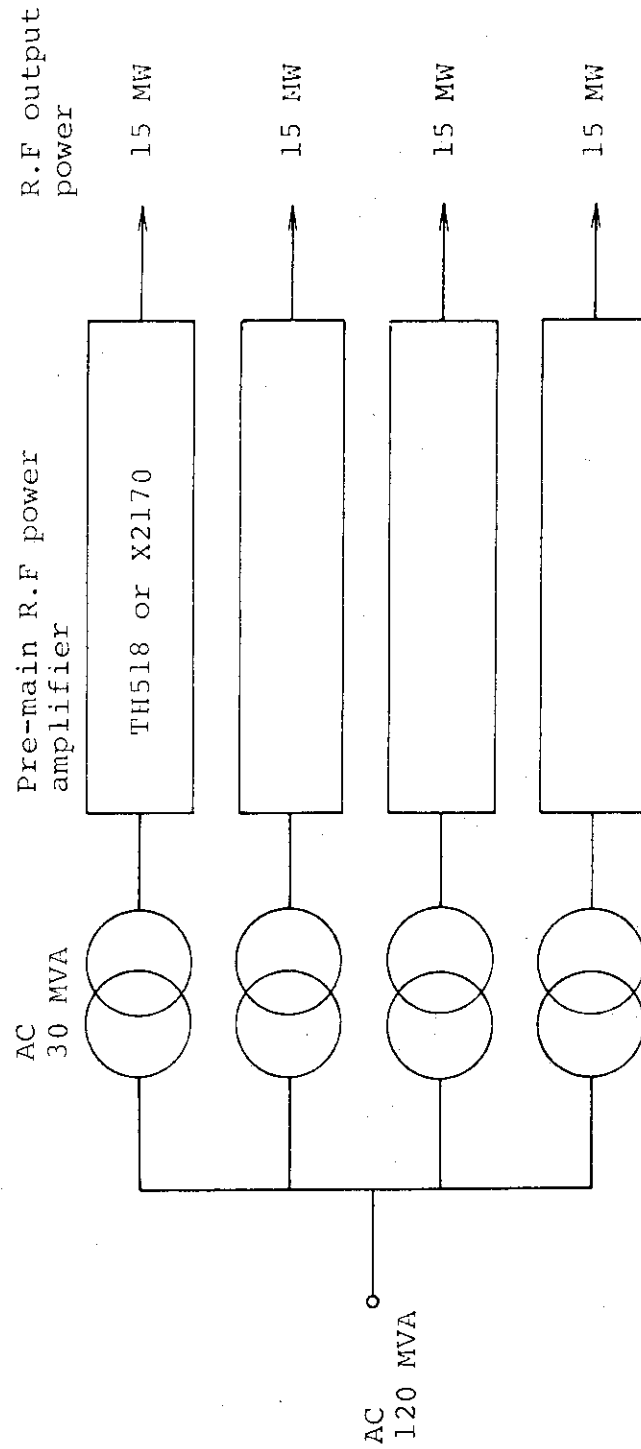Fig. V-2-17 Total cross sectional view of ICRF antenna in reactor

Fig. V-2-18 Schematic diagram of power supply of ICRF heating system

2.2 Lower Hybrid Wave Launching System

T. Imai*

T. Ohno**

N. Kobayashi**

T. Uchida**

Y. Sawada**

K. Ebisawa**

K. Uchida**

M. Yamauchi**

* Japan Atomic Energy Research Institute

** Toshiba Corporation

2.2.1 Specifications

Total input power   85 MW

Plasma heating power   75 MW in duty of 10 sec/246 sec

Current drive power   10 MW in duty of 211 sec/246 sec

Maximum available r.f port number   4

Maximum transport r.f power density   4.5 kw/cm^2

Interval of waveguide center for plasma heating 36 mm

Interval of waveguide center for current drive   18 mm

Long side width of waveguide   125 mm

R.F frequency   2 GHz

Launcher   Grill type

2.2.2 LHRF launcher of plasma heating and current drive

Total injection r.f power is 85 MW. The power of

75 MW is devoted to plasma heating for about 10 sec

and the power of 10 MW for current drive is injected

in C.W operation.

The waveguide size for the plasma heating is 125 mm

× 28 mm as shown in Fig. V-2-19 and the interval of

them is 36 mm. The waveguide size for the current

drive is 125 mm × 11 mm as shown in Fig. V-2-20 and

the interval of them is 18 mm. The thickness of the

waveguide plate is about 3 mm.

The launcher for the plasma heating, which we call

A type from now, is composed of 48 waveguides

(lateraly 24 × vertically 2 as shown in Fig. V-2-19,

where the each two waveguides at the right and left
sides are short circuited at the distance of $\lambda/4$
from the launcher front to improve the radiation
characteristics of the grill). The front size of
the A-type launcher is about 910 mm × 310 mm.
When the number of A-type launcher is 16, the total
number of the waveguide which r.f power passes
through is 640. As the r.f power for one waveguide
is 117 kW, the power density is 3.3 kW/cm^2, which
is smaller than the maximum allowable density
4.5 kW/cm^2.

On the other hand, the launcher for current drive,
which we call B-type, is composed of 56 waveguides
(lateraly 28 × vertically 2 as shown in Fig. V-2-20,
where the each two waveguides of both sides are
passive like as A-type launcher.) The front size
is about 550 mm × 310 mm.

When the B-type launcher number is 4, the total
waveguides number for r.f power transport is 192.
The r.f power of one waveguide is 52 kW and the
power density is 3.8 kW/cm^2 which is smaller than
4.5 kW/cm^2.

For both type launchers, the waveguides are con-
tained in a vessel as shown in Fig. V-2-21. The ves-
sel is a water jacket to cool several heat loads of
launcher as mentioned later. In this discussion,
suppose that the launcher length is 1.7 $\sim$ 2 m and
the thickness of the vessel wall is 2 cm.

Each waveguide is supported by some conducting plates as shown in Fig. V-2-21. Also there are longitudinal supporters omitted in this figure in the vessel.

2.2.3 Mechanical consideration at disruption

(1) Electromagnetic force of launcher

In this discussion, the induced current in the launcher vessel is only considered, because the induced current of each waveguide is almost cancelled by the current, which flows neighbor waveguides with each other.

First we consider the current i_{10} induced by the variation of $B_\perp$ as shown in Fig. V-2-22. $B_\perp$ is the normal field to the launcher front.

$B_\perp$ is about 0.2T on the average. In fact this field is negligible near the intermediate plane of the plasma, so the field variation affects only for upper launchers. The force f_{10} results from $i_{10} \times B_T$ and f_{11} results from $i_{10} \times (B_P + B_V)$, where B_T is the toroidal magnetic field, B_P is the poloidal magnetic field and B_V is the vertical magnetic field. In this estimation, $B_T \sim 4.3T$, $B_P \sim 0.9T$ and $B_V \sim 0.6T$.

The another current i_{12} induced by B_P variation is shown in Fig. V-2-23.

The force f_{12} results from $i_{12} \times B_T$ and f_{13} results from $i_{12} \times (B_P + B_V)$.

(2)   Electromagnetic force and stress

  (i)   A type launcher

The maximum f_{10} and f_{11} are about 2.6×10^4 kg/m and 8.9×10^3 kg/m, respectively, where the launcher length is 1.7 m. These forces give rise to the shering stress at the long side corner of the launcher. The maximum stress is approximately given by

$$\sigma = \frac{F}{S} = \frac{26 \times 310 + 8.9 \times 910}{20 \times 1700} \sim 0.5 \text{ kg/mm}^2$$

The maximum f_{12} and f_{13} are about 1.8×10^4 kg/m and 2×10^4 kg/m^2 for unit area, respectively. On the top and bottom surfaces of the launcher, the bending moment arises from the force f_{12}. The maximum bending stress is given by

$$\sigma = \frac{M}{Z} \sim 3 \times 10^{-3} \text{ kg/mm}^2$$

where $Z \sim 5.4 \times 10^6$ mm^3 for a box model. The another stress is tensile due to f_{13} on the side wall of the launcher and is straightforwardly 2×10^{-2} kg/mm^2.

  (ii)   B type launcher

The all forces and stresses can be discussed like as the previous estimations. The maximum f_{10} and f_{11} are about 1.4×10^4 kg/m and 4.9×10^3 kg/m, respectively. Then the shering stress due to these forces is

$$\sigma \sim 0.2 \text{ kg/mm}^2$$

The maximum f_{12} and f_{13} are about 3.7×10^4 kg/m and 4×10^4 kg/mm^2, respectively. So the bending stress due to f_{12} is

$$\sigma \sim 1 \times 10^{-2} \text{ kg/mm}^2$$

The tensile stress due to f_{13} is about 4×10^{-2} kg/mm^2.

The above estimations are summarized in Table V-2-2.

(3) Assessment of stress

According to ASME Sec. III, as Sm is 14.1 kg/mm^2 for SS316, all stresses are enough allowable. The launcher can endure to the plasma disruption.

2.2.4 Heat load of launcher

There are some heat loads of the launcher. The launcher suffers the nuclear heat in everywhere and receives the plasma radiation load on the front surface and the waveguide inner surface. Although there is the r.f loss in the waveguide, it is much smaller than the other loads.

(1) Heat load of waveguide

The inner cross sectional size of the waveguide is 125 mm × 28 mm for the plasma heating and 125 mm × 11 mm for the current drive. The plate thickness of the waveguide is 3 mm. Then the

nuclear heat for both waveguides is about 100

W/cm, where the nuclear heat rate is about 12

W/cm^3. The total nuclear heat of the waveguide

in a launcher is about 700 kW for A type and

about 800 kW for B-type.

The r.f loss for both waveguide sizes is about

2 W/cm, which can be negligible in comparison

with the nuclear heat.

The estimation of plasma radiation is rather

complicated, because the radiation intensity is

reduced with the distance from the waveguide

aperture and on the other hand there is the

reflection of the radiation inside the waveguide.

However the total radiation load incident from

the aperture can be easily obtain. The total

radiation load for one waveguide is about 810

watt for A-type launcher and about 320 watt for

B-type launcher. They can be also neglected in

comparison with the nuclear heat.

(2) Heat load of launcher vessel

When the wall thickness of the vessel is 2 cm,

the total nuclear heat is about 900 kW for A

type and about 600 kW for B type. As the launcher

front receives the radiation load of 23 W/cm^2

from the plasma, the total radiation load includ-

ing the radiation load of the waveguide is about

70 kW for A-type launcher, and about 40 kW for B-type

launcher. Then the total heat load of the launcher is

700 + 900 + 70 ∿ 1.7 Mw for A type,

800 + 600 + 40 ∿ 1.5 MW for B type

These heat loads are listed in Table V-2-3.

2.2.5 Conceptual design

When a launcher for plasma heating is composed of 48 waveguides, 16 A-type launchers are required to inject the r.f power of 75 MW. While for a current drive launcher composed of 56 waveguides, 4 B-type launchers are required to inject the r.f power of 10 MW.

The port size is horizontally about 2 m and vertically about 3 m. As the less r.f port number is desirable from the point of view of large branket space, we design the two type structures as shown in Fig. V-2-24.

The one is composed of only A-type launchers as shown in Fig. V-2-24-(a). Two ports of this type are required in this design.

The another is composed of 4 A-type launchers and 4 B-type launchers as shown in Fig. V-2-24-(b).

The 85 MW r.f power can be injected by above three ports, which is less than the ICRF heating system by one port.

The total view of the A-type launchers in the reactor is shown in Fig. V-2-25. The front surface of the

launcher is set as same as the first wall position
from the plasma surface. The launcher cross section-
al view is previously shown in Fig. V-2-21. The launcher
vessel and the waveguide are made of stainless steel.
The waveguide inner surface is coated Cu to reduce
the r.f loss and further the waveguide surface near
the aperture has TiC coating layer to protect the
high frequency discharge.

As the launcher suffers the some heat loads, it is
cooled by water. Although there are many supporters,
the cooling water can pass through the each gap
between the waveguides. The launcher vessel has the
role of the water jacket.

To avoid the trouble of the many waveguides connec-
tion near the access door, particularly in the
vacuum region, it is desirable to use the multiwave-
guide connector as shown in Fig. V-2-26. The connec-
tor has the same structure compared to the launcher,
such as it has the vessel contains the coolant.

The total cross sectional view of the R.F port is shown
in Fig. V-2-27. The flux of waveguides are located in
the shield.

A preliminary investigation of penetration shield
for the LHRF duct was carried out. Since the RF duct
is filled with parallel waveguides by 34%, streaming
neutrons which have vertical direction will be attenuat-
ed by these waveguide materials. One dimensional

neutron transport calculation for a homogeneous mixture
of SS and air shows considerable decreases of neutron
flux in the duct. These results suggest us that a
necessary shield thickness around the duct may be as
small as 50 cm at a distance of 4.6 m from the duct
entrance.

The first corner of the RF duct is striken by high
energy neutrons from the plasma directly. It is
estimated that about 70 cm thick shield of SS may be
needed to keep the dose rate below 2.5 mrem/h outside
the duct surface at 24 hours after shut down.

2.2.6 Electric power supply

Supposing the transport efficiency of the waveguide
system of 50%, that is -3 dB, we obtain the total
output power of 170 MW from the R.F power amplifier.
Because of the recent development of high power
klystron, the MW class klystron can be available.
When the 1 MW klystron like as the one for JT-60
LHRF heating system is used, the total klystron
number is 180. If the klystron for plasma heating
can be operated with the r.f output power of 3.74
MW in the duty of 10 sec/246 sec, the klystron
number for plasma heating will be 40 and the total
klystron number will be 60, including 20 klystrons
of 1 MW output power for current drive with the
continuous operation. As 50% power efficiency of
the R.F amplifier and 85% power factor of the

rectifier and transformer can be usually acceptable,
the A.C power supply requires the capacity of 400 MVA,
which is much larger than the ICRF power supply.
About 350 MVA of it is devoted to plasma heating
with the operation of 10 sec/246 sec duty. About
50 MVA requires the continuous power supply for
about 200 sec.

The diagram of power supply of LHRF heating system
is shown in Fig. V-2-28 for the power amplifier
with 1 MW-klystron.

2.3 Electron cyclotron wave launching system

No contribution to this subsection.

Table V-2-2　Electromagnetic force and stress at disruption, where σs is the shering stress due to f_{10} and f_{11}, σb is the bending stress due to f_{12}, and σt is the tensile stress due to f_{13}

Force and stress	Launcher for plasma heating	Launcher for current drive
f_{10}　(kg/m)	2.6×10^4	1.4×10^4
f_{11}　(kg/m)	8.9×10^3	4.9×10^3
f_{12}　(kg/m)	1.8×10^4	3.7×10^4
f_{13}　(kg/m^2)	2×10^4	4×10^4
σs　(kg/mm^2)	0.5	0.2
σb　(kg/mm^2)	3×10^{-3}	1×10^{-2}
σt　(kg/mm^2)	2×10^{-2}	4×10^{-2}

Table V-2-3　Heat load of launcher

Heat load	Launcher for plasma heating		Launcher for current drive	
	Waveguide	Vessel	Waveguide	Vessel
Nuclear heat (kW)	700	900	800	600
	1600		1400	
Plasma radiation (kW)	40	30	20	20
	70		40	
r.f loss (kW)	14		16	
Total heat load of one launcher (MW)	1.7		1.5	
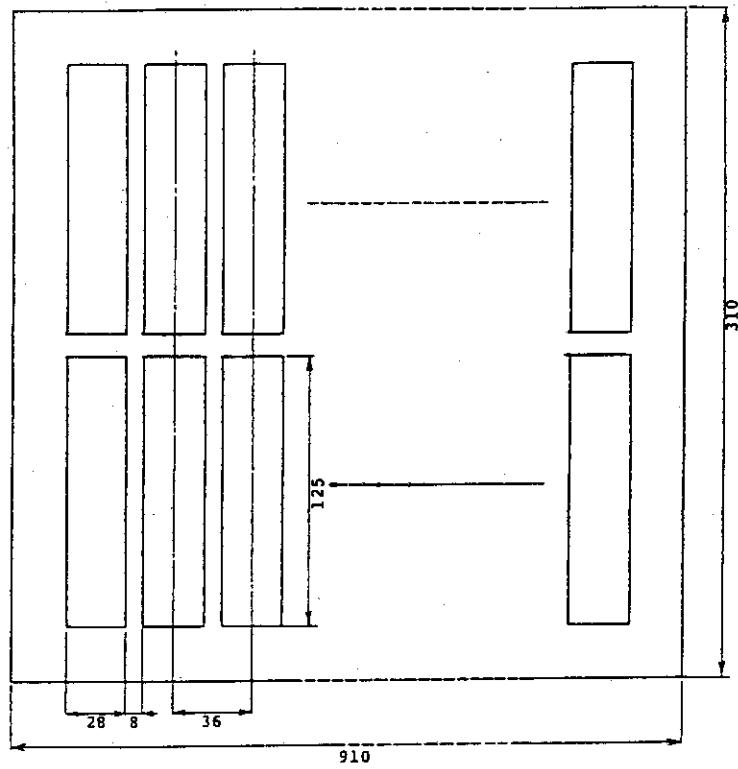
Fig. V-2-19 Launcher size for plasma heating
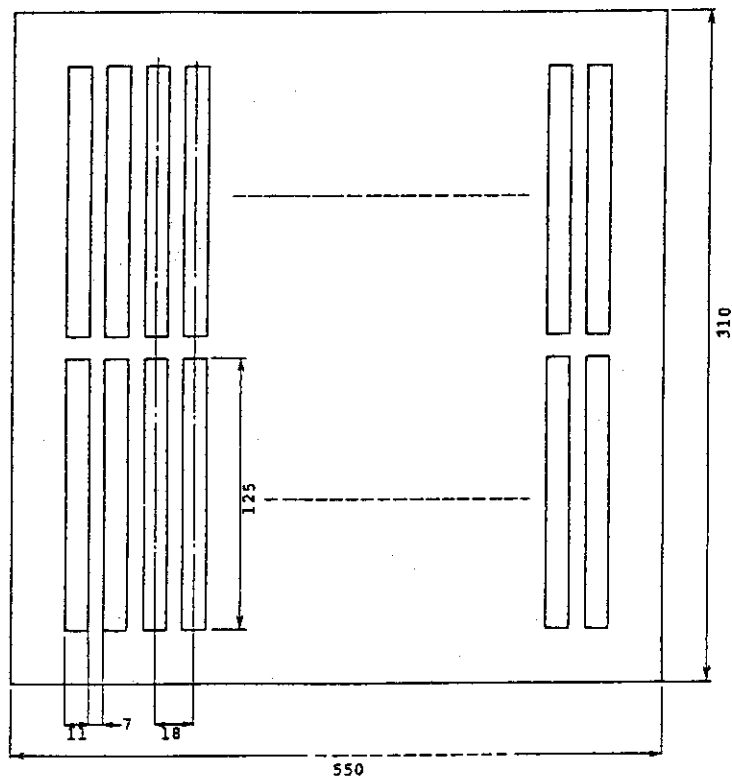
Fig. V-2-20 Launcher size for current drive
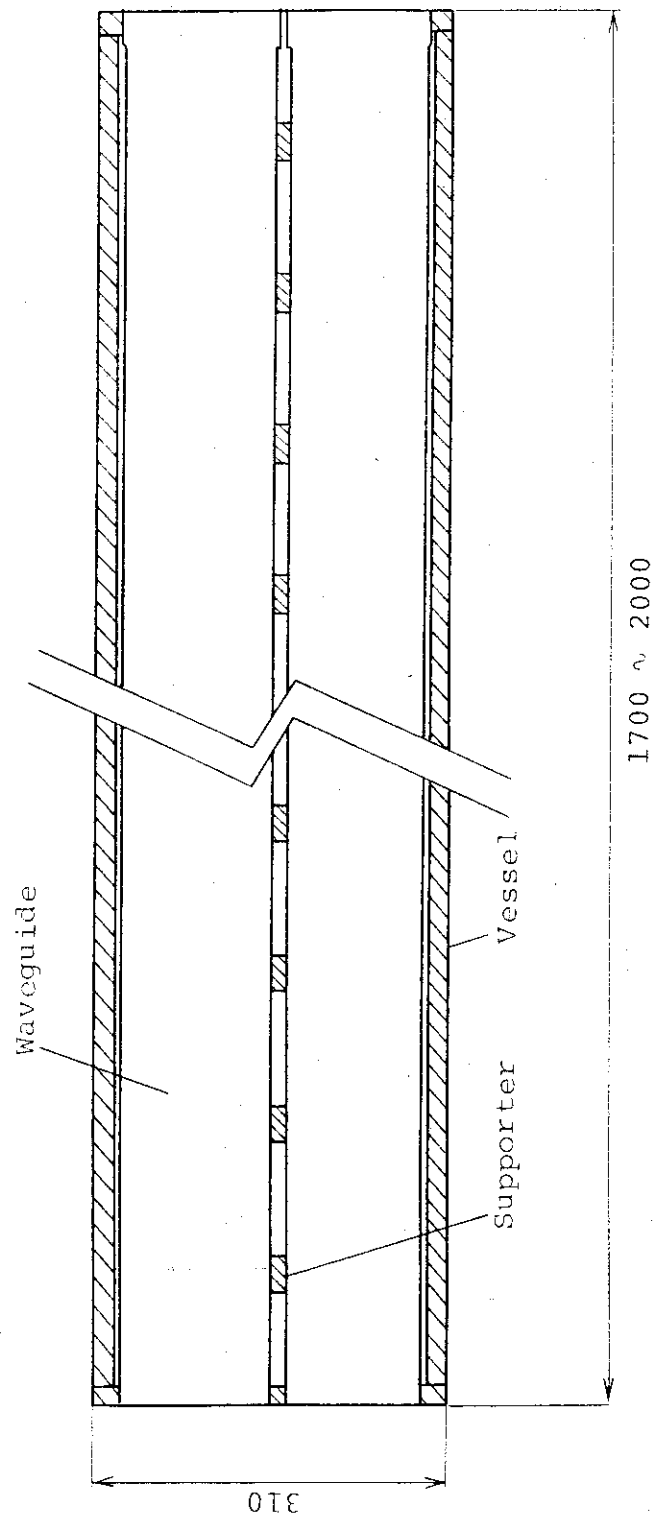
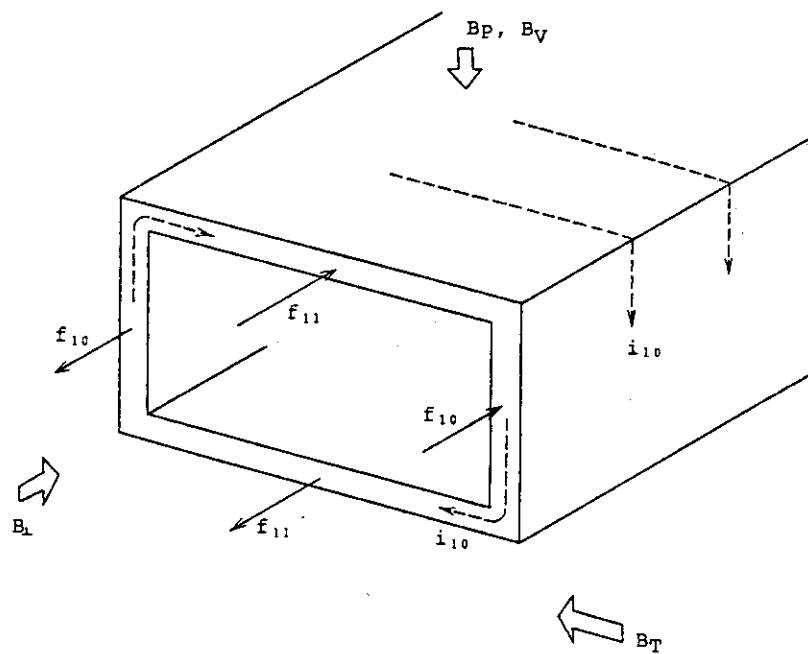Fig. V-2-21 Cross sectional side view of launcher

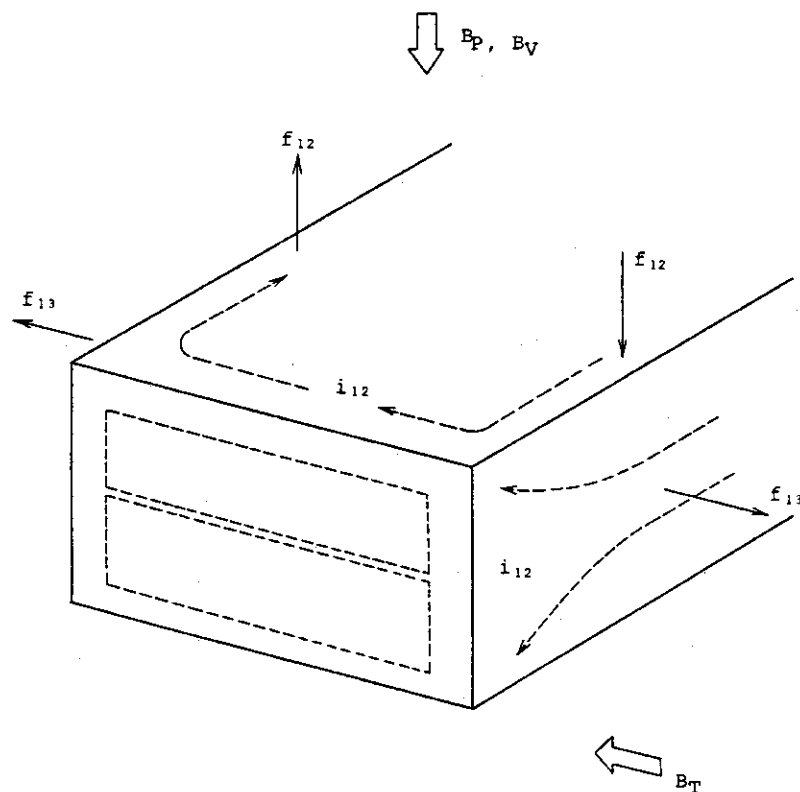Fig. V-2-22   Induced current and electromagnetic force
of LHRF launcher

Fig. V-2-23   Induced current and electromagnetic
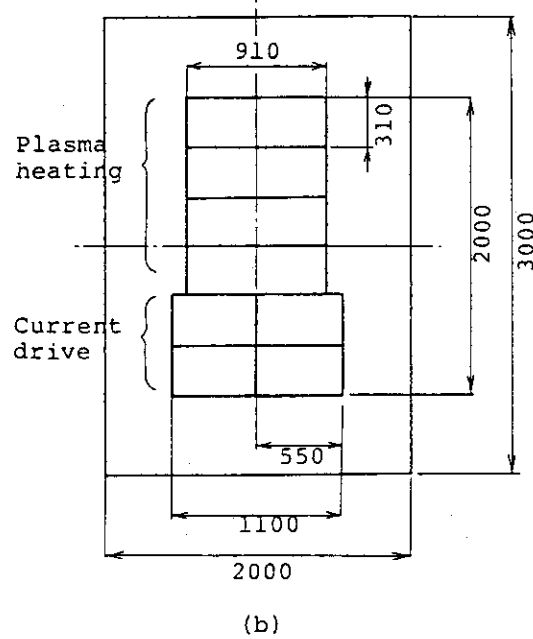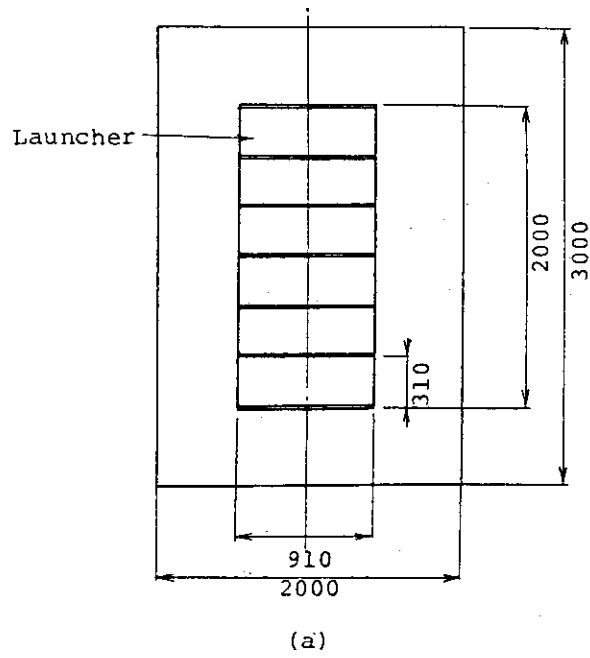force of LHRF launcher

(a)

(b)

Fig. V-2-24   R.F. port overview; (a) for plasma heating,
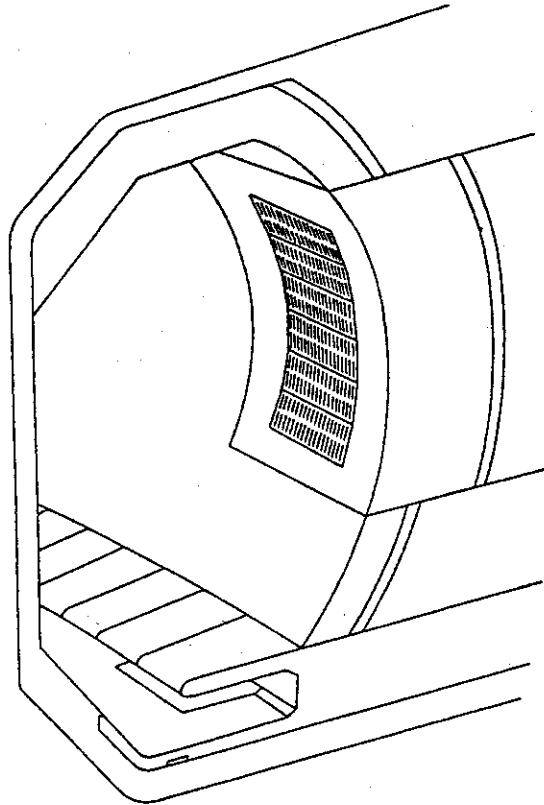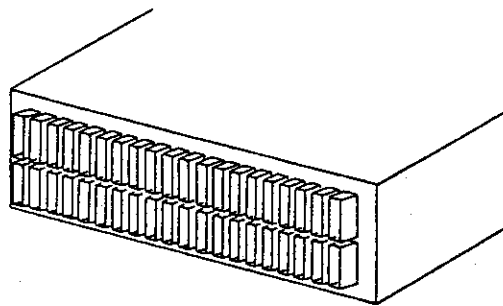(b) for plasma heating + current drive
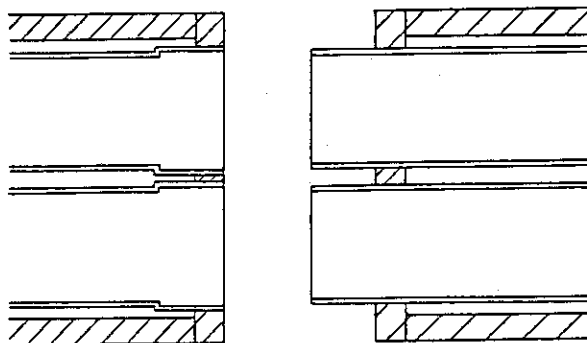
Fig. V-2-25   Schematic view of LHRF launcher in reactor

(a)
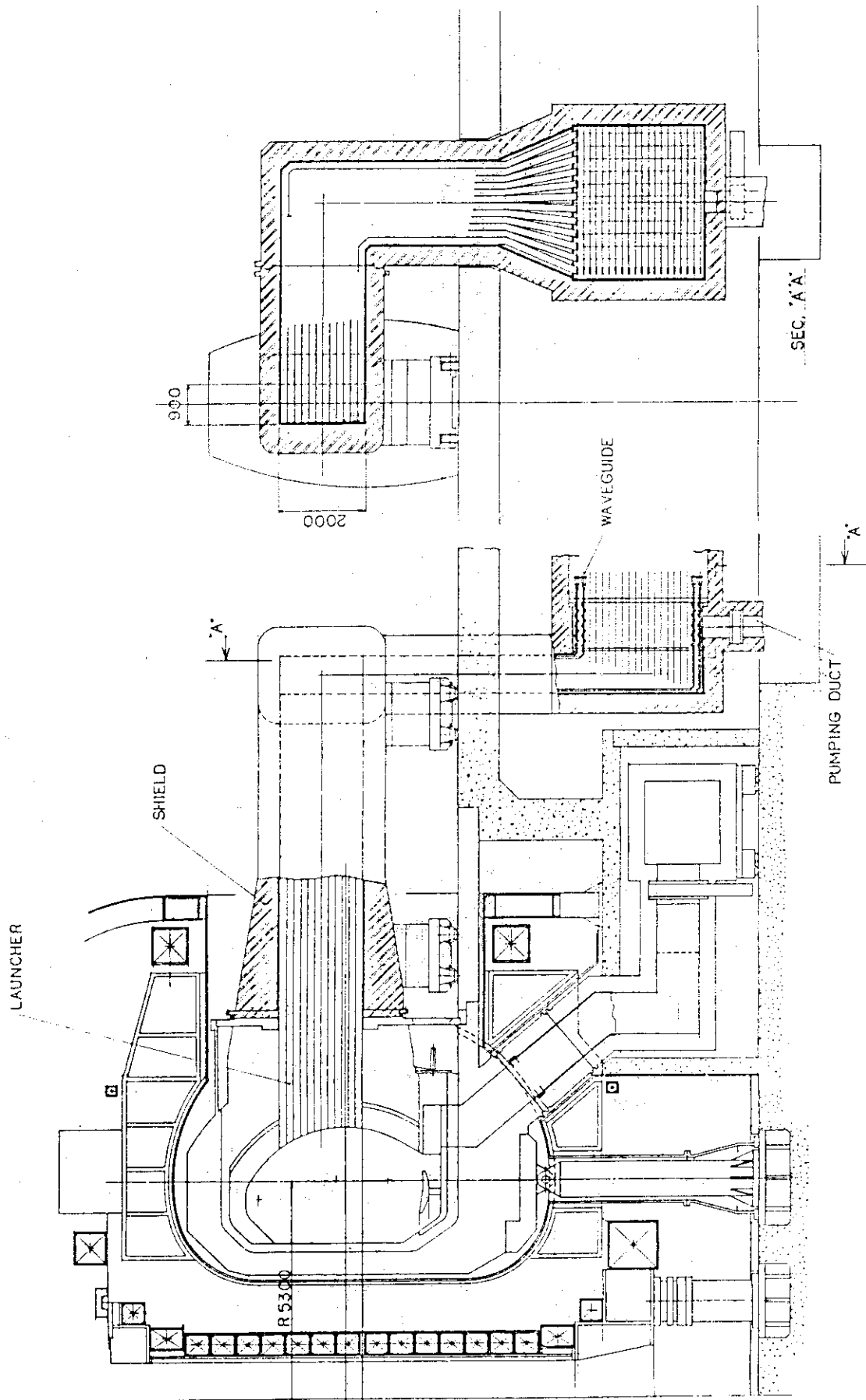

(b)

Fig. V-2-26   Launcher connector

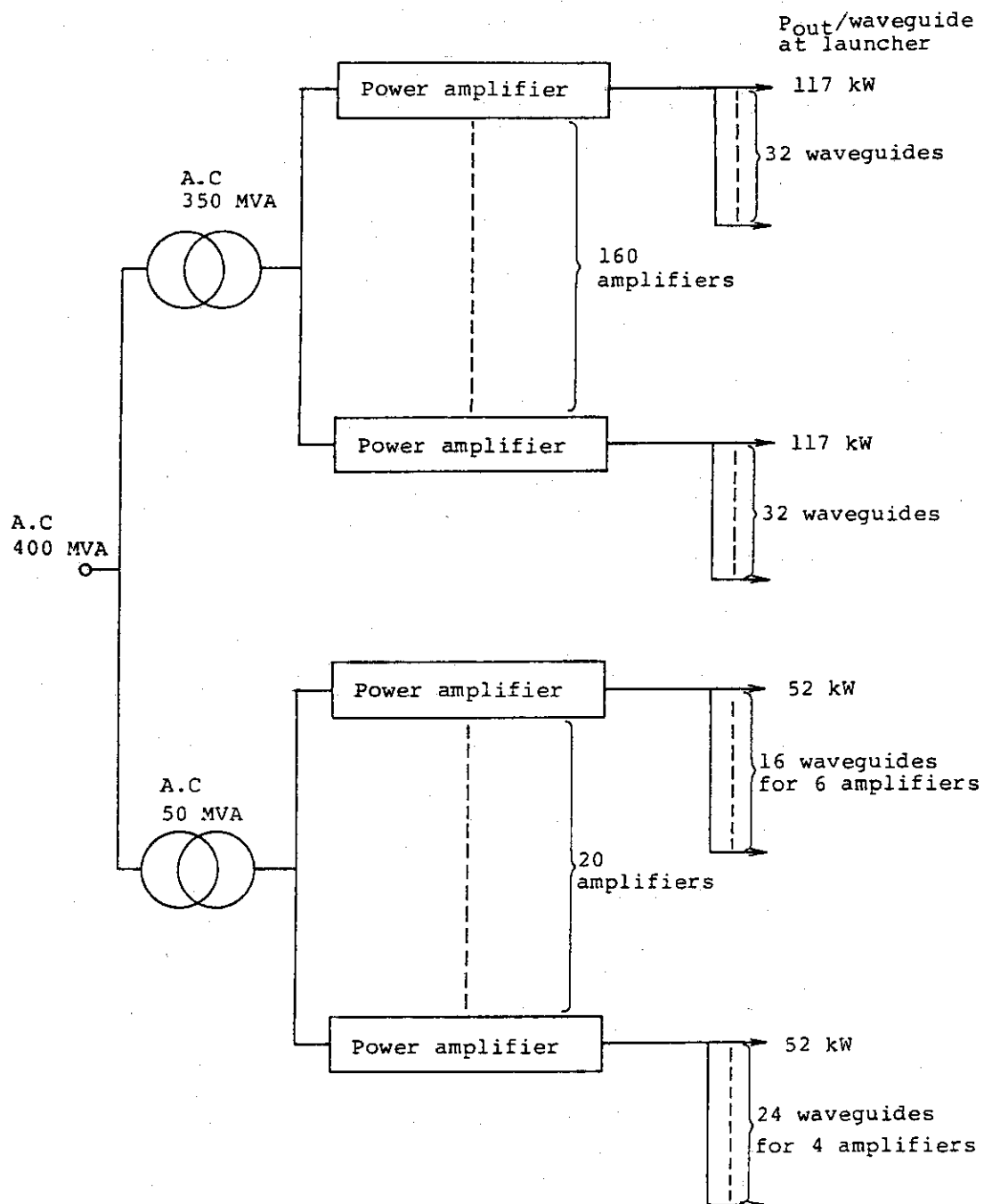Fig. V-2-27 Cross sectional view of R.F port

Fig. V-2-28 Schematic diagram of power supply

3. Conclusions and referece heating system

The physics data base for heating in the ion cyclotron range of frequencies (ICRF) has improved especially in PLT experiments. Benchmark calculation of INTOR plasma heating by the second harmonic deuterium mode is carried out and it is found the strong single pass absorption occurs when Ti(o) > 1 keV and centrel deuterium heating is dominant when Ti(o) < 10 keV and electron heating with a fairly broad spatial distribution progressively supplants the ion heating as the electron temperature increases. Preliminary calculations of ignition approach by ICRF heating are made by one dimensional trasport code with power deposition profile given in benchmark calculation. It is shown that heating power of 50-70 MW is enough to ignite the INTOR plasma. For an ICRF launcher, 2×2 arrays of loop antenna per one port is designed to feed 15 MW.

Lower hybrid heating (LHH) is attractive because of the engineering simplicity of its wave guide launching system. Although data base of high power heating experiments is not sufficient yet, several plans of multi-mega watt heating experiments are being prepared. Numerical simulation of lower hybrid heating in INTOR plasma is carried out and it is shown that the real time feedback control of RF parameters of phase difference, power and frequency is necessary and satisfactory heating efficiency can be expected for optimum heating performance. Concepts for launching structure of wave giude is provided to feed 85 MW from 4 ports. Current drive by lower hybrid wave has been demonstrated by JFT-Ⅱ and a number of Tokamaks and form a generally consistent picture. Preliminary estimation of RF power deposition and generated current profiles are carried out by use of Fokker-Planck equation coupled to an energy loss term and guasi-linear

diffusion term. However data base at the present time still remains inadequate for contemplating using this mechanism for steady state concept of INTOR primarilly due to its limitation to low density operation.

The observation of current ramping by LH waves not only gives credence to current ramp-up in INTOR start-up period, but also to a revised mode of operation possessing a number of attractive features. The items of LHH and the current drive should be the important items of R and D.

Relative advantages and disadvantages of ICRF, LHH and NBI are considered for the referece heating method of INTOR plasma. The following points are considered as important items,

1) ICRF experimental status: During the past three years ion cycoltron heating has made considerable progress (Ti(o) 3.5 keV by 3.2 MW in PLT). There is convergence between the theoretical models and experimental results

2) LHH experimental status: Data base of LHH in high power level is not adequate yet at the present time. The heating efficiency of LHH is somewhat less than those of ICRF and NBI. However several plans of multi-mega watt experiments and being prepared and the experimental and theoretical studies of current drive by lower hydrid wave is in rapid progress.

3) NBI experimental status: these is more experience with NBI than with ICRF

4) Global technological and economical considerations make ICRF and LHH more desirable than NBI for use on a reactor, because of the remoteness of sensitive components from the reactor core, higher system efficiency and easier maintenance.

On the basis of these consideration it is recommended that ion

cyclotron heating be adopted as the reference heating method for the

INTOR phane II A design concept, although it is recognized that this

choice entails a somewhat higher physics risk.   Neutral beam heating

is taken to be backup option and hower hybrid heating and the current

drive are to be important items of R and D.

On the basis of these consideration it is recommended that ion
cyclotron heating be adopted as the reference heating method for the
INTOR phane II A design concept, although it is recognized that this
choice entails a somewhat higher physics risk. Neutral beam heating
is taken to be backup option and hower hybrid heating and the current
drive are to be important items of R and D.

References

[A1] T. Imai, M. Okamoto, and T. Nagashima, JAERI-M 9879 (1981).

[N1] Japanese Contributions to IAEA INTOR Workshop, Phase IIA,
      Chapter I: Introduction, Chapter II: Summary and Recommendation,
      Chapter III: INTOR Concept, JAERI-M 82-170.

[N2] Japanese Contributions to IAEA INTOR Workshop, Phase IIA,
      Chapter IV: Plasma Confinement and Control, JAERI-M 82-171.

[N3] Japanese Contributions to IAEA INTOR Workshop, Phase IIA,
      Chapter V: RF Heating and Current Drive, JAERI-M 82-172.

[N4] Japanese Contributions to IAEA INTOR Workshop, Phase IIA,
      Chapter VI: Impurity Control Physics, JAERI-M 82-173.

[N5] Japanese Contributions to IAEA INTOR Workshop, Phase IIA,
      Chapter VII: Impurity Control and Fisrt-Wall Engineering, JAERI-M
      82-174.

[N6] Japanese Contributions to IAEA INTOR Workshop, Phase IIA,
      Chapter VIII: Tritium and Blanket, JAERI-M 82-175.

[N7] Japanese Contributions to IAEA INTOR Workshop, Phase IIA,
      Chapter IX: Magnets, JAERI-M 82-176.

[N8] Japanese Contributions to IAEA INTOR Workshop, Phase IIA,
      Chapter X: Electromagnetics, JAERI-M 82-177.

[N9] Japanese Contributions to IAEA INTOR Workshop, Phase, IIA,
      Chapter XI: Mechanical Configurations, JAERI-M 82-178.

[N10] Japanese Contributions to IAEA INTOR Workshop, Phase IIA,
      Chapter XII: Engineering Testing, JAERI-M 82-179.